

Abstract

Interfacing robotic devices with humans presents significant control challenges, as the control algorithms governing these machines must accommodate for the inherent variability among individuals. This requirement necessitates the system's ability to adapt to changes in the environment, particularly in the context of human-in-the-loop applications, wherein the system must identify specific features of the human interacting with the machine. In the field of rehabilitation, one promising approach for exercise-based rehabilitation involves the integration of hybrid rehabilitation machines, combining robotic devices such as motorized bikes and exoskeletons with functional electrical stimulation (FES) applied on lower-limb muscles. This integrated approach offers the potential for repetitive training, reduced therapist workload, improved range of motion, and therapeutic benefits. However, conducting prolonged rehabilitation sessions to maximize functional recovery using these hybrid machines imposes several difficulties. Firstly, the design and analysis of adaptive controllers are motivated, but challenges exist in coping with the inherent switching effects associated with hybrid machines. Notably, the transitions between gait phases and the dynamic switching of inputs between active lower-limb muscles and electric motors and their incorporation in the control design remain an open problem for the research community. Secondly, the system must effectively compensate for the influence of human input, which can be viewed as an external disturbance in the closed-loop system during rehabilitation. Robust methods for understanding and adapting to the variations in human input are critical for ensuring stability and accurate control of the human-robot closed-loop system. Lastly, FES-induced muscle fatigue diminishes the human torque contribution to the rehabilitation task, leading to input saturation and potential instabilities as the duration of the exercise extends. Overcoming this challenge requires the development of control algorithms that can adapt to variations in human performance by dynamically adjusting the control parameters accordingly. Consequently, the development of rehabilitative devices that effectively interface with humans requires the design and implementation of control algorithms capable of adapting to users with varying muscle

and kinematic characteristics. In this regard, adaptive-based control methods provide tools for addressing the uncertainties in human-robot dynamics within exercise-based rehabilitation using FES, while ensuring stability and robustness in the human-robot closed-loop system.

This dissertation develops adaptive controllers to enhance the effectiveness of exercise-based rehabilitation using FES. The objectives include the design and evaluation of adaptive control algorithms that effectively handle the switching effects inherent in hybrid machines, adapt to compensate for human input, and account for input saturation due to muscle fatigue. The control designs leverage kinematic and torque feedback and ensure the stability of the human-robot closed-loop system. These controllers have the potential to significantly enhance the practicality and effectiveness of assistive technologies in both clinical and community settings.

In Chapter 1, the motivation to design switching adaptive closed-loop controllers for motorized FES-cycling and powered exoskeletons is described. A survey of closed-loop kinematic control methods related to the tracking objectives in the subsequent chapters of the dissertation is also introduced.

In Chapter 2, the dynamic models for cycling and bipedal walking are described: (i) a stationary FES-cycling model with nonlinear dynamics and switched control inputs are introduced based on published literature. The muscle stimulation pattern is defined based on the kinematic effectiveness of the rider, which depends on the crank angle. (ii) A phase-dependent bipedal walking system model with switched dynamics is introduced to control a 4-degrees-of-freedom (DoF) lower-limb exoskeleton assuming single stance support. Moreover, the experimental setup of the cycle-rider and lower-limb exoskeleton system are described.

Chapter 3 presents a switched concurrent learning adaptive controller for cadence tracking using the cycle-rider model. The control design is decoupled for the muscles and electric motor. An FES controller is developed with minimal parameters, capable of generating bounded muscle responses with an adjustable saturation limit. The electric motor controller employs an adaptive-

based method that estimates uncertain parameters in the cycle-rider system and leverages the muscle input as a feedforward term to improve the tracking of crank trajectories. The adaptive motor controller and saturated muscle controller are implemented in able-bodied individuals and people with movement disorders. Three cycling trials were conducted to demonstrate the feasibility of tracking different crank trajectories with the same set of control parameters across all participants. The developed adaptive controller requires minimal tuning and handles rider uncertainty while ensuring predictable and satisfactory performance. This result has the potential to facilitate the widespread implementation of adaptive closed-loop controllers for FES-cycling systems in real clinical and home-based scenarios.

Chapter 4 presents an integral torque tracking controller with anti-windup compensation, which achieves the dual objectives of kinematic and torque tracking (i.e., power tracking) for FES cycling. Designing an integral torque tracking controller to avoid feedback of high-order derivatives poses a significant challenge, as the integration action in the muscle loop can induce error buildup; demanding high FES input on the muscle. This can cause discomfort and accelerate muscle fatigue, thereby limiting the practical utility of the power tracking controller. To address this issue, this chapter builds upon the adaptive control for cadence tracking developed in Chapter 3 and integrates a novel torque tracking controller that allows for input saturation in the FES controller. By doing so, the controller achieves cadence and torque tracking while preventing error buildup. The analysis rigorously considers the saturation effect, and preliminary experimental results in able-bodied individuals demonstrate its feasibility.

In Chapter 5, a switched concurrent learning adaptive controller is developed to achieve kinematic tracking throughout the step cycle for treadmill-based walking with a 4-DoF lower-limb hybrid exoskeleton. The developed controller leverages a phase-dependent human-exoskeleton model presented in Chapter 2. A multiple-Lyapunov stability analysis with a dwell time condition is developed to ensure exponential kinematic tracking and parameter estimation. The controller is tested in two able-bodied individuals for a six-minute walking trial and the performance

of the controller is compared with a gradient descent classical adaptive controller.

Chapter 6 highlights the contributions of the developed control methods and provides recommendations for future research directions.

SWITCHING ADAPTIVE CONCURRENT LEARNING CONTROL FOR POWERED REHABILITATION MACHINES WITH FES

by

Jonathan Alejandro Casas Bocanegra

B.S., Colombian School of Engineering Julio Garavito, 2016

M.S., Colombian School of Engineering Julio Garavito, 2019

Dissertation

Submitted in partial fulfillment of the requirements for the degree of

Doctor of Philosophy in

Mechanical and Aerospace Engineering

Syracuse University

June 2023

Copyright © Jonathan Alejandro Casas Bocanegra June 2023

All Rights Reserved

Contents

Abstract	i
Title	v
Copyright	vi
List of Tables	x
List of Figures	xi
1 Introduction	1
1.1 Rehabilitation with Hybrid Machines	2
1.1.1 FES-Cycling	2
1.1.2 Exoskeletons for Walking Assistance	3
1.1.3 Adaptive Control for Rehabilitation Machines	5
1.2 Outline of the Dissertation	6
2 Dynamics Models and Experimental Setup	9
2.1 Cycle-Rider System	9
2.2 4-DoF Lower Limb Exoskeleton	12
2.3 Experimental Setup	17
2.3.1 Motorized FES-Cycling testbed	17

2.3.2	Lower-limb Cable-Driven Exoskeleton	19
3	Switched Adaptive Integral Concurrent Learning for Cadence Tracking	22
3.1	Control Development	23
3.2	Unknown Constant Parameters	29
3.3	Stability Analysis	30
3.4	Experiments	32
3.4.1	Experimental Protocol	33
3.4.2	Results	35
3.5	Discussion	36
3.5.1	Tracking error performance and convergence	40
3.5.2	Desired cadence trajectories & parameter estimation performance	42
3.5.3	Control Contribution	44
3.5.4	Participants with Neurological Conditions	46
3.6	Conclusion	47
4	Integral Torque Tracking with Anti-Windup Compensation and Adaptive Cadence Tracking for Powered FES-Cycling	49
4.1	Active Torque Tracking Development	50
4.2	Stability Analysis	53
4.3	Experimental Results	55
4.4	Conclusion	58
5	Switched Concurrent Learning Adaptive Control for Treadmill Walking using a Lower-limb Hybrid Exoskeleton	60
5.1	Control Development	61
5.2	Unknown Constant Parameters	64

5.3	Stability Analysis	66
5.4	Experiments	73
5.4.1	Experimental Protocol	73
5.4.2	Participants	73
5.4.3	Results	74
5.5	Discussion	82
5.5.1	Gain tuning and hyper-parameter selection	82
5.5.2	Tracking and Input Performance	85
5.5.3	Parameter estimation convergence	85
5.6	Conclusion	88
6	Conclusions	89
6.1	Contributions and conclusions	89
6.2	Research directions	93
6.2.1	Input-Output Relationship	93
6.2.2	Convergence Rate	94
	References	96
7	Vita	104

List of Tables

3.1	Demographics of subjects with neurological conditions	33
3.2	Tracking results for able-bodied participants: RMS position error e for the full experiment (10 minutes), average cadence percentage error $\bar{e}(\%)$, RMS velocity error \bar{e} (RPM) for the full experiment, and RMS steady-state cadence error \bar{e}_{ss} (RPM) for the last 400 seconds of each trial	36
3.3	Tracking results for participants with NCs: RMS position error e for the full experiment (5 minutes), average cadence percentage error $\bar{e}(\%)$, RMS velocity error \bar{e} (RPM) for the full experiment, and RMS steady-state cadence error \bar{e}_{ss} (RPM) for the last 90 seconds of each trial	36
5.1	Gain tuning and hyperparameter selection for all the experiments	74
5.2	Percentage of time spent on each walking phase during 114 strides (228 steps), for an average walking velocity of 0.48 steps/s	74
5.3	Average RMS tracking error \bar{e}_{rms} and \bar{r}_{rms} . For each joint, the RMS value is calculated by averaging the error across all gait cycles, and then the RMS values of all joints are averaged to obtain an overall measure of tracking error. The difference is calculated and compared using a Wilcoxon signed ranked test for pairwise differences on each gait cycle. * denotes p-value < 0.05	77

List of Figures

2.1	Schematic of the cycle-rider system [17], [43].	10
2.2	Schematic of the lower-limb kinematic chain described by right and left knee, (q_{RK}, q_{LK}), and hip (q_{RH}, q_{LH}) joint angles, respectively, in both legs with one-point foot contact. The model of the walking dynamics switches based on the signal σ , where $\sigma = 1$ denotes the right leg stance phase, and $\sigma = 2$ denotes the right leg swing phase (i.e., left leg stance phase). The times $t_n^{\sigma=1}, t_n^{\sigma=2}$ denote the beginning of each phase, right leg stance, and swing, during step n , respectively. . .	13
2.3	Motorized FES-cycling testbed. The cycling system integrates an electric motor mounted on the frame to drive the chain and a portable stimulator that applies a voltage potential using surface electrodes applied on the quadriceps muscle groups.	17
2.4	Cable-driven lower-limb exoskeleton platform. The system incorporates a hybrid exoskeleton for treadmill walking using a safety harness to provide fall protection. The hybrid exoskeleton combines motors attached to Bowden cables and FES applied to muscles. Encoders are installed on each hip and knee joint and force sensors underneath the sole of the foot to assist with gait phase detection. Real-time data is accessed through the DAC board.	18
2.5	Gait phase detection. (a) Force sensors are installed underneath the sole of the foot to detect heel strike and toe-off events. (b) A schematic that illustrates the detection of foot contact based on the heel and toe reaction forces. (c) The logic is generated for each foot to determine the walking states: values 1 and 2 represent right and left stance, respectively, while value 3 represents double stance. The plot illustrates how the switching signal (orange) is generated out of the walking state (green) defined by the force-based phase detection algorithm. It is shown how the double stance support (value 3 in the walking state signal) is not considered for the switching signal σ	20

3.1	Block diagram of the cycle-rider dynamics and the closed-loop feedback control system. The gray shaded area highlights the uncertainty in the cycle-rider dynamics and muscle effectiveness that the adaptive controller seeks to estimate. The electrical motor controller u_e leverages tracking errors e, r and input-output data from the history stack to improve the parameter estimation and achieve cadence tracking. The muscle input also leverages e, r and is delivered to the system through the unknown muscle effectiveness that switches according to $\sigma(q)$	23
3.2	Kinematic tracking for cycling trial EXP1 (using <i>trajectory 1</i> in (3.33)). Cadence tracking (actual versus desired angular speed) in RPM, position error $e(t)$ (rad), and filtered error $r(t)$ (computed using e (rad) and \dot{e} (rad/sec)) are depicted. Each row corresponds to the cycling performance of one participant for subjects S1-S5.	37
3.3	Kinematic tracking for EXP2 (using <i>trajectory 2</i> in (3.34)). Cadence tracking (RPM), position error $e(t)$ (rad) and filtered error $r(t)$ (computed using e (rad) and \dot{e} (rad/sec)) are depicted. Each row corresponds to the performance of one participant.	38
3.4	Kinematic tracking for EXP3 (using <i>trajectory 1</i> in (3.33)). Cadence tracking (RPM), position error $e(t)$ (rad) and filtered error $r(t)$ (computed with e (rad) and \dot{e} (rad/sec)) are shown. Each row corresponds to the cycling performance of one participant.	39
3.5	Parameter estimates for each participant during the 10-minute experiments. The left column displays the estimates in EXP1 and the right column shows the estimates in EXP2 . The vertical line depicts the instance at which the predetermined FE condition based on $\underline{\lambda}$ in EXP2 is satisfied. Cycling trials corresponding to EXP1 did not satisfy the predefined FE condition; nevertheless, the minimum eigenvalue for all trials in EXP1 is positive as depicted in Figure 3.6. Section 3.2 describes the vector of parameters estimated during the cycling experiments.	40
3.6	Minimum eigenvalue of the history stack, i.e., $\lambda_{min}\{\Sigma_Y\}$. The eigenvalues for EXP1 and EXP2 are shown in blue and red, respectively. The vertical line indicates the time at which the FE excitation condition is satisfied in EXP2.	41
3.7	Control inputs across all experiments of subject S4 . The plots on the left show the normalized control inputs, i.e., muscle and motor, computed for each experiment. The plots on the right show the applied FES input (pulse width) for the right and left quadriceps muscle groups. The FES input was applied 25 seconds after the beginning of the experiments to avoid delivering high stimulation intensities in the transient phase.	42
3.8	Control inputs of subject S4 across 10 crank cycles following 4 minutes of pedaling during the EXP1 . Normalized muscle and motor control inputs are depicted in the top plot. FES delivered to the right and left quadriceps are depicted in the bottom plot.	43

3.9	The control contributions in the controller in (3.11) are illustrated for cycling trials corresponding to EXP2 . The red signal shows the robust state feedback term ($k_e r + e$) while the blue signal shows the adaptive term contribution $Y_o \hat{\Theta}$	44
3.10	Kinematic tracking performance for participants with NCs undergoing EXP1 . Cadence tracking (RPM), position error $e(t)$ (rad) and filtered error $r(t)$ are presented. Each row corresponds to one subject (P1-P3).	45
4.1	Torque tracking for both five-minute cycling experiments: trial one (2 Nm) on the left column and trial two (3 Nm) on the right column. The top plots show the integral torque error $e_{aw}(t)$. The plots in the middle show the muscle control input (pulse width). The bottom plots show a zoom-in version of the muscle input during the saturated regions with saturation limit $\beta_m = 80 \mu s$	56
4.2	Torque error (top plot) and FES input (bottom plot) for trial one (2 Nm) when the system is not saturated (note that $u_m = \text{sat}_{\beta_m}(u_m)$).	57
4.3	Kinematic tracking of the second trial. Cadence tracking is shown on the left side and the position error $e(t)$ and filtered error $r(t)$ are shown on the right.	58
4.4	Adaptive estimates $\hat{\Theta}(t)$ of the uncertain constant parameters computed during the second cycling trial.	59
5.1	Schematic of the lower limbs depicting a subset of the uncertain constant parameters in (5.17) assuming symmetry between legs.	66
5.2	Average RMS tracking errors. The top plots show the average RMS position error e across all joints during each gait cycle. The bottom plots show the average RMS filtered error r . The performance plots in the left and right columns correspond to subject S1 and subject S2, respectively.	75
5.3	Kinematic tracking performance for subject S1 undergoing eight minutes of treadmill walking at a speed of 0.48 steps/s during Exp2. The vertical dashed lines indicate the average switching instances, where the orange background indicates $\sigma = 1$ and the blue indicates $\sigma = 2$	76
5.4	Parameter estimates for subject S1 corresponding to (a) Exp2 and (b) Exp1, and subject S2 corresponding to (c) Exp2 and (d) Exp1. The estimation of the uncertain parameters (described in Section 5.2) is illustrated for eight-minute treadmill walking experiments. The parameters are divided into three groups: Inertial parameters (blue) in kgm^2 , gravitational torque parameters (orange) in Nm , and viscous-damping coefficients (green). The bottom plots for all experiments depict all the parameter estimates combined.	78

5.5	Evolution of the minimum eigenvalue of the history stack, i.e., $\lambda_{\min}\{\sum_{p=1}^{\bar{p}} \mathcal{Y}_p^T \mathcal{Y}_p\}$ for (a) subject S1 and (b) subject S2 during Exp2. The dashed line in red shows the user-defined finite excitation condition $\underline{\lambda}$	79
5.6	Magnitude of the average (± 1 std) contribution of each term in the adaptive update law in (5.7) as a function of the gait cycle percentage during Exp 2 for both participants. The classical gradient-descent term is defined as $Classical = \ \Gamma Y_{\sigma}^T r\ $ (green), whereas the integral concurrent learning term is defined as $CL = \ k_{cl} \Gamma \sum_{p=1}^{\bar{p}} \mathcal{Y}_{\sigma}^T(t_p)(\mathcal{V}_{\sigma}(t_p) - \mathcal{Y}_{\sigma}(t_p)\hat{\Theta}(t))\ $ (purple). The vertical dashed lines indicate the average switching instances, where the orange background indicates $\sigma = 1$ and the blue indicates $\sigma = 2$	80
5.7	Average control inputs for subject S1 (a) applied to the hip and knee joints and (b) segregated by the contribution of the feedback and adaptive terms.	81
5.8	FES pulse width input (μs) delivered to left (top) and right (bottom) quadriceps (orange) and hamstrings (blue) for subject S1 during experiment Exp2. The input signal is shown for an interval of 15 seconds.	82
5.9	RMS control input u_{σ} averaged across all joints for all gait cycles. The top plot illustrates the average input delivered to subject S1 for both experiments, whereas the bottom plot shows the input delivered to subject S2.	83
5.10	RMS feedback and adaptive control input contributions averaged across all joints for all gait cycles. The top plots illustrate the average inputs delivered to subject S1 for both experiments, whereas the bottom plots show the inputs delivered to subject S2.	84

Chapter 1

Introduction

Powered dynamical systems that physically interact with humans need to accurately estimate human attributes and adapt their responses to ensure stability and safety. Controllers for rehabilitation robots interacting with people with neurological conditions (NCs) should ensure safe human-robot interaction and seamlessly customize the assistance for participants with different functional capacities. Thus, advancing the control algorithms of rehabilitation robotic devices can lead to adoption in clinical settings, thereby having the potential to make a significant impact on patients' recovery.

The present dissertation aims to develop and implement data-driven adaptive controllers that customize rehabilitation across multiple participants and estimate the unknown human-robot dynamics to enhance the performance of the closed-loop control system.

This chapter provides an introduction to the use of robotic machines as a rehabilitation interface and outlines the challenges involved with this strategy in two specific rehabilitation scenarios: lower-limb cycling and assisted treadmill-based walking with functional electrical stimulation. Furthermore, the chapter presents the potential advantages and current limitations of adaptive control techniques for rehabilitation machines. Lastly, an overview of the dissertation structure is

provided.

1.1 Rehabilitation with Hybrid Machines

Neurological disorders such as spinal cord injury (SCI) result in partial or total loss of motor and sensory functions, significantly impacting an individual's independence and quality of life [1], [2]. Restoring and improving motor function is a priority for individuals with SCI, as it is crucial in enhancing their overall well-being and daily activities [1], [3]. A rehabilitative strategy that is typically prescribed is cycling induced by functional electrical stimulation (FES), wherein a voltage potential is applied to lower-limb muscles to induce controlled contractions and facilitate pedaling a cycle, either with or without motorized assistance [4]. FES-cycling has been shown to offer cardiovascular and physiological benefits, thereby improving the quality of life for individuals with NCs, including those with SCI [5]–[7]. Another potential approach for restoring function after SCI is the development of active orthotic devices, such as robotic exoskeletons, aimed at assisting gait rehabilitation [3], [8], [9]. These exoskeletons enable individuals with SCI to engage in overground walking or treadmill-based walking with body weight support, which helps partially offload the user's weight and is particularly beneficial for individuals with limited ambulation capabilities [10]. However, each device poses unique challenges when it comes to developing control algorithms. Addressing these challenges and developing effective control methodologies are essential for ensuring safe and efficient rehabilitative interventions for individuals with SCI.

1.1.1 FES-Cycling

Motorized FES-cycling applies electrical stimuli to activate the rider's muscles and engages an electrical motor to provide assistance [11]. An outstanding challenge for the implementation of

FES-powered devices is the need to achieve long-duration rehabilitation sessions to maximize physiological and cardiovascular benefits. Furthermore, the control of FES systems poses additional technical challenges as the dynamics of the muscles (i.e., the control effectiveness that maps the electrical stimulation to torque) is unknown and difficult to measure in practice since it requires complex system identification procedures [12].

Given the inherent characteristics of cycling, FES involves switching across multiple muscle groups to ensure metabolic efficiency and facilitate forward pedaling [13]. Furthermore, an electrical motor is incorporated to provide intermittent assistance when necessary, potentially assisting in delaying muscle fatigue. As a result, the cycle-rider system as a whole can be classified as a switched system, necessitating a stability analysis specifically tailored to switched systems [14]. In the context of speed or cadence tracking, closed-loop feedback controllers employing robust approaches have been designed [15]–[18]. Alternatively, admittance-based controllers have been developed to achieve both cadence and power tracking objectives using robust control strategies [19]. However, it should be noted that robust controllers often incorporate conservative bounds during the design process, which can lead to higher stimulation levels and accelerate the onset of fatigue [17]. Moreover, robust controllers are unable to provide estimates of the uncertainty present in the nonlinear system, limiting their ability to adapt to different subjects and guarantee satisfactory tracking performance.

1.1.2 Exoskeletons for Walking Assistance

While the wearability and design aspects of exoskeletons are crucial, the effectiveness of their gait patterns heavily relies on the control algorithms employed. Tracking controllers, such as proportional-derivative (PD) and impedance-based techniques, are commonly utilized in lower-limb exoskeletons to achieve desired movements [9], [20]. More recently, gait controllers incorporating muscle-reflex models have been implemented to generate torque patterns that mimic

human-like behavior [21]. Alternatively, optimization methods have been proposed to generate optimal gait trajectories and facilitate continuous walking across different gait patterns in exoskeleton-assisted walking [8], [22]. These optimization techniques employ virtual constraints based on hybrid zero dynamics, which are enforced through feedback linearization controllers [23], [24]. However, implementing control algorithms that rely on accurate models of human dynamics is impractical for human-in-the-loop applications. Obtaining personalized dynamic models can involve burdensome and time-consuming system identification procedures, especially when engaging individuals with movement disorders in rehabilitation. In addition, the data collected in the system identification may not capture the dynamic characteristics of the real-time experiments. Moreover, as individuals undergo long-term rehabilitation, the dynamic model may need to be updated periodically to compute the optimized controllers. Hence, there is a need for the design of novel control methods that can cope with uncertainties in the human-robot dynamics and adapt during assisted walking by exploiting online data.

Hybrid exoskeletons, which combine electric motors and FES, pose unique control challenges in terms of control. A shared control approach combining FES with a motor-driven exoskeleton has been developed to control the knee joint [25]. Additionally, cooperative control methods have been developed to enable kinematic tracking of both the knee and hip joints [26], [27]. These methods often utilize an iterative stimulation profile, where pulse duration and amplitude are adjusted based on previous steps. Alternatively, optimal muscle synergy-based controllers have been designed to ensure stable trajectory tracking and facilitate leg swing movements during overground walking [28]. However, the development of a systematic control design and rigorous stability analysis for data-driven gait controllers remains an open problem due to challenges that involve the nonlinear and uncertain nature of walking dynamics.

1.1.3 Adaptive Control for Rehabilitation Machines

Adaptive-based control methods are inherently well-suited for addressing the challenges posed by uncertainty in both cycle-rider dynamics and human-exoskeleton dynamics. These methods involve generating estimates of uncertain parameters within the dynamical system and utilizing these estimates to achieve the desired tracking objective. However, classical adaptive control techniques fail to guarantee convergence of the adaptive estimates to their true values unless a persistence of excitation (PE) condition is satisfied [29], [30]. To overcome this limitation, recent research in adaptive-based concurrent learning control has replaced the PE condition with a finite excitation condition, ensuring exponential convergence of both the adaptive estimates and tracking errors [31]–[33]. The significant advantage of this technique lies in its capacity to exploit input-output data stored in a history stack, which accumulates until a sufficient amount of rich data is collected to achieve a full-rank condition. This verifiable condition guarantees parameter convergence and eliminates the requirement for persistently exciting trajectories, thereby making it a more practical and appropriate approach for ensuring safe human-robot interaction.

Convergence of the adaptive estimates of the unknown parameters depends on the PE condition [34], which is hard to satisfy in many real-time applications [35]. Further, satisfying the PE condition is unfeasible in human-robot applications that aim to ensure smooth operation and prioritize human safety. Therefore, concurrent learning offers an alternative to replace the PE condition for a less-restrictive finite excitation condition that relies on the quality of the data collected during the early stages of the experiment. Concurrent learning control strategies have recently been designed and applied to human-robot systems such as motorized FES-cycling [36], [37] and bicep curls [38], [39]. However, the development of a concurrent learning strategy for controlling a hybrid multi-joint exoskeleton encounters specific challenges arising from the non-linear, uncertain nature of gait and muscle dynamics, which involve a large number of coupled uncertain parameters and transient effects due to gait phase transitions (e.g., between swing and stance phase).

Conventional Lyapunov-based theory cannot be applied to analyze the stability of adaptive controllers for switching FES-cycling and walking with hybrid exoskeletons. Instead, switched systems theory [14] is exploited in this work to analyze the cycle-rider and human-exoskeleton model with phase-dependent switched dynamics that account for the input switching and gait phase transitions. Hence, this dissertation develops contributions at the emerging intersection of adaptive control methods and switching systems for rehabilitative powered devices. The outline of this work is presented in the next section.

1.2 Outline of the Dissertation

In Chapter 2, the dynamic models of the cycle-rider stationary cycling system and the robotic phase-dependent lower-limb exoskeleton with FES inputs are introduced. The cycling model includes the switching effects of activating multiple muscle groups based on a state-dependent stimulation pattern that exploits the kinematic effectiveness of the rider. The bipedal walking model for exoskeleton control is developed considering the gait phase transitions during walking modeled with switching dynamics. The experimental testbeds developed to demonstrate the feasibility of the control design for cycling and treadmill-based walking with a lower-limb exoskeleton are introduced.

In Chapter 3, a closed-loop switched integral concurrent learning adaptive controller inspired by the work in [32] is designed to track a desired cadence trajectory using the model of a motorized FES-cycling system introduced in Section 2.1. The muscle groups and electric motor are activated based on state-dependent switching signals that exploit the kinematic effectiveness of the rider [17]. Therefore, the adaptive update law exploits the feedback of the currently active subsystem to selectively store input-output data in a history stack using the singular value decomposition algorithm described in [32], [40]. The algorithm stores data that maximizes the minimum singular value of the history stack, which is related to the rate of convergence of the

adaptive estimates of the unknown parameters. A Lyapunov-based stability analysis is developed for the overall cycle-rider switched system and is segregated into two phases. In the first phase, the individual history stacks of the subsystems do not satisfy the excitation condition (i.e., the minimum eigenvalue is not positive), and thus, a negative semidefinite result is obtained in the Lyapunov stability analysis. Asymptotic tracking and bounded parameter estimation are guaranteed by invoking an invariance-like extension for adaptive switched systems using non-strict common Lyapunov functions [41]. In the second phase, all the subsystems satisfy the finite excitation condition, and thus the Lyapunov derivative becomes negative definite, guaranteeing exponential tracking and parameters convergence since the Lyapunov function is common for all the subsystems [14]. Testing was performed with eight able-bodied individuals and three individuals with neurological conditions. The results demonstrate the feasibility of the control design and show satisfactory performance for a wide range of participants demanding minimal tuning despite the inherent variability in participants.

In Chapter 4, an integral torque tracking controller is designed with anti-windup compensation to activate lower-limb muscles using FES for power tracking (i.e., achieve the dual objective of torque and cadence tracking). The design of an integral error is required to prevent the need for feedback of high-order derivatives of the torque signal. The muscle controller addresses the challenge of fast error build-up due to the integration action that otherwise can lead to applying high FES inputs to the muscles, causing discomfort and fatigue. This chapter leverages the adaptive control design presented in Chapter 3 for the electric motor cadence tracking objective. The modified integral muscle torque tracking error signal mitigates error buildup when the muscles inherently saturate in experiments. This control design accounts for input saturation in the model, which is rigorously analyzed to provide stability guarantees. One major advantage of this approach is that it enables the controller to cope with input saturation, thereby reducing muscle discomfort and potentially delaying the onset of muscle fatigue. The feasibility of the design is evaluated through preliminary experiments with one able-bodied individual. These experiments demonstrate that the controller achieves reliable and satisfactory performance, highlighting its

potential for enhancing the practicality and effectiveness of FES cycling systems in clinical and community settings.

In Chapter 5, the design and experimental implementation of a switched adaptive concurrent learning controller are developed for treadmill walking using a 4-degrees-of-freedom (DoF) hybrid exoskeleton controlling the hip and knee joints bilaterally. The combined human-exoskeleton dynamics are modeled as a phase-dependent switched system to account for the gait phase transitions between the right and left leg, as presented in Section 2.2. The leg dynamics switch between two models that capture the following: (1) the right leg is in the stance phase and the left leg is in the swing phase, and (2) the left leg is in the stance phase and the right leg is in the swing phase. The concurrent learning adaptive controller, inspired by [32], is developed to estimate uncertain parameters of the lower limb dynamics and track desired joint kinematic trajectories. The designed switched controller applies FES to the quadriceps and hamstring muscle groups and activates electric motors to provide assistance to the knee and hip joints in both legs. A multiple Lyapunov function analysis is developed to ensure the stability of the closed-loop error system with switching effects due to the gait phase transitions. A dwell time analysis is provided to guarantee tracking errors decay across sequential gait phase transitions. Treadmill walking experiments are implemented at a constant speed in two able-bodied individuals to illustrate the feasibility of the developed control methods. The performance of the concurrent learning controller and a classical gradient-based adaptive controller are compared during six-minute treadmill walking trials. The results indicate that the switching concurrent learning controller achieves a lower mean root-mean-squared (RMS) kinematic tracking error for both the knee and hip joints compared to the gradient-based adaptive controller.

In Chapter 6, a summary of the dissertation is provided along with a discussion on potential extensions and future research directions based on the results developed in previous chapters.

Chapter 2

Dynamics Models and Experimental Setup

In this chapter, the nonlinear dynamic models with switching effects are presented for the cycle-rider system leveraging [17], [42], and the 4-DoF lower-limb cable-driven exoskeleton with FES. Note that for simplicity, a similar notation will be leveraged for both systems. Therefore, clarification on the notation will be provided to rigorously define the state, input, and regressor dimensions for cycling or walking.

2.1 Cycle-Rider System

The cycle-rider system is modeled as a single DOF using a closed kinematic chain as illustrated in Figure 2.1, where the crank angle is denoted by q , the hip and knee joint angles with respect to the horizontal (dashed lines) are denoted by q_{hip} and q_{knee} , respectively, and the trunk angle is denoted by q_t . The measurable relative hip and knee angles are denoted by ϕ_{Hip} and ϕ_{Knee} , respectively, and the crank length, shank length, and thigh length are denoted by l_c , l_l , and l_t , respectively [17], [43]. The cycle-rider system is modeled with the following Euler-Lagrange

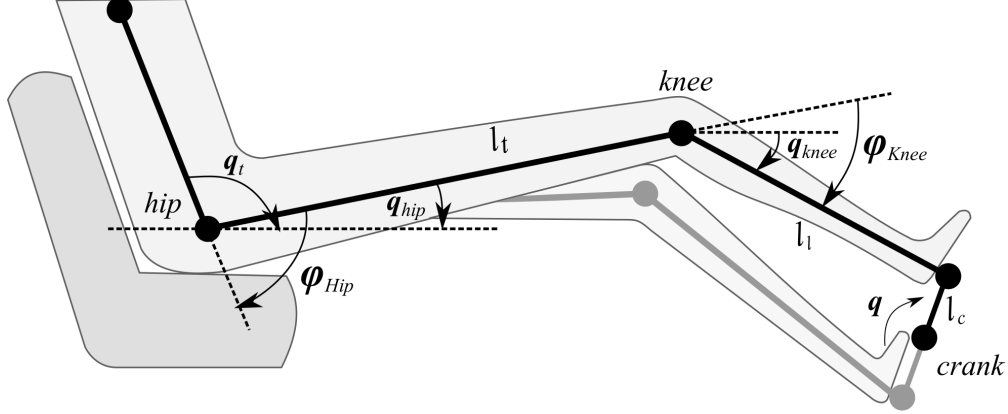


Figure 2.1: Schematic of the cycle-rider system [17], [43].

dynamics¹ [17], [36]

$$M(q(t))\ddot{q}(t) + C(q(t), \dot{q}(t))\dot{q}(t) + G(q(t)) + C_d\dot{q}(t) = \tau_m(t, \sigma) + \tau_e(t), \quad (2.1)$$

where $q : \mathbb{R}_{\geq t_0} \rightarrow \mathcal{Q}$ and $\dot{q} : \mathbb{R}_{\geq t_0} \rightarrow \mathbb{R}$ denote the measurable crank angle and crank velocity, respectively, and $\ddot{q} : \mathbb{R}_{\geq t_0} \rightarrow \mathbb{R}$ denotes the unmeasurable crank acceleration. The set of crank angles is denoted by $\mathcal{Q} \subseteq \mathbb{R}$, and $t_0 \in \mathbb{R}_{\geq 0}$ denotes the initial time. The inertial, centripetal-Coriolis, gravitational effects, and viscous damping coefficient are denoted by $M : \mathcal{Q} \rightarrow \mathbb{R}_{>0}$, $C : \mathcal{Q} \times \mathbb{R} \rightarrow \mathbb{R}$, $G : \mathcal{Q} \rightarrow \mathbb{R}$, and $C_d \in \mathbb{R}_{>0}$, respectively. The torque applied at the crank by an electrical motor is denoted as τ_e and the torque evoked by muscle activation through FES is denoted as τ_m . The set of muscles considered in the model are the right and left quadriceps muscle groups. The quadriceps muscle groups are only activated in the crank regions where they can evoke significant active torque to achieve forward pedaling, i.e., within kinematically efficient regions denoted as $\mathcal{Q}_R, \mathcal{Q}_L \subset \mathcal{Q}$ [42]. The logic state variable denoted by $\sigma : \mathcal{Q} \rightarrow \mathcal{S}$,

¹For notational brevity, the explicit dependence of time, t , is hereafter suppressed unless required for clarity of exposition.

where $\mathcal{S} \triangleq \{RQ, KDZ, LQ\}$ is the set of possible switching subsystems, is defined as

$$\sigma(q) \triangleq \begin{cases} RQ & q \in \mathcal{Q}_r \\ KDZ & q \notin (\mathcal{Q}_r \cup \mathcal{Q}_l) , \\ LQ & q \in \mathcal{Q}_l \end{cases} \quad (2.2)$$

where RQ, LQ denote when the right and left quadriceps are activated, respectively, and the KDZ denotes the kinematic dead zone, where muscles are not activated as they do not evoke significant active torque. Using (2.2), the torque produced by the muscle $\tau_m : \mathbb{R}_{\geq t_0} \times \mathcal{S} \rightarrow \mathbb{R}_{>0}$ in (2.1) can be defined as

$$\tau_m(t, \sigma) \triangleq \begin{cases} B_{RQ}u_m(t) & \sigma = RQ \\ 0 & \sigma = KDZ , \\ B_{LQ}u_m(t) & \sigma = LQ \end{cases} \quad (2.3)$$

where $B_{RQ}, B_{LQ} \in \mathbb{R}_{>0}$ are the unknown muscle control effectiveness for the right and left quadriceps, respectively, and u_m is a subsequently designed muscle control input.

Assumption 1. *The individual muscle effectiveness within the kinematically efficient regions is considered to be an unknown constant. This is a reasonable assumption for trials with stimulation regions with small time duration [12], [39]. Thus, exact model knowledge of the control effectiveness B_{RQ} and B_{LQ} is not needed for the design of the muscle torque input τ_m .*

The torque applied by the electrical motor at the crank $\tau_e : \mathbb{R}_{\geq t_0} \times \mathcal{S} \rightarrow \mathbb{R}$ can be defined as

$$\tau_e(t, \sigma) \triangleq B_e u_e(t, \sigma), \quad (2.4)$$

where $B_e \in \mathbb{R}_{>0}$ denotes the known motor constant control effectiveness and u_e is a subsequently designed motor control input. The following properties of (2.1) are exploited in the subsequent

control design and stability analysis.

Property 1. $\underline{m} \leq M \leq \overline{m}$, where $\underline{m}, \overline{m} \in \mathbb{R}_{>0}$ are known constants [44, Ch.3].

Property 2. By skew symmetry $\frac{1}{2}\dot{M} - C = 0$ [44, Ch.3].

Property 3. The functions M , C , and G are linearly parameterizable and bounded given bounded arguments [44, Ch.3].

Property 4. $\underline{B}, \overline{B} \in \mathbb{R}_{>0}$ are known lower and upper bounds of the muscle effectiveness B_m defined as $\underline{B} \leq \min\{B_{RQ}, B_{LQ}\}$ and $\overline{B} \geq \max\{B_{RQ}, B_{LQ}\}$, respectively.

2.2 4-DoF Lower Limb Exoskeleton

This dynamic model considers a 4-DoF kinematic chain that models the combined human-exoskeleton dynamics in the sagittal plane with point-foot contact. Transitions across gait phases are determined by the switching signal $\sigma(t) : \mathbb{R}_{\geq t_0} \rightarrow \mathcal{S}$, with $\mathcal{S} = \{1, 2\}$ and $t_0 \in \mathbb{R}_{\geq 0}$ denotes the initial time. A schematic of the gait cycle is shown in Figure 2.2. When $\sigma = 1$, the right leg is in the stance phase while the left leg is in the swing phase. Similarly, when $\sigma = 2$, the left leg is in the stance phase and the right leg is in the swing phase. One leg is in the stance phase while the other leg is in the swing phase. The gait cycle n starts at time $t_n^{\sigma=1}$ with the *right leg stance phase* ($\sigma = 1$) when the right heel strike occurs, then transitions to the *right leg swing phase* ($\sigma = 2$) at time $t_n^{\sigma=2}$ when the left heel strike occurs. Finally, the gait cycle n ends at time $t_{n+1}^{\sigma=1}$ with the right heel strike to initiate the next step $n + 1$. The trunk and the upper body are assumed to be fixed in an upright position. During experiments in Chapter 5, a safety harness provides trunk and upper-body support.

To unify the walking dynamics throughout the gait cycle, the walking system can be modeled as a

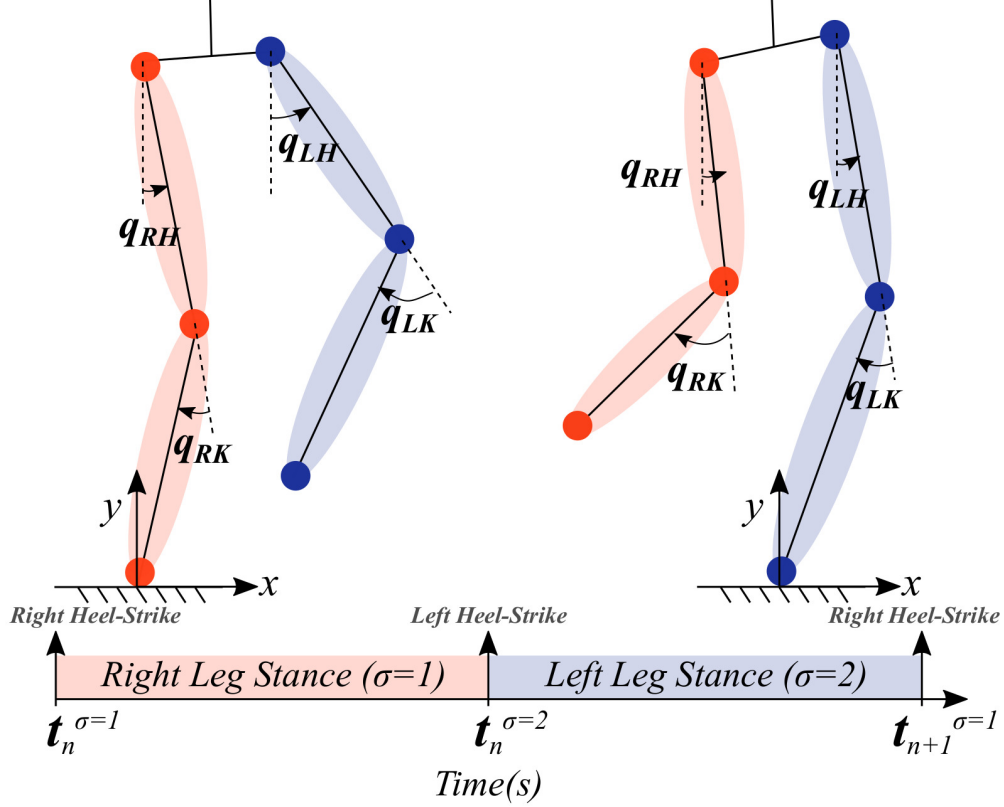


Figure 2.2: Schematic of the lower-limb kinematic chain described by right and left knee, (q_{RK}, q_{LK}) , and hip (q_{RH}, q_{LH}) joint angles, respectively, in both legs with one-point foot contact. The model of the walking dynamics switches based on the signal σ , where $\sigma = 1$ denotes the right leg stance phase, and $\sigma = 2$ denotes the right leg swing phase (i.e., left leg stance phase). The times $t_n^{\sigma=1}$, $t_n^{\sigma=2}$ denote the beginning of each phase, right leg stance, and swing, during step n , respectively.

phase-dependent switched system with the following Euler-Lagrange dynamics

$$M_\sigma(q(t))\ddot{q}(t) + C_\sigma(q(t), \dot{q}(t))\dot{q}(t) + G_\sigma(q(t)) + P_\sigma\dot{q}(t) = B_\rho(q, t)u_\sigma(t), \quad (2.5)$$

where $q = [q_{RH}, q_{RK}, q_{LH}, q_{LK}]^T : \mathbb{R}_{\geq t_0} \rightarrow \mathcal{Q}^4$ denotes the measurable angular positions of the hip (H) and knee (K) for the right (R) and left leg (L), respectively, where $\mathcal{Q} \subset \mathbb{R}$ denote the set of generalized coordinates. The measurable joint velocities are denoted as $\dot{q} : \mathbb{R}_{\geq t_0} \rightarrow \mathbb{R}^4$ and the unmeasurable joint accelerations are denoted as $\ddot{q} : \mathbb{R}_{\geq t_0} \rightarrow \mathbb{R}^4$. The uncertain inertial, centripetal-Coriolis, and gravity effects are denoted by $M_\sigma : \mathcal{Q}^4 \rightarrow \mathbb{R}_{>0}^{4 \times 4}$, $C_\sigma : \mathcal{Q}^4 \times \mathbb{R}^4 \rightarrow \mathbb{R}^{4 \times 4}$, and $G_\sigma : \mathcal{Q}^4 \rightarrow \mathbb{R}^4$, respectively. Additionally, the unknown viscous damping coefficients

are denoted by $P_\sigma \in \mathbb{R}_{\geq 0}^{4 \times 4}$. The control input is denoted as $u_\sigma : \mathbb{R}_{\geq t_0} \rightarrow \mathbb{R}^4$, and the control effectiveness matrix is denoted by $B_\rho : \mathcal{Q}^4 \times \mathbb{R}_{\geq t_0} \rightarrow \mathbb{R}_{> 0}^{4 \times 4}$.

The powered exoskeleton integrates a cable-driven actuation system for each joint to perform bidirectional motion using a pair of Bowden cables that allow joint flexion and extension. Hence, four cables are required to actuate the hip and knee joints in each leg. Additionally, FES is applied to the quadriceps and hamstrings muscle groups to contribute to knee extension and flexion, respectively. The electric motors that actuate hip and knee joints bilaterally are denoted as $e \in \mathcal{E} \triangleq \{1, 2, \dots, 8\}$ and the muscles are denoted as $m \in \mathcal{M} \triangleq \{RQuad, RHam, LQuad, LHam\}$.

The known lumped switched control effectiveness matrix in (2.5) can be defined as

$$B_\rho(q, t) \triangleq \sum_{m \in \mathcal{M}} B_m(q) k_m \rho_m(t) + \sum_{e \in \mathcal{E}} B_e k_e \rho_e(t), \quad (2.6)$$

where $\rho(t) : \mathbb{R}_{\geq t_0} \rightarrow \mathcal{P}$, $\mathcal{P} \subset \mathbb{N}$ is a switching signal that defines the combination of active muscles and motors. The selectable constant control gains for each muscle and motor are denoted as $k_m \in \mathbb{R}_{> 0}$, $\forall m \in \mathcal{M}$ and $k_e \in \mathbb{R}_{> 0}$, $\forall e \in \mathcal{E}$, respectively. Let $j \in \mathcal{J}$, $\mathcal{J} = \{RH, RK, LH, LK\}$ be the joint set. The muscle control effectiveness matrix $B_m : \mathcal{Q}^4 \rightarrow \mathbb{R}^{4 \times 4}$ and the motor control effectiveness matrix $B_e \in \mathbb{R}^{4 \times 4}$ in (2.6) are defined, respectively, as

$$B_m \triangleq \begin{cases} \text{diag}([0, B_{m,j}, 0, 0]) & \text{if } j = RK \\ \text{diag}([0, 0, 0, B_{m,j}]) & \text{if } j = LK \end{cases}, \quad \forall m \in \mathcal{M}, \quad (2.7)$$

$$B_e \triangleq \begin{cases} \text{diag}([B_{e,j}, 0, 0, 0]) & \text{if } j = RH \\ \text{diag}([0, B_{e,j}, 0, 0]) & \text{if } j = RK \\ \text{diag}([0, 0, B_{e,j}, 0]) & \text{if } j = LH \\ \text{diag}([0, 0, 0, B_{e,j}]) & \text{if } j = LK \end{cases}, \quad \forall e \in \mathcal{E}. \quad (2.8)$$

The control effectiveness of each muscle group in (2.7) is a known joint position-and velocity-dependent function denoted as $B_{m,j} : \mathcal{Q} \times \mathbb{R} \times \mathcal{J} \rightarrow \mathbb{R}_{>0}, \forall m \in \mathcal{M}$ that describes the mapping from electrical stimulation intensity on the muscle m to output torque about the knee joint j [45], [46]. Similarly, the control effectiveness of each electric motor in (2.8) is a known positive torque constant denoted as $B_{e,j} \in \mathbb{R}_{>0}, \forall e \in \mathcal{E}$ that maps the current applied to the motor e to output torque on the joint j .

To provide bidirectional movement about each joint, the actuators including muscles and motors are classified as extensors or flexors. The set $\mathbf{Ex} = \{\{RQuad, LQuad\}, \{1, 3, 6, 8\}\}$ contains the muscles and motors that contribute to joint extension, and the set $\mathbf{Fl} = \{\{RHam, LHam\}, \{2, 4, 5, 7\}\}$ contains the muscles and motors that contribute to joint flexion as developed in [47]. The sign of the entries of the control command u_σ dictates the direction of motion such that when $u_\sigma > 0$ indicates joint flexion, and when $u_\sigma < 0$ indicates joint extension. To allocate the control command to the corresponding set of actuators (i.e., flexor or extensor muscles and motors), the piecewise-continuous activation signals $\rho_m : \mathbb{R}_{\geq t_0} \rightarrow \{0, 1\}, \forall m \in \mathcal{M}$ and $\rho_e : \mathbb{R}_{\geq t_0} \rightarrow$

$\{0, 1\}$, $\forall e \in \mathcal{E}$, in (2.6), are defined as

$$\rho_m(t) \triangleq \begin{cases} 1 & \text{if } m \in \mathcal{A} \\ 0 & \text{if } m \notin \mathcal{A} \end{cases}, \quad \rho_e(t) \triangleq \begin{cases} 1 & \text{if } e \in \mathcal{A} \\ 0 & \text{if } e \notin \mathcal{A} \end{cases}, \quad (2.9)$$

where $\mathcal{A} \subset \mathcal{M} \cup \mathcal{E}$ is the set of active actuators defined as

$$\mathcal{A} \triangleq \{a \in \mathcal{M} \cup \mathcal{E} | \exists t \geq t_0, a \in \mathbf{Fl} \wedge u_\sigma(t) > 0, \text{ or } a \in \mathbf{Ex} \wedge u_\sigma(t) < 0\}, \quad (2.10)$$

where, \wedge denotes the logical operator “and”.

Remark 1. Based on the definition of the motor and muscle effectiveness in (2.8) and (2.7), respectively, and the activation signals in (2.9), the switched lumped effectiveness $B_\rho \in \mathbb{R}^{4 \times 4}$ is a positive definite diagonal matrix (i.e., non-singular and B_ρ^{-1} can be computed).

The switched system in (2.5) with control effectiveness matrix defined in (2.6) has the following properties, that are exploited in the subsequent control design and stability analysis.

Property 5. $\underline{m}\|\xi\|^2 \leq \xi^T M_\sigma(q)\xi \leq \overline{m}\|\xi\|^2$, $\forall \xi \in \mathbb{R}^4$, $\forall \sigma \in \mathcal{S}$, where \underline{m} , $\overline{m} \in \mathbb{R}_{>0}$ are known constants [44, Ch. 3].

Property 6. $\xi^T \left(\frac{1}{2} \dot{M}_\sigma - C_\sigma \right) \xi = 0$, $\forall \xi \in \mathbb{R}^4$, $\forall \sigma \in \mathcal{S}$ [44, Ch. 3].

Property 7. $\underline{B}\|\xi\|^2 \leq \xi^T B_\rho(q)\xi \leq \overline{B}\|\xi\|^2$, $\forall \xi \in \mathbb{R}^4$, where \underline{B} , $\overline{B} \in \mathbb{R}_{>0}$ are known constants.

Property 8. The functions M_σ , C_σ , G_σ and P_σ , $\forall \sigma \in \mathcal{S}$ are linearly parameterizable and bounded given bounded arguments [44, Ch. 3].

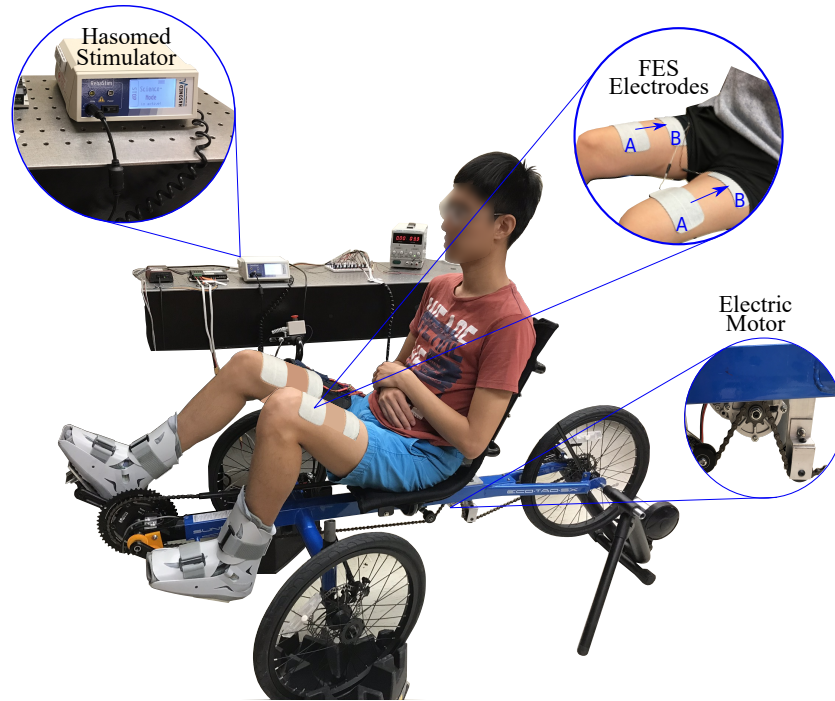


Figure 2.3: Motorized FES-cycling testbed. The cycling system integrates an electric motor mounted on the frame to drive the chain and a portable stimulator that applies a voltage potential using surface electrodes applied on the quadriceps muscle groups.

2.3 Experimental Setup

2.3.1 Motorized FES-Cycling testbed

Treadmill walking experiments are performed using a recumbent cycle (Sun Seeker ECO-TAD SX) mounted on an indoor trainer and adapted with orthotic boots. A brushed 24 VDC electric motor is mounted to drive the chain. An optical encoder (H1, US Digital) installed at the cycle crank measures the crank position. The controller is implemented on a desktop computer (Windows 10 OS) running a real-time target (QUARC 2.6, Quanser) via MATLAB/Simulink 2018a (MathWorks Inc) with a sample rate of 100 Hz. The Quanser QPIDE DAQ board is used to read the encoder signal and to control the analog motor driver (Advanced Motion Controls)² operating in current-controlled mode. A current-controlled stimulator (RehaStim, Hasomed GmbH)

²The servo drive was provided in part by the sponsorship of Advanced Motion Controls.

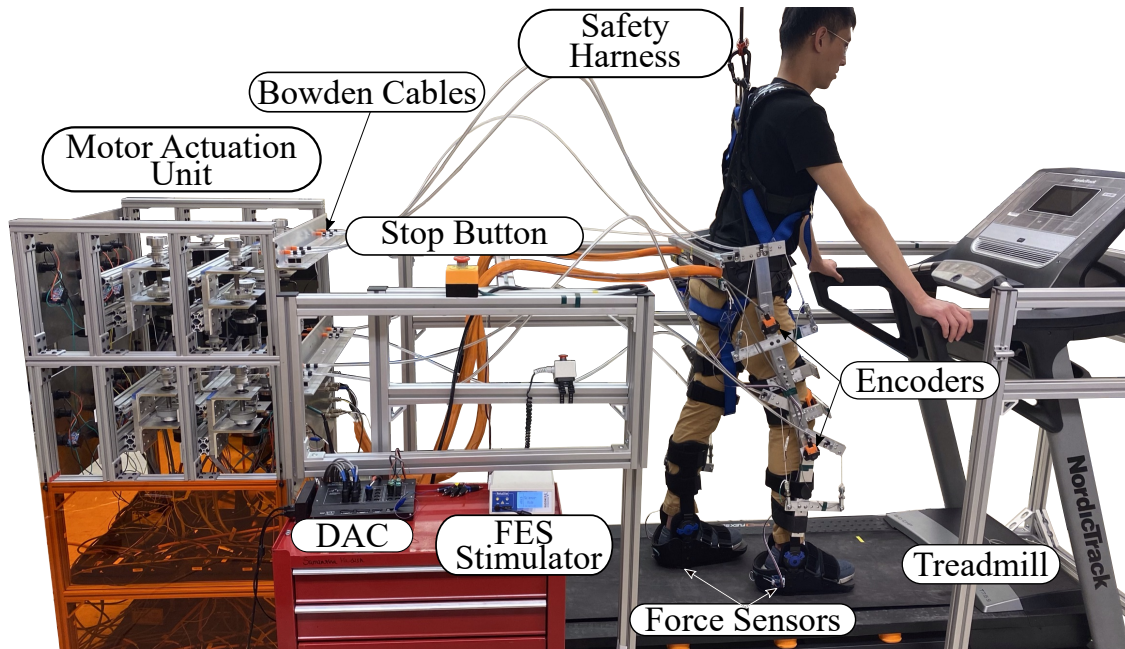


Figure 2.4: Cable-driven lower-limb exoskeleton platform. The system incorporates a hybrid exoskeleton for treadmill walking using a safety harness to provide fall protection. The hybrid exoskeleton combines motors attached to Bowden cables and FES applied to muscles. Encoders are installed on each hip and knee joint and force sensors underneath the sole of the foot to assist with gait phase detection. Real-time data is accessed through the DAC board.

operating in Science Mode delivers biphasic, symmetric, rectangular pulses to the participant's quadriceps muscle groups. Self-adhesive PALS[®] electrodes (3 by 5 inches)³ are placed on each muscle group in both legs as in previous cycling studies [43]. The stimulation current amplitude and stimulation frequency are fixed at 80 mA and 60 Hz, respectively, for all experiments. The crank regions where the muscle groups are stimulated are defined as in [42]. For safety purposes, participants have access to an emergency stop button, and software stop conditions are implemented to limit the amount of motor current that complies with hardware limits, and FES to prevent uncomfortable stimulation intensities.

2.3.2 Lower-limb Cable-Driven Exoskeleton

The experimental testbed is a custom 4-DoF lower-limb exoskeleton for treadmill walking experiments. The exoskeleton is shown in Figure 2.4. The exoskeleton includes mechanical locks that limit the range of motion of each joint to avoid hyper-extension and angles outside of the natural range of motion. Participants wear a safety harness connected to a portable track for fall protection. The weight of the exoskeleton is 17 kg. The platform implements a cable-driven actuation system to preserve backdrivability for each joint, allowing for hybrid actuation (i.e., FES and motor actuation). The actuation system consists of a custom-designed motor actuation unit equipped with 8 brushless DC motors (EC60 Flat 200-400 W, Maxon) to actuate Bowden cables and transmit pulling forces to each joint. The FES stimulator described above was used to evoke muscle contractions in the hamstrings and quadriceps. Two self-adhesive electrodes (3'' by 5'') (PALS, Axelgaard) are placed on each muscle group in both legs. The same stimulation parameters were defined as described in Section 2.3.1. The exoskeleton is equipped with optical encoders (H1-5000-IE-D, US Digital) to measure the hip and knee joint angles. Force sensors (FlexiForce A401, Tekscan) are placed underneath the sole of each foot to detect gait phases. Specifically, the foot sensors are located under the heel and toe (as shown in Figure 2.5) to determine heel strike and toe-off events and integrate them to determine the logic of the switching signal σ (as described in Figure 2.2) using a gait-phase detection algorithm. The algorithm estimates which leg is in stance or swing by comparing the force signals with a predefined threshold configured to detect when each leg is supporting most of the body weight. This approach results in three possible cases: single stance for the right or left leg, or double-stance support. As the current control design assumes double-stance support is negligible compared to the single-stance support phases, the gait detection algorithm ignores double-stance support and waits until the weight is fully transferred from the current stance leg to the other leg to trigger the switching signal. That is, the controller treats the landing leg with the swing model and the stance leg with

³Surface electrodes for the study were provided compliments of Axelgaard Manufacturing Co., Ltd.

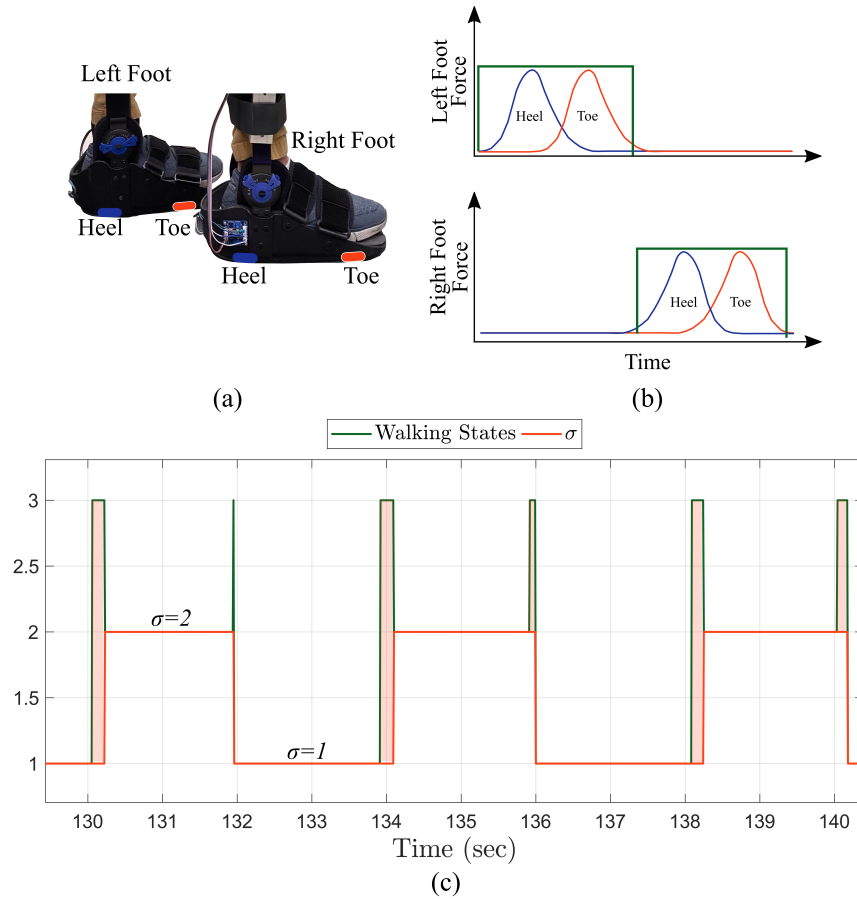


Figure 2.5: Gait phase detection. (a) Force sensors are installed underneath the sole of the foot to detect heel strike and toe-off events. (b) A schematic that illustrates the detection of foot contact based on the heel and toe reaction forces. (c) The logic is generated for each foot to determine the walking states: values 1 and 2 represent right and left stance, respectively, while value 3 represents double stance. The plot illustrates how the switching signal (orange) is generated out of the walking state (green) defined by the force-based phase detection algorithm. It is shown how the double stance support (value 3 in the walking state signal) is not considered for the switching signal σ .

the stance model until lift-off is detected and the body weight is fully supported by the other leg. Thus, the algorithm generates a switching signal that indicates when the subject undergoes right or left stance only. Figure 2.5 illustrates how the algorithm handles the switching events, where the gait phase detected by the forces is depicted in green, and the actual switching signal σ is depicted in orange. It can be observed that σ waits until the full-weight transfer occurs to switch its state.

To maintain satisfactory tension of the cable-driven system, a low-level synchronization con-

troller is used for the electric motors [47], [48]. Prior to each walking experiment, the participants are standing upright and the zero references for all joint angles are calibrated. At this standing position, the cables are tensioned and serve as a reference for the motors to maintain their position and prevent slackness when not activated.

The kinematic control algorithms developed in this dissertation are implemented on a PC (Windows 10 OS) running real-time software (QUARC, Quanser) and interfacing with two digital acquisition boards: QPID-e, and Q8-USB (Quanser) at a rate of 100Hz. Emergency buttons are installed to stop the experiments at any time. Software safeguards are in place to halt the experiment if peak motor currents and large muscle stimulation intensities (e.g., reach FES saturation thresholds) are computed. Prior to the gait experiments for each participant, a walking pretrial is performed with the exoskeleton in passive mode (i.e., allowing free motion), during which joint trajectories were recorded to generate smooth curve fits for the desired walking trajectories q_d, \dot{q}_d , and the foot force thresholds were calibrated to detect the gait phases.

Chapter 3

Switched Adaptive Integral Concurrent Learning for Cadence Tracking

In this chapter and based on the previous work in [36], [49], an adaptive concurrent learning controller is designed for cadence tracking using the cycle-rider model presented in Section 2.1 with switched muscle and motor inputs computed based on the crank angle. A Lyapunov analysis is developed in two phases: 1) the initial phase proves that the switched system remains bounded and achieves asymptotic cadence tracking until a finite time excitation condition is satisfied. 2) The second phase ensures exponential cadence tracking and parameter estimation convergence once the finite excitation condition is satisfied. Experimental results in eight able-bodied individuals and three participants with NCs are discussed for three cycling trials to compare the performance of the adaptive cadence controller under different conditions.

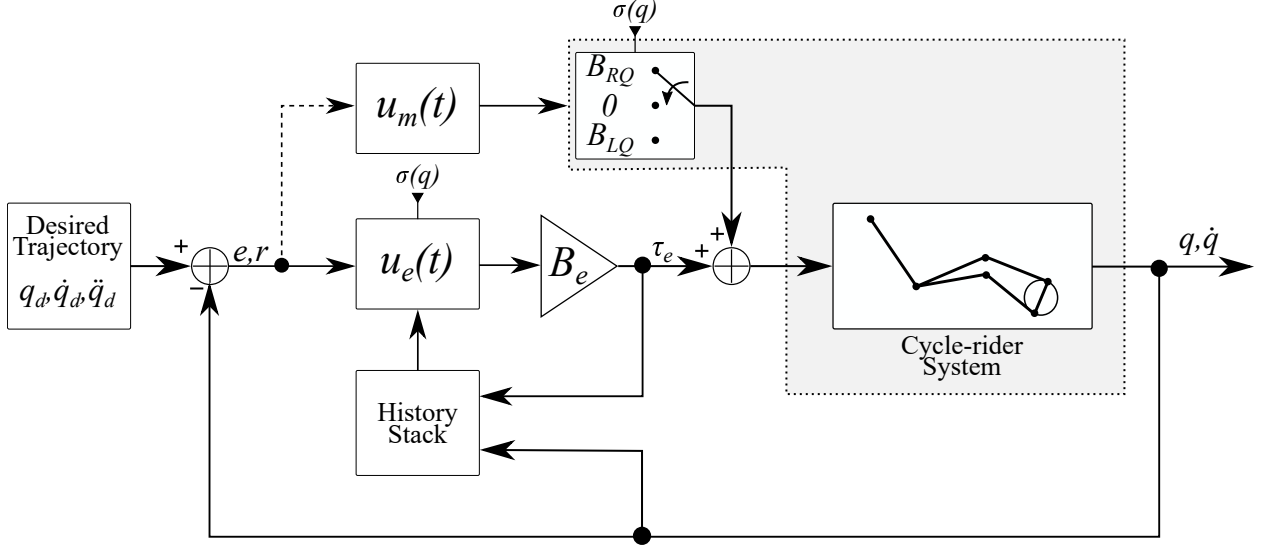


Figure 3.1: Block diagram of the cycle-rider dynamics and the closed-loop feedback control system. The gray shaded area highlights the uncertainty in the cycle-rider dynamics and muscle effectiveness that the adaptive controller seeks to estimate. The electrical motor controller u_e leverages tracking errors e, r and input-output data from the history stack to improve the parameter estimation and achieve cadence tracking. The muscle input also leverages e, r and is delivered to the system through the unknown muscle effectiveness that switches according to $\sigma(q)$.

3.1 Control Development

The block diagram of the cycle-rider closed-loop system is illustrated in Figure 3.1. The control objective is to track desired kinematic trajectories of the crank q_d, \dot{q}_d by combining control inputs from the electric motor u_e in (2.4) and muscle u_m in (2.3). The muscle input is designed as a saturated state feedback controller to ensure bounded muscle torque output, which is suitable for long-duration cycling. The motor control input is designed to estimate the uncertain constant parameters of the cycle-rider system (i.e., the functions in (2.1) are known but the system's parameters are unknown) leveraging input-output data from the history stack and achieve cadence tracking. Through the design of the adaptive update law, the muscle input u_m is embedded into the regressor to strategically account for the switching of muscles during the crank cycle; hence, the unknown constant muscle control effectiveness is lumped into the vector of unknown parameters. Thus, the muscle input u_m , which physically acts as an exogenous saturated input into the system, is exploited as a feedforward term in the cadence electric motor controller.

To quantify the tracking objective, a measurable angular crank position tracking error $e : \mathbb{R}_{\geq t_0} \rightarrow \mathbb{R}$ and auxiliary filtered error $r : \mathbb{R}_{\geq t_0} \rightarrow \mathbb{R}$, are defined as

$$e(t) \triangleq q_d(t) - q(t), \quad (3.1)$$

$$r(t) \triangleq \dot{e}(t) + \alpha e(t), \quad (3.2)$$

where $\alpha \in \mathbb{R}_{>0}$ is a selectable constant control gain and $q_d : \mathbb{R}_{\geq 0} \rightarrow \mathbb{R}$ denotes the desired crank position and is designed with bounded first and second-time derivatives (i.e., $|\dot{q}_d| \leq \xi_1$ and $|\ddot{q}_d| \leq \xi_2$, where $\xi_1, \xi_2 \in \mathbb{R}_{>0}$). After taking the time derivative of (3.2), premultiplying by M , substituting (2.1) and (3.2), and performing algebraic manipulation yields¹

$$M\dot{r} = M(\ddot{q}_d + \alpha\dot{e}) + C(\dot{q}_d + \alpha e) + G + C_d\dot{q} - \tau_m - \tau_e - Cr. \quad (3.3)$$

For the subsequent control design analysis, the torque produced by the muscles τ_m is linearly parameterized as the product of the uncertain constant control effectiveness and the subsequently designed saturated muscle control input. The muscle torque input in (2.3) can be expressed as

$$\tau_m \triangleq y_m(t, \sigma)\theta_m, \quad (3.4)$$

where the switching muscle regressor $y_m : \mathbb{R}_{\geq t_0} \times \mathcal{S} \rightarrow \mathbb{R}^{1 \times 2}$ and the unknown muscle constant parameter vector $\theta_m \in \mathbb{R}^2$ are defined as

$$y_m(t, \sigma) \triangleq \begin{cases} [u_m, 0] & \sigma = RQ \\ [0, 0] & \sigma = KDZ \\ [0, u_m] & \sigma = LQ. \end{cases}, \theta_m \triangleq \begin{bmatrix} B_{RQ} \\ B_{LQ} \end{bmatrix}. \quad (3.5)$$

¹Functional dependencies are omitted henceforth in this chapter unless required for clarification

Leveraging Property 3, the following expression can be obtained

$$y\theta \triangleq M(\ddot{q}_d + \alpha\dot{e}) + C(\dot{q}_d + \alpha e) + G + C_d\dot{q}, \quad (3.6)$$

where $y : \mathcal{Q} \times \mathbb{R} \times \mathbb{R}_{\geq t_0} \rightarrow \mathbb{R}^{1 \times l}$ is a computable regressor vector and $\theta \in \mathbb{R}^l$ is the vector of constant unknown parameters of the cycle-rider system described in the next subsection, where $l \in \mathbb{N}$. Substituting (3.4), (3.6) and (2.4) into (3.3), yields

$$M\dot{r} = Y_\sigma\Theta - B_e u_e - Cr, \quad (3.7)$$

where the lumped switching regressor $Y_\sigma : \mathcal{Q} \times \mathbb{R} \times \mathbb{R}_{\geq t_0} \times \mathcal{S} \rightarrow \mathbb{R}^{1 \times (l+2)}$ and lumped constant parameter vector $\Theta \in \mathbb{R}^{l+2}$ are defined as²

$$Y_\sigma \triangleq [y, -y_m], \Theta \triangleq \begin{bmatrix} \theta \\ \theta_m \end{bmatrix}. \quad (3.8)$$

The parameter estimation error denoted as $\tilde{\Theta} : \mathbb{R}_{\geq t_0} \rightarrow \mathbb{R}^{l+2}$ is defined as

$$\tilde{\Theta}(t) \triangleq \Theta - \hat{\Theta}(t), \quad (3.9)$$

where $\hat{\Theta} : \mathbb{R}_{\geq t_0} \rightarrow \mathbb{R}^{l+2}$ denotes the parameter estimates. The muscle torque input τ_m in (3.4) is segregated into the lumped regressor and lumped constant uncertain parameter vector in (3.8), which facilitates the generation of estimates of both the uncertain parameters of the cycle-rider dynamics and the muscle control effectiveness through the adaptive update law. Thus, the design of the muscle input u_m is decoupled from the design of the electric motor input u_e ; yet, the muscle input directly influences the motor input through the adaptive term. The muscle and electric

²The lumped regressor Y_σ contains the switching muscle regressor y_m . Therefore, Y_σ switches according to the logic state variable σ .

motor control inputs $u_m : \mathbb{R}_{\geq t_0} \rightarrow \mathbb{R}_{>0}$ and $u_e : \mathbb{R}_{\geq t_0} \times \mathcal{S} \rightarrow \mathbb{R}$ are designed, respectively, as

$$u_m(t) \triangleq \text{sat}_{\beta_m}(k_m r + w_m), \quad (3.10)$$

$$u_e(t, \sigma) \triangleq \frac{1}{B_e}(k_e r + e + Y_\sigma \hat{\Theta}), \quad (3.11)$$

where $k_m, k_e \in \mathbb{R}_{>0}$ are selectable positive gains, $w_m \in \mathbb{R}_{\geq 0}$ is an offset muscle stimulation input, which is the minimum input to evoke active muscle torque, and the saturation function is defined as

$$\text{sat}_{\beta_m}(\cdot) \triangleq \begin{cases} (\cdot) & |(\cdot)| \leq \beta_m \\ \beta_m \text{sgn}(\cdot) & |(\cdot)| > \beta_m \end{cases}, \quad (3.12)$$

where $\beta_m \in \mathbb{R}_{>0}$ is a selectable muscle saturation limit. Inspired by [36], the integral concurrent learning (ICL) adaptive update law is designed as

$$\dot{\hat{\Theta}} \triangleq \Gamma Y_\sigma^T r + k_{cl} \Gamma \sum_{i=1}^{\bar{p}} \mathcal{Y}_\sigma^T(t_p) (\mathcal{V}_\sigma(t_p) - \mathcal{Y}_\sigma(t_p) \hat{\Theta}(t)), \quad (3.13)$$

where $k_{cl} \in \mathbb{R}_{>0}$ is a selectable positive constant, $\bar{p} \in \mathbb{N}$ denotes the size of the input-output history stack designed to improve parameter estimation convergence [40], and $\Gamma \in \mathbb{R}^{(l+2) \times (l+2)}$ is a selectable positive definite diagonal matrix, and the time at which the i -th input-output data-point stored in the stack is denoted as $t_p \in [t_0, t]$. The terms $\mathcal{V}_\sigma : \mathbb{R}_{\geq t_0} \rightarrow \mathbb{R}$ and $\mathcal{Y}_\sigma : \mathbb{R}_{\geq t_0} \rightarrow \mathbb{R}^{1 \times (l+2)}$ denote the input and output data, respectively, and are defined as

$$\mathcal{V}_\sigma(t_p) \triangleq B_e \int_{t_p - \delta t}^{t_p} u_e(\gamma, \sigma) d\gamma, \quad (3.14)$$

$$\mathcal{Y}_\sigma(t_p) \triangleq Y_a(q(t), \dot{q}(t), q(t - \delta t), \dot{q}(t - \delta t)) + \int_{t_p - \delta t}^{t_p} Y_b(q(\gamma), \dot{q}(\gamma)) d\gamma - \int_{t_p - \delta t}^{t_p} Y_c(\gamma, \sigma) d\gamma, \quad (3.15)$$

where δt is the integration time window. Since the switching signal σ is piecewise continuous, then the control input u_e within \mathcal{V}_σ in (3.14) and Y_c in (3.15) are integrable. The functions $Y_a :$

$\mathcal{Q}^2 \times \mathbb{R}^2 \rightarrow \mathbb{R}^{1 \times (l+2)}$, $Y_b : \mathcal{Q} \times \mathbb{R} \rightarrow \mathbb{R}^{1 \times (l+2)}$, and $Y_c : \mathbb{R}_{\geq t_0} \times \mathcal{S} \rightarrow \mathbb{R}^{1 \times (l+2)}$ are defined as

$$\begin{aligned} Y_a \Theta &\triangleq M(q(t))\dot{q}(t) - M(q(t - \delta t))\dot{q}(t - \delta t), \\ Y_b \Theta &\triangleq -\dot{M}(q)\dot{q} + C(q, \dot{q})\dot{q} + G(q) + C_d\dot{q}, \\ Y_c \Theta &\triangleq \tau_m(t, \sigma). \end{aligned} \quad (3.16)$$

The dimension of the regressors Y_a, Y_b, Y_c is defined such that they match the dimension of the parameter vector Θ . Using (3.14) and (3.15), integrating both sides of (2.1) over the time window δt , and using integration by parts for the $M\ddot{q}$ term yields

$$Y_a \Theta + \int_{t-\delta t}^t Y_b \Theta d\gamma - \int_{t-\delta t}^t Y_c \Theta d\gamma = \int_{t-\delta t}^t B_e u_e d\gamma, \quad (3.17)$$

$$\mathcal{Y}_\sigma(t) \Theta = \mathcal{V}_\sigma(t). \quad (3.18)$$

Using (3.18), the update law in (3.13) can be rewritten in its analytical form as

$$\dot{\hat{\Theta}} = \Gamma Y_\sigma^T r + k_{cl} \Gamma \left[\sum_{i=1}^{\bar{p}} \mathcal{Y}_\sigma^T(t_p) \mathcal{Y}_\sigma(t_p) \right] \tilde{\Theta}(t). \quad (3.19)$$

Remark 2. The objective of the ICL adaptive update law is to record input-output data to improve the rate of parameter convergence. Hence, the data points at each time t_p are selected based on the algorithm described in [40] to maximize the minimum eigenvalue of the matrix $\left[\sum_{i=1}^{\bar{p}} \mathcal{Y}_\sigma^T \mathcal{Y}_\sigma \right]$ since the minimum eigenvalue is associated with the rate of convergence of the parameter estimation error [32].

Taking the time derivative of the parameter error estimation signal in (3.9) and substituting (3.19) yields

$$\dot{\tilde{\Theta}} = -\Gamma Y_\sigma^T r - k_{cl} \Gamma \Sigma_{\mathcal{Y}} \tilde{\Theta}(t), \quad (3.20)$$

where $\Sigma_{\mathcal{Y}} \triangleq \left[\sum_{i=1}^{\bar{p}} \mathcal{Y}_\sigma^T(t_p) \mathcal{Y}_\sigma(t_p) \right]$ contains the data history stack. The closed-loop error system is obtained after substituting the controller in (3.11) into the open-loop error system in (3.7) and

using (3.9) as

$$M\dot{r} = Y_\sigma \tilde{\Theta} - k_e r - e - Cr. \quad (3.21)$$

Combining (3.2), (3.21) and (3.20), the closed-loop tracking and estimation error systems can be compactly written as

$$\begin{bmatrix} \dot{e} \\ M\dot{r} \\ \dot{\tilde{\Theta}} \end{bmatrix} = \begin{bmatrix} r - \alpha e \\ Y_\sigma \tilde{\Theta} - k_e r - e - Cr \\ -\Gamma Y_\sigma^T r - k_{cl} \Gamma \Sigma_y \tilde{\Theta} \end{bmatrix}, \forall \sigma \in \mathcal{S}. \quad (3.22)$$

3.2 Unknown Constant Parameters

The constant unknown parameter vector in (3.8) of the cycle-rider dynamics in (2.1) obtained from the Euler-Lagrange derivation developed in [13] is defined as

$$\begin{aligned}
 \Theta_1 &= I_c + l_{cc}^2 m_c, \\
 \Theta_2 &= \frac{l_c^2}{l_t^2} (m_t l_{ct}^2 + I_t + m_l l_t^2), \\
 \Theta_3 &= \frac{l_c^3}{l_l l_t^2} (m_t l_{ct}^2 + I_t + m_l l_t^2), \\
 \Theta_4 &= \frac{l_c^3}{l_t^3} (m_t l_{ct}^2 + I_t + m_l l_t^2), \\
 \Theta_5 &= \frac{l_c^2}{l_l^2} (m_l l_{cl}^2 + I_l), \\
 \Theta_6 &= \frac{l_c^3}{l_l^2 l_t} (m_l l_{cl}^2 + I_l), \\
 \Theta_7 &= \frac{l_c^3}{l_l^3} (m_l l_{cl}^2 + I_l), \\
 \Theta_8 &= \frac{l_c^2}{l_l l_t} (m_l l_t l_{cl}), \\
 \Theta_9 &= \frac{l_c^3}{l_l l_t^2} (m_l l_t l_{cl}), \\
 \Theta_{10} &= \frac{l_c^3}{l_l^2 l_t} (m_l l_t l_{cl}), \\
 \Theta_{11} &= l_{cc} m_c g, \\
 \Theta_{12} &= l_c g (m_l + m_t \frac{l_{ct}}{l_t} + m_l \frac{l_{cl}}{l_l}), \\
 \Theta_{13} &= C_d, \\
 \Theta_{14} &= B_{RQ}, \\
 \Theta_{15} &= B_{LQ},
 \end{aligned} \tag{3.23}$$

where g denotes the gravity constant, m_* , I_* denote the mass and moment of inertia, l_* , l_{c*} denote the link lengths and distances to the center of mass, respectively, where $*$ indicates the indexes t, l, c for thigh, shank and crank, respectively. The viscous damping coefficient is denoted by C_d , and B_{RQ} , B_{LQ} denote the muscle effectiveness of the right and left quadriceps, respectively.

3.3 Stability Analysis

The stability analysis of the adaptive cadence tracking controller can be developed through the following two theorems that depend on the FE condition. Theorem 1 proves that the closed-loop error system remains bounded during an initial phase (i.e., the FE condition has not been satisfied, which is quantifiable using the data stored in the history stack). Theorem 2 proves exponential convergence of the kinematic tracking and parameter estimation errors of the switched system (i.e., the FE condition has been satisfied and verified). The FE condition is specified in the following assumption.

Assumption 2. Let $\lambda_{\min}\{\cdot\}$ denote the minimum eigenvalue of a given matrix and $\underline{\lambda} \in \mathbb{R}_{>0}$ the excitation condition. The system is said to be sufficiently excited after a finite time $T \in \mathbb{R}_{>t_0}$ such that $\exists \underline{\lambda} : \forall t > T, \lambda_{\min}\{\Sigma_Y\} \geq \underline{\lambda}$.

Theorem 1. The controller in (3.11) and the adaptive update law in (3.13) achieve bounded trajectory tracking and parameter estimation over the interval $t \in [t_0, T)$ in the sense that

$$\|z(t)\| \leq \sqrt{\frac{\beta_2}{\beta_1}} \|z(t_0)\|. \quad (3.24)$$

Proof. Let $V : \mathbb{R} \times \mathbb{R} \times \mathbb{R}^{l+2} \times \mathbb{R}_{\geq t_0} \rightarrow \mathbb{R}$ be a positive definite, continuously differentiable, Lyapunov function candidate defined as

$$V(e, r, \tilde{\Theta}, t) = \frac{1}{2}e^2 + \frac{1}{2}Mr^2 + \frac{1}{2}\tilde{\Theta}^T \Gamma^{-1} \tilde{\Theta}, \quad (3.25)$$

where the following inequalities are satisfied

$$\beta_1 \|z\|^2 \leq V(z, t) \leq \beta_2 \|z\|^2, \quad (3.26)$$

where $\beta_1 \triangleq \min\{\frac{1}{2}, \frac{m}{2}, \frac{1}{2}\lambda_{\min}\{\Gamma^{-1}\}\}$, $\beta_2 \triangleq \max\{\frac{1}{2}, \frac{m}{2}, \frac{1}{2}\lambda_{\max}\{\Gamma^{-1}\}\}$ and $z : \mathbb{R}_{\geq t_0} \rightarrow \mathbb{R}^{l+4}$ is the

lumped state vector defined as

$$z \triangleq [e, r, \tilde{\Theta}^T]^T. \quad (3.27)$$

Let $z(t)$ be the Filippov solution to the differential inclusion $\dot{z} \in K[h](z, t)$, where $K[\cdot]$ is the Filippov regularization as in [50], and $h \triangleq [\dot{e}, M\dot{r}, \dot{\tilde{\Theta}}^T]^T$. Moreover, let $K'_\sigma[h](z, t)$ be the collection of regularized systems generated by the switching signal σ , defined as

$$K'_\sigma[h](z, t) = \begin{bmatrix} r - \alpha e \\ \{Y_\sigma \tilde{\Theta}\} - k_e r - e - Cr \\ \{-\Gamma Y_\sigma^T r\} - k_{cl} \Gamma K[\Sigma_{\mathcal{Y}}] \tilde{\Theta} \end{bmatrix}. \quad (3.28)$$

Note that $K[h](z, t) \subseteq K'_\sigma[h](z, t)$ as proved in [41]. Since the Lyapunov function candidate in (3.25) is continuously differentiable, the Clarke generalized gradient of (3.25) reduces to ∇V . Leveraging Property 2, and considering the FE is not yet satisfied, i.e., for $t \in [t_0, T) \implies 0 \leq \lambda_{\min}\{\Sigma_{\mathcal{Y}}\} < \underline{\lambda}$, a bound on the generalized derivative along the set of solutions in (3.28) can be defined as [41]

$$\begin{aligned} \dot{V} &\leq \max_{x \in K'_\sigma[h]} [e, r, \tilde{\Theta}^T, \tfrac{1}{2}r^2 \dot{M}] \cdot [x, 1]^T, \\ &\leq -W_1(z), \end{aligned} \quad (3.29)$$

where $W_1(z) = \alpha \|e\|^2 + k_e \|r\|^2$ is a positive semi-definite function. Thus, invoking [41, Th. 2], $W_1(z) \rightarrow 0$ as $t \rightarrow \infty$. Since $V \geq 0$ and $\dot{V} \leq 0$, $V \in \mathcal{L}_\infty$ implies $z \in \mathcal{L}_\infty$ and $V(z(t)) \leq V(z(t_0))$. Using (3.26), the bound in (3.24) holds for $t \in [t_0, T)$. Since $z \in \mathcal{L}_\infty$ then $\dot{e} \in \mathcal{L}_\infty$ from (3.2), and $\hat{\Theta} \in \mathcal{L}_\infty$ from (3.9). Moreover, $q, \dot{q} \in \mathcal{L}_\infty$ from (3.1) and (3.2) which implies, along with the fact that $u_m \in \mathcal{L}_\infty$ from (3.10), that $Y_\sigma \in \mathcal{L}_\infty$ in (3.8) and $u_e \in \mathcal{L}_\infty$ in (3.11), which implies that $\mathcal{Y}_\sigma, \mathcal{V}_\sigma \in \mathcal{L}_\infty$ in (3.18) and $\tau_e \in \mathcal{L}_\infty$ in (2.4), and along with the fact that $\tau_m \in \mathcal{L}_\infty$ yields $\ddot{q} \in \mathcal{L}_\infty$ in (2.1). ■

Theorem 2. *Given the closed-loop error system in (3.22), the controller in (3.11) and the adaptive update law in (3.13) achieve exponential kinematic tracking and parameter estimation error*

convergence in the sense that

$$\|z(t)\| \leq \frac{\beta_2}{\beta_1} \|z(t_0)\| \exp\left(-\frac{\psi}{2\beta_2}(t-T)\right), \quad (3.30)$$

where $\psi \triangleq \min\{\alpha, k_e, \underline{\lambda}\}$.

Proof. Let $V : \mathbb{R} \times \mathbb{R} \times \mathbb{R}^{l+2} \times \mathbb{R}_{\geq t_0} \rightarrow \mathbb{R}$ be the Lyapunov function candidate defined in (3.25).

A bound on the generalized derivative along the solutions in (3.28) can be defined as

$$\begin{aligned} \dot{V} &\leq \max_{x \in K'_\sigma[h]} [e, r, \tilde{\Theta}^T, \frac{1}{2}r^2\dot{M}] \cdot [x, 1]^T, \\ &\leq -W_2(z), \end{aligned} \quad (3.31)$$

where $W_2(z) = \alpha\|e\|^2 + k_e\|r\|^2 + \underline{\lambda}\|\tilde{\Theta}\|^2$ is a positive definite function leveraging Assumption 2, where the FE is satisfied, i.e., for $t \in [T, \infty) \implies \lambda_{\min}\{\Sigma_Y\} \geq \underline{\lambda}$. Using the bounds in (3.26), the system achieves exponential tracking and estimation error convergence for $t \geq T$ in the sense of

$$\|z(t)\| \leq \sqrt{\frac{\beta_2}{\beta_1}} \|z(T)\| \exp\left(-\frac{\psi}{2\beta_2}(t-T)\right), \quad (3.32)$$

Furthermore, substituting the result in (3.24) with $t = T$ into (3.32) yields (3.30). Since $V \geq 0$ and $\dot{V} \leq 0$, $V \in \mathcal{L}_\infty$ implies $z \in \mathcal{L}_\infty$, then $\dot{e}, \hat{\theta} \in \mathcal{L}_\infty$ in (3.2) and (3.9), respectively. Moreover, $q, \dot{q} \in \mathcal{L}_\infty$ in (3.1) and (3.2) which implies $Y_\sigma \in \mathcal{L}_\infty$ in (3.8) since $u_m \in \mathcal{L}_\infty$ in (3.10). Further, $u_e \in \mathcal{L}_\infty$ in (3.11), which implies that $\mathcal{Y}_\sigma, \mathcal{V}_\sigma \in \mathcal{L}_\infty$ in (3.18) and $\tau_e \in \mathcal{L}_\infty$ in (2.4) yields $\ddot{q} \in \mathcal{L}_\infty$ in (2.1) since $\tau_m \in \mathcal{L}_\infty$. ■

3.4 Experiments

The electric motor and muscle controllers designed in (3.11) and (3.10), respectively, and the adaptive update law in (3.13) were implemented during real-time cycling trials. The muscle input

Table 3.1: Demographics of subjects with neurological conditions

Subject	Age	Sex	Injury	Months Since Injury
P1	67	F	Right Side Hemiparetic Stroke	76
P2	60	M	L1 SCI	365
P3	51	M	T11-T12 SCI	232

was computed as stimulation pulse width to activate the left and right quadriceps muscle groups and the motor input was computed as current. Eight able-bodied individuals (6 males and 2 females) with ages ranging between 22 and 30 years, and three individuals (2 males and 1 female) with neurological conditions participated in the FES-cycling experiments at Syracuse University. Demographics of the participants with NCs are presented in Table 3.1. Prior to participation, written informed consent was obtained from all participants as approved by the Institutional Review Board (IRB) at Syracuse University. Participants were instructed to avoid voluntarily contributing to pedaling and were not informed of the desired and actual trajectories.

3.4.1 Experimental Protocol

Three 10-minute (600 sec) cycling experiments (EXP) were conducted with all able-bodied participants, while 5-minute (300 sec) trials were conducted in participants with NCs. Due to the limited availability of the participants, all cycling trials were conducted during the same session with ten-minute rest breaks in between trials using the experimental testbed described in Section 2.3.1. **EXP1:** this cycling trial implements the desired *trajectory 1* in (3.33) in which the cadence gradually increases until it reaches a steady-state value of 55 revolutions per minute (RPM). The concurrent learning algorithm initializes the update law in (3.13) with an empty history stack. **EXP2:** this cycling trial implements the desired *trajectory 2* in (3.34), which is a staircase-like trajectory during the transient phase and remains constant at 55 RPM until the end of the experiment. The update law in (3.13) is also initialized with the history stack empty as in EXP1. **EXP3:** this cycling trial implements the desired *trajectory 1* and it exploits the history

stack collected in EXP2; hence, the cadence controller u_e is initialized exploiting the adaptive estimates collected in EXP2 (i.e., with previously learned parametric estimates of the cycle-rider system and muscle control effectiveness) and keeps computing the update law in (3.13) with the instantaneous tracking error r and the recorded history stack without collecting new input-output data. The desired trajectories are implemented by computing the desired crank accelerations in (3.33) and (3.34) and then performing numerical integration to obtain the desired cadence and crank angular position³. The desired acceleration to compute the steady-state constant cadence in *trajectory 1* is defined as

$$\ddot{q}_{d1} \triangleq 1.75\text{sech}^2(0.6(t - 5)), \quad (3.33)$$

and the desired acceleration to compute the staircase cadence in *trajectory 2* is defined as

$$\begin{aligned} \ddot{q}_{d2} \triangleq & 2.5\text{sech}^2(t - 5) + 0.25\text{sech}^2(t - 31) \\ & + 0.25\text{sech}^2(t - 57) + 0.25\text{sech}^2(t - 83) \\ & + 0.25\text{sech}^2(t - 109) - 0.25\text{sech}^2(t - 135) \\ & - 0.25\text{sech}^2(t - 161), \end{aligned} \quad (3.34)$$

which reaches an initial constant speed of 5 rad/s (47.7 RPM) and subsequently increases to 5.5 (52.5), 6 (57.3), 6.5 (62.1), and 7 (66.8) rad/s (RPM), decreases the speed to 6.5 (62.1), and then finally settles to a steady-state constant speed of 6 rad/s (57.3 RPM). Each speed level prior to the steady-state cadence was maintained for 20 seconds. The ICL algorithm comprises two phases. In the initial phase, input-output data is collected to populate the history stack Σ_Y and satisfy the FE condition (see Assumption 2 in Section 3.3), which for the real-time cycling experiments was set to $\underline{\lambda} = 0.001$. Once the history stack satisfies the FE condition, the adaptive controller stops recording new data and only leverages the already-stored data to achieve parameter convergence.

The control gains and parameters in (3.2), (3.10), (3.11), and (3.13) were defined as follows for all cycling experiments across participants: $k_e = 0.7$, $k_m = 0.1$, $\beta_m = [70, 90]\mu s$, $w_m = [0.2, 0.4]$

³This approach to implement the desired cadence trajectories is practical and convenient to generate smooth staircase-like trajectories, i.e., thus, allowing changes in the steady state target cadence.

(normalized pulsewidth with respect to β_m), $\alpha = 0.1$, $k_{cl} = 0.1$, $\Gamma = 0.0001 * \text{eye}(15)$, $\delta t = 0.03\text{s}$, $\bar{p} = 30$, $\hat{\Theta}(t_0) = \text{zeros}(15, 1)$ for EXP1 and EXP2 and $\hat{\Theta}(t_0) = \hat{\Theta}(t_{EXP2} = 600)$ for EXP3.

3.4.2 Results

The tracking performance for the able-bodied participants (S1-S8) is summarized in Table 3.2, and Table 3.3 presents the tracking performance obtained for the subjects with NCs (P1-P3). Note in Table 3.3 that P3 did not perform EXP2. This was due to the participant's discomfort to cycle at high speeds. Thus, P3 performed EXP1 and EXP3 at a lower speed (35 RPM) than the other participants. Both tables show the root-mean-square (RMS) position error, average percentage cadence error computed as $\bar{e}(\%) = \frac{|\dot{q}_d - \dot{q}|}{\dot{q}_d} \cdot 100\%$, RMS cadence error \dot{e} , and RMS of the steady-state cadence error \dot{e}_{ss} , which is computed for the last 400 seconds of each trial in the able-bodied participants, and for the last 90 seconds in the participants with NCs, across the three cycling experiments. Figure 3.2 illustrates cadence tracking performance and the position and filtered tracking errors e, r in (3.1), (3.2), respectively, for a subset (S1-S5) of the able-bodied participants undergoing EXP1. The tracking performance for the same subset of participants undergoing EXP2 and EXP3 is illustrated in Figure 3.3 and Figure 3.4, respectively. The parameter estimates obtained during EXP1 (left column) and EXP2 (right column) are illustrated in Figure 3.5 for S1-S5. Figure 3.6 depicts the minimum eigenvalue of the history stack (i.e., $\lambda_{\min}\{\Sigma_Y\}$) in (3.13) during EXP1 and EXP2 for participants S1-S5. The control inputs generated across all trials for subject S4 are illustrated in Figure 3.7, where the normalized motor and muscle inputs are depicted on the left column and the applied FES inputs on the quadriceps muscle groups are depicted on the right column. Figure 3.8 depicts the control inputs for S4 in EXP1 across ten crank cycles as a representative example. The control contribution of each term in the electric motor controller u_e in (3.11) is illustrated in Figure 3.9 for participants S1-S5 in EXP2, where the contribution of the adaptive term $Y_\sigma \hat{\Theta}$ is depicted in blue and the contribution of the state feedback term $k_e r + e$ is depicted in orange. The tracking performance for the participants

Table 3.2: Tracking results for able-bodied participants: RMS position error e for the full experiment (10 minutes), average cadence percentage error $\bar{e}(\%)$, RMS velocity error \dot{e} (RPM) for the full experiment, and RMS steady-state cadence error \dot{e}_{ss} (RPM) for the last 400 seconds of each trial

Participant	EXP1				EXP2				EXP3			
	e (rad) RMS	\bar{e} (%)	\dot{e} (RPM) RMS	\dot{e}_{ss} (RPM) RMS	e (rad) RMS	\bar{e} (%)	\dot{e} (RPM) RMS	\dot{e}_{ss} (RPM) RMS	e (rad) RMS	\bar{e} (%)	\dot{e} (RPM) RMS	\dot{e}_{ss} (RPM) RMS
S1	1.51	2.94 ± 2.77	2.94	1.41	1.10	2.95 ± 2.05	2.88	2.02	0.44	3.60 ± 2.50	2.97	2.45
S2	1.08	2.09 ± 1.69	2.52	1.38	1.19	2.15 ± 2.00	3.21	1.41	0.47	1.68 ± 1.35	2.33	1.16
S3	0.88	2.09 ± 1.65	2.26	1.40	1.19	2.47 ± 2.03	2.70	1.69	0.58	2.42 ± 1.94	2.62	1.61
S4	0.98	2.08 ± 1.84	2.45	1.36	1.05	3.08 ± 1.98	2.81	2.10	0.38	3.10 ± 1.98	2.86	2.21
S5	0.80	3.26 ± 2.18	2.76	2.35	0.77	3.21 ± 2.17	2.43	2.23	0.28	4.32 ± 2.33	2.88	2.87
S6	0.77	2.60 ± 2.02	3.08	1.75	1.34	2.32 ± 2.67	2.94	1.42	1.73	2.39 ± 3.74	3.86	1.45
S7	0.46	2.74 ± 2.38	2.29	1.71	0.47	2.23 ± 2.36	2.10	1.29	0.56	2.81 ± 1.87	2.07	2.01
S8	0.47	1.68 ± 1.53	1.65	1.09	0.54	2.41 ± 2.45	2.20	1.53	0.37	2.31 ± 1.64	1.90	1.69
Mean	0.87	2.43	2.49	1.56	0.96	2.60	2.66	1.71	0.60	2.82	2.69	1.93
STD	0.32	2.00*	0.42	0.36	0.30	2.21*	0.36	0.34	0.44	2.16*	0.58	0.53

* Reports the mean over the standard deviations.

Table 3.3: Tracking results for participants with NCs: RMS position error e for the full experiment (5 minutes), average cadence percentage error $\bar{e}(\%)$, RMS velocity error \dot{e} (RPM) for the full experiment, and RMS steady-state cadence error \dot{e}_{ss} (RPM) for the last 90 seconds of each trial

Participant	EXP1				EXP2				EXP3			
	e (rad) RMS	\bar{e} (%)	\dot{e} (RPM) RMS	\dot{e}_{ss} (RPM) RMS	e (rad) RMS	\bar{e} (%)	\dot{e} (RPM) RMS	\dot{e}_{ss} (RPM) RMS	e (rad) RMS	\bar{e} (%)	\dot{e} (RPM) RMS	\dot{e}_{ss} (RPM) RMS
P1	0.98	2.45 ± 2.03	2.41	1.27	0.94	2.13 ± 1.68	2.43	1.39	0.92	3.39 ± 2.32	2.46	1.84
P2	0.83	2.96 ± 2.09	2.53	1.67	1.07	2.35 ± 1.96	2.77	1.57	0.55	2.76 ± 2.22	2.46	1.66
P3	1.36	11.58 ± 7.03	4.52	4.91	—	—	—	—	0.40	14.68 ± 7.89	5.50	5.57
Mean	1.06	5.66	3.15	2.62	1.01	2.24	2.60	1.48	0.62	6.94	3.47	3.02
STD	0.22	3.71*	0.97	1.63	0.07	1.82*	0.17	0.09	0.22	4.14*	1.43	1.80

* Reports the mean over the standard deviations.

with NCs undergoing EXP1 is illustrated in Figure 3.10.

3.5 Discussion

The experimental results demonstrate the feasibility of the controllers developed in (3.10) and (3.11) to track desired cadence trajectories during ten-minute trials with able-bodied individuals, where the average RMS cadence tracking error for able-bodied participants was 2.49 ± 0.42 RPM (2.43 ± 2.00 % error) for EXP1, 2.66 ± 0.36 RPM (2.60 ± 2.21 % error) for EXP2, and 2.69 ± 0.58 RPM (2.82 ± 2.16 % error) for EXP3. Additionally, the average steady-state RMS cadence tracking

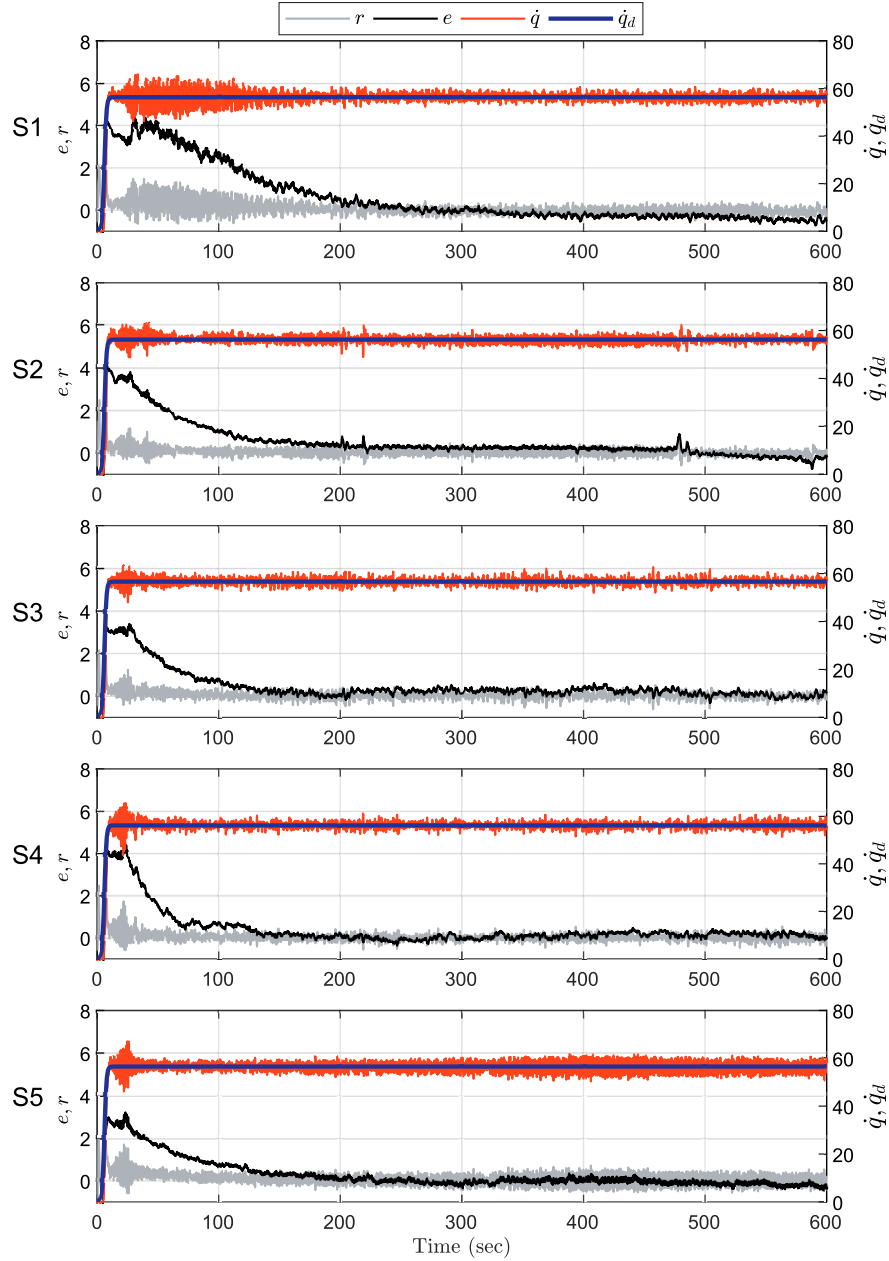


Figure 3.2: Kinematic tracking for cycling trial **EXP1** (using *trajectory 1* in (3.33)). Cadence tracking (actual versus desired angular speed) in RPM, position error $e(t)$ (rad), and filtered error $r(t)$ (computed using e (rad) and \dot{e} (rad/sec)) are depicted. Each row corresponds to the cycling performance of one participant for subjects S1-S5.

error for healthy participants was 1.56 ± 0.36 RPM for EXP1, 1.71 ± 0.34 RPM for EXP2, and 1.93 ± 0.53 RPM for EXP3. Moreover, the average RMS position error for healthy participants was 0.87 ± 0.32 , 0.96 ± 0.30 , and 0.60 ± 0.44 rad for the three different trials, respectively. Results in participants with NCs were obtained with an average cadence tracking error of 3.15 ± 0.97

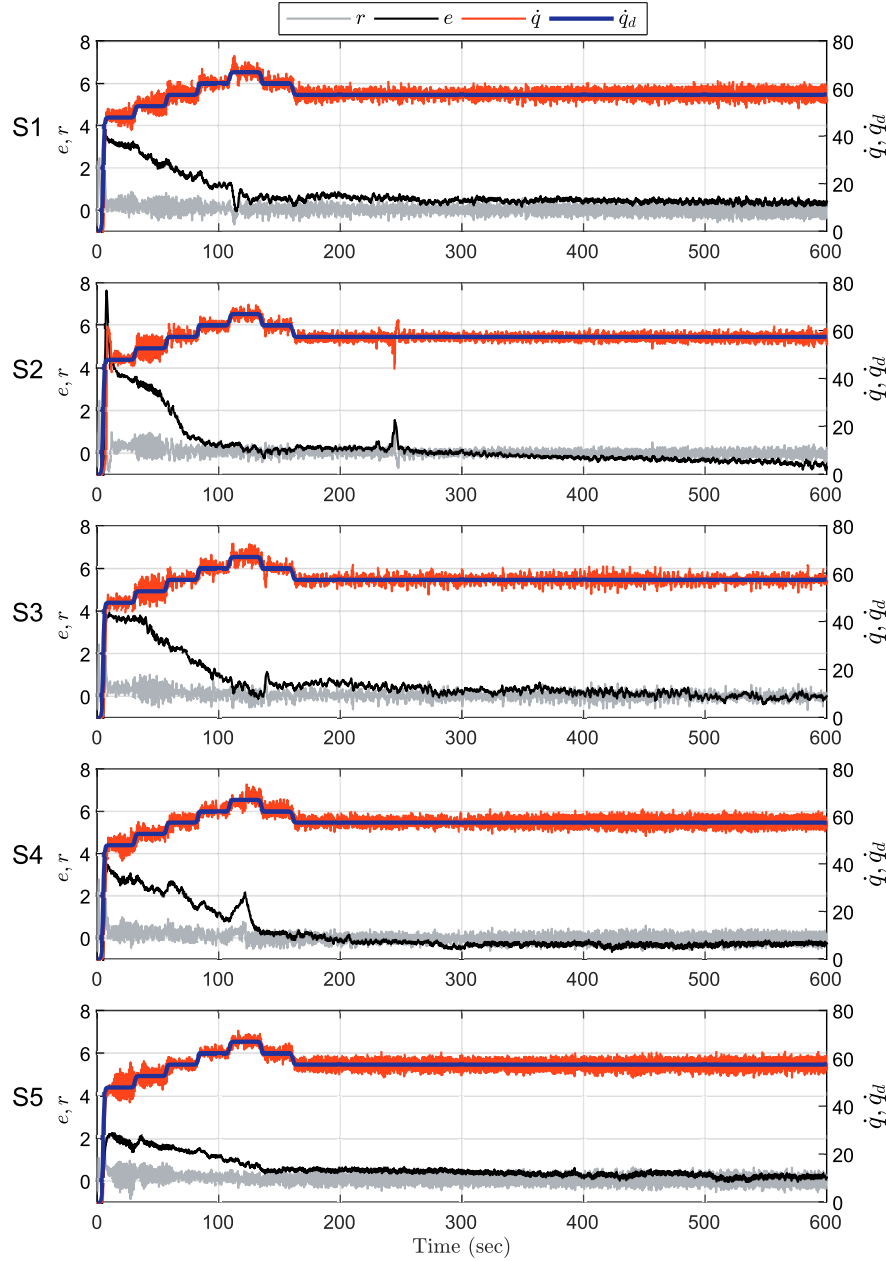


Figure 3.3: Kinematic tracking for **EXP2** (using *trajectory 2* in (3.34)). Cadence tracking (RPM), position error $e(t)$ (rad) and filtered error $r(t)$ (computed using e (rad) and \dot{e} (rad/sec)) are depicted. Each row corresponds to the performance of one participant.

RPM (5.66 ± 3.71 % error), 2.60 ± 0.17 RPM (2.24 ± 1.82 % error), and 3.47 ± 1.43 RPM (6.94 ± 4.14 % error) for the three trials, respectively. Additionally, the average steady-state RMS cadence tracking error of 2.62 ± 1.63 , 1.48 ± 0.09 , and 3.02 ± 1.80 RPM were obtained. Finally, an average RMS position error of 1.06 ± 0.22 , 1.01 ± 0.07 , and 0.62 ± 0.22 rad, were obtained

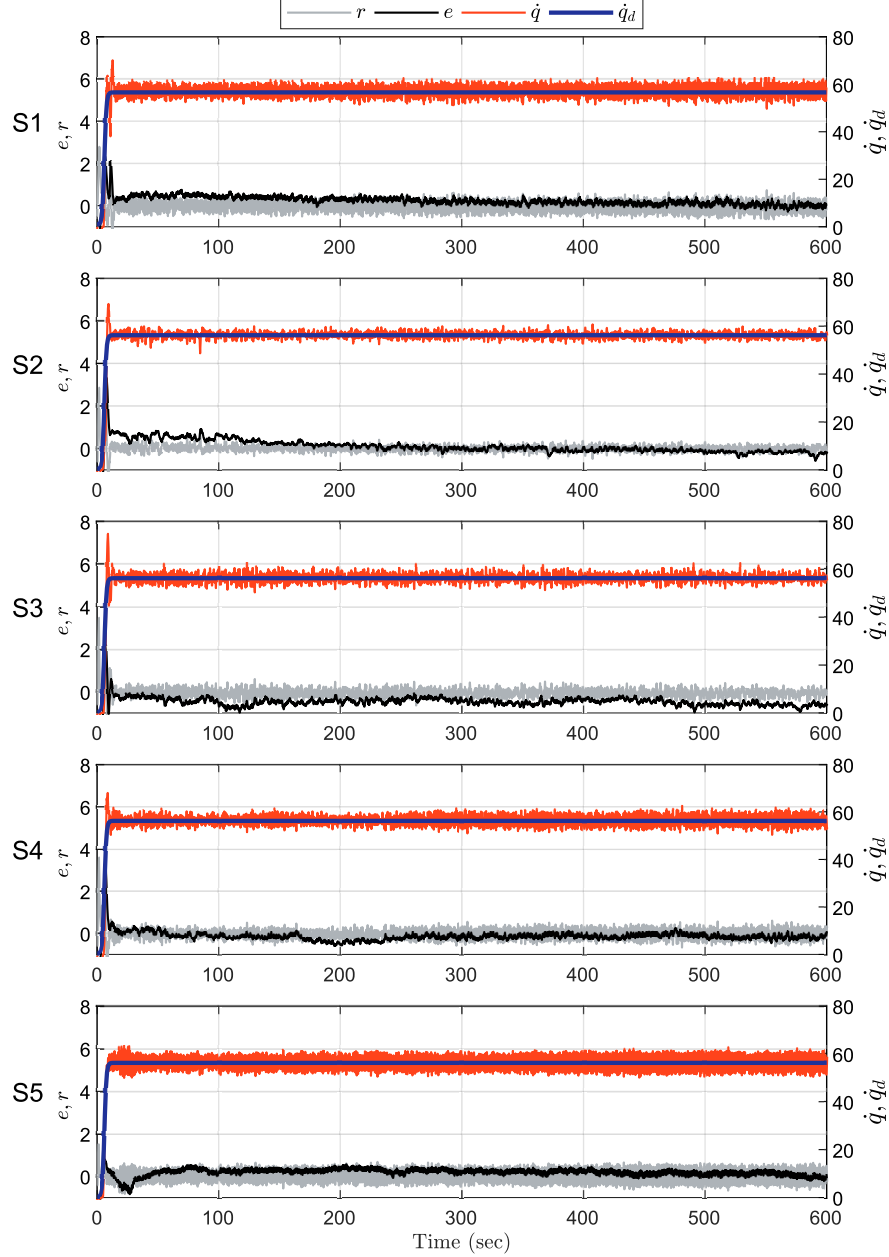


Figure 3.4: Kinematic tracking for **EXP3** (using *trajectory 1* in (3.33)). Cadence tracking (RPM), position error $e(t)$ (rad) and filtered error $r(t)$ (computed with e (rad) and \dot{e} (rad/sec)) are shown. Each row corresponds to the cycling performance of one participant.

for the three trials. The main objective of the experimental protocol was to analyze the behavior of the concurrent learning controller and parameter estimation under different learning conditions. The results successfully demonstrate the ability of the system to perform under different types of trajectories and the availability of previously-learned data.

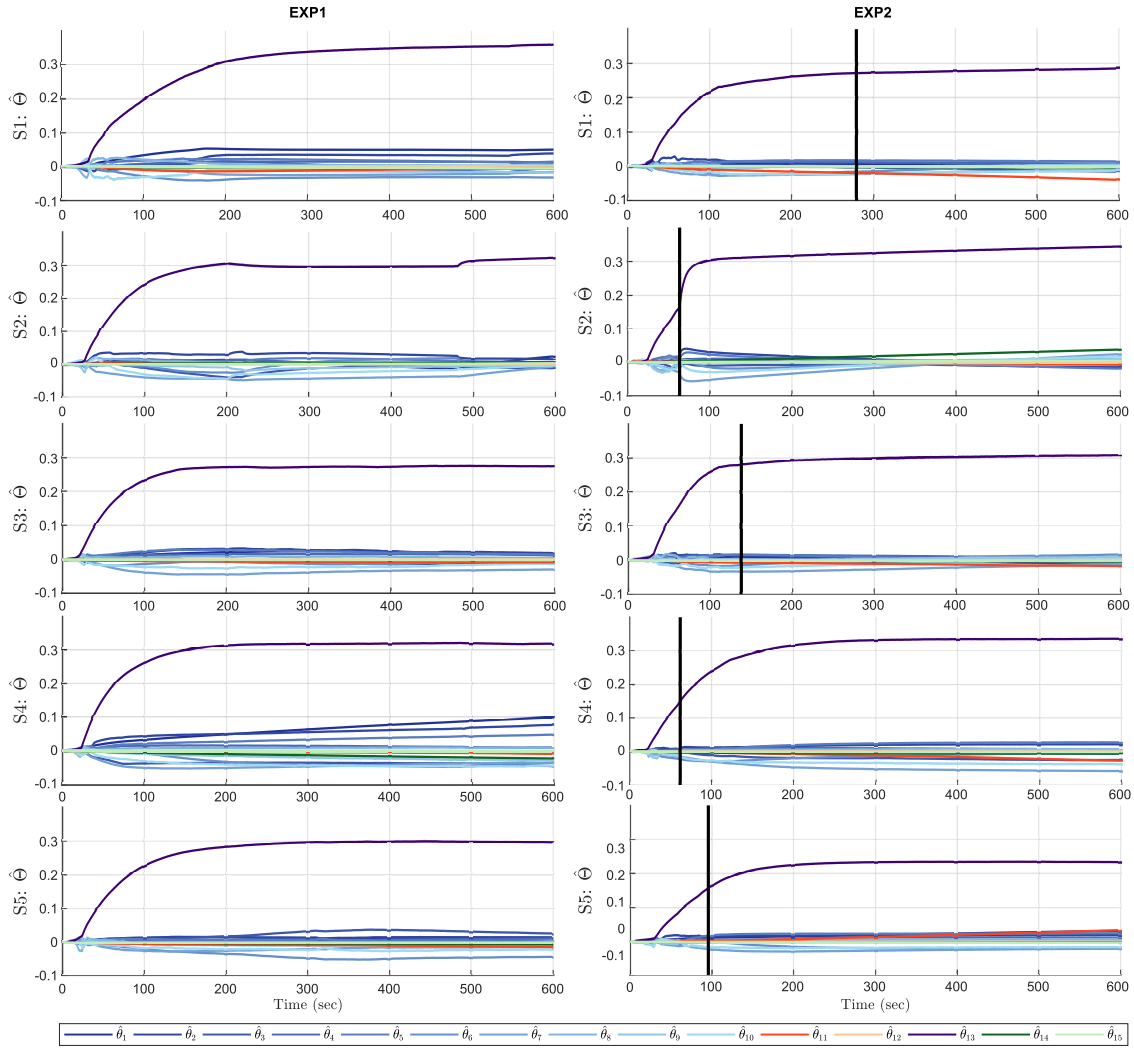


Figure 3.5: Parameter estimates for each participant during the 10-minute experiments. The left column displays the estimates in **EXP1** and the right column shows the estimates in **EXP2**. The vertical line depicts the instance at which the predetermined FE condition based on $\underline{\lambda}$ in EXP2 is satisfied. Cycling trials corresponding to EXP1 did not satisfy the predefined FE condition; nevertheless, the minimum eigenvalue for all trials in EXP1 is positive as depicted in Figure 3.6. Section 3.2 describes the vector of parameters estimated during the cycling experiments.

3.5.1 Tracking error performance and convergence

As depicted in Figure 3.2-3.4, the filtered tracking error r remains bounded and settles around zero (± 0.5) for all experiments. Likewise, the position error e converges to zero (i.e., reaches the error window of ± 0.5 rad) for all trials with able-bodied individuals; it can be observed that e converges faster in EXP3 (12.15 ± 6.86 seconds), compared to EXP1 (91.50 ± 51.26 seconds) and

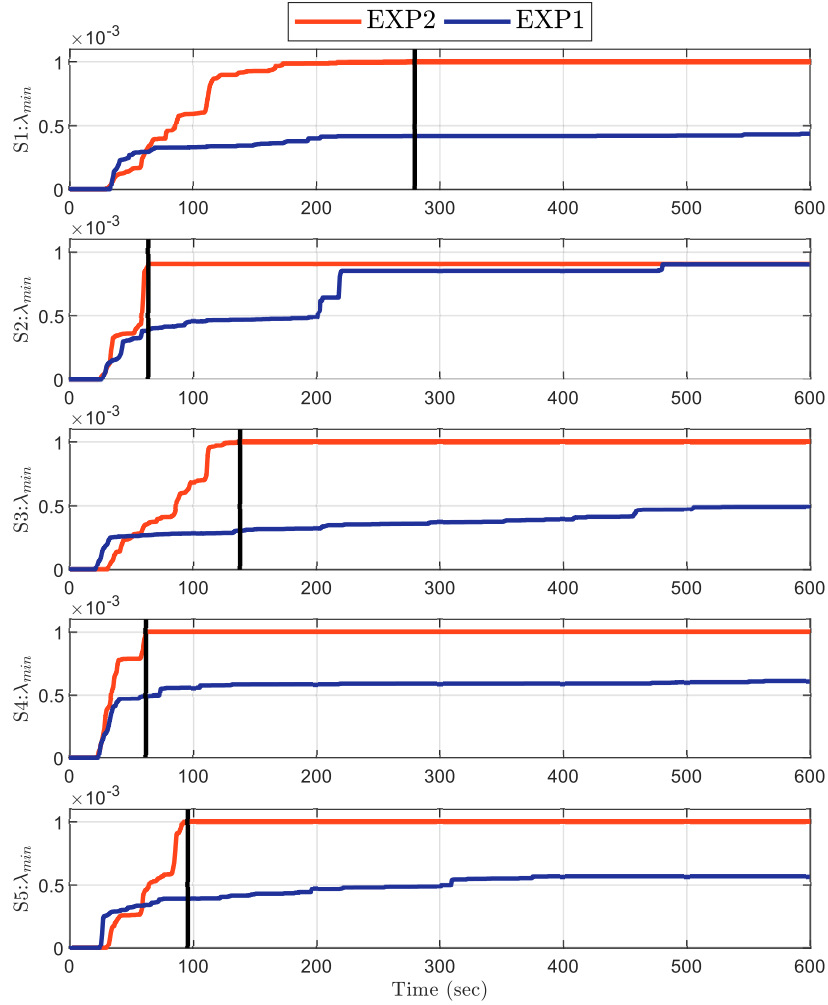


Figure 3.6: Minimum eigenvalue of the history stack, i.e., $\lambda_{\min}\{\Sigma_Y\}$. The eigenvalues for **EXP1** and **EXP2** are shown in blue and red, respectively. The vertical line indicates the time at which the FE excitation condition is satisfied in EXP2.

EXP2 (91.70 ± 35.79 seconds). This phenomenon can be attributed to the fact that the cadence controller in EXP3 used previously-recorded data from EXP2 in the history stack such that the adaptive estimates in EXP3 are initialized with the learned estimates obtained at the end of EXP2. Hence, the cycling trial EXP3 differs from the cycling trials EXP1 and EXP2 in which the adaptive update law and cadence controller are initialized with an empty history stack (i.e., adaptive estimates are initialized to zero). The tracking performance and convergence were satisfactory across the three experiments for all participants (able-bodied and participants with NCs) independently of the initial conditions of the adaptive estimates (e.g., starting the cycling trial with an

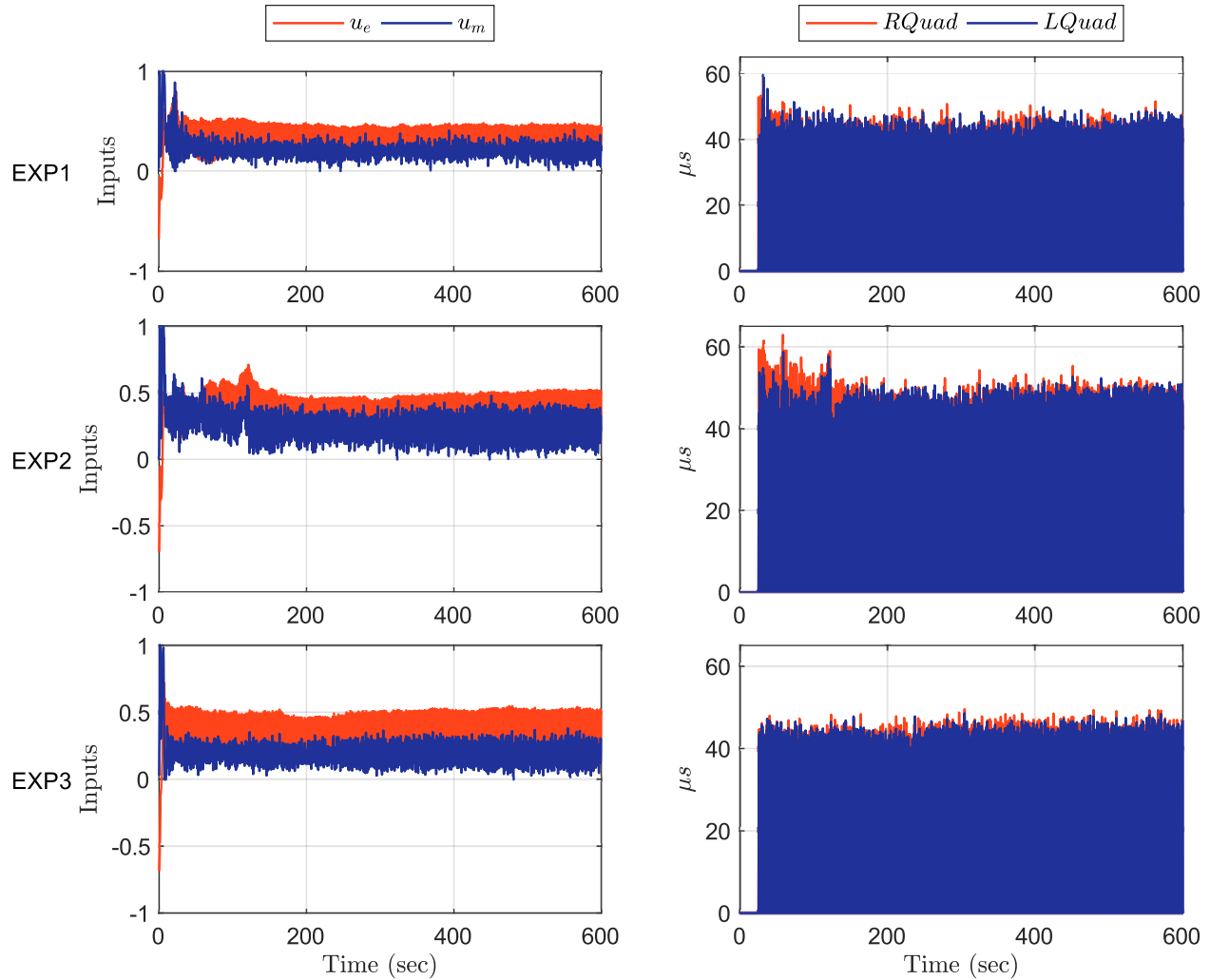


Figure 3.7: Control inputs across all experiments of subject **S4**. The plots on the left show the normalized control inputs, i.e., muscle and motor, computed for each experiment. The plots on the right show the applied FES input (pulse width) for the right and left quadriceps muscle groups. The FES input was applied 25 seconds after the beginning of the experiments to avoid delivering high stimulation intensities in the transient phase.

empty stack or with previously learned estimates from another cycling trial).

3.5.2 Desired cadence trajectories & parameter estimation performance

Two sets of desired trajectories were implemented in EXP1 and EXP2 to examine differences in parameter estimation performance. Figure 3.6 depicts the evolution of the minimum eigenvalue of the history stack between the cycling trials EXP1 and EXP2. The minimum eigenvalue in the

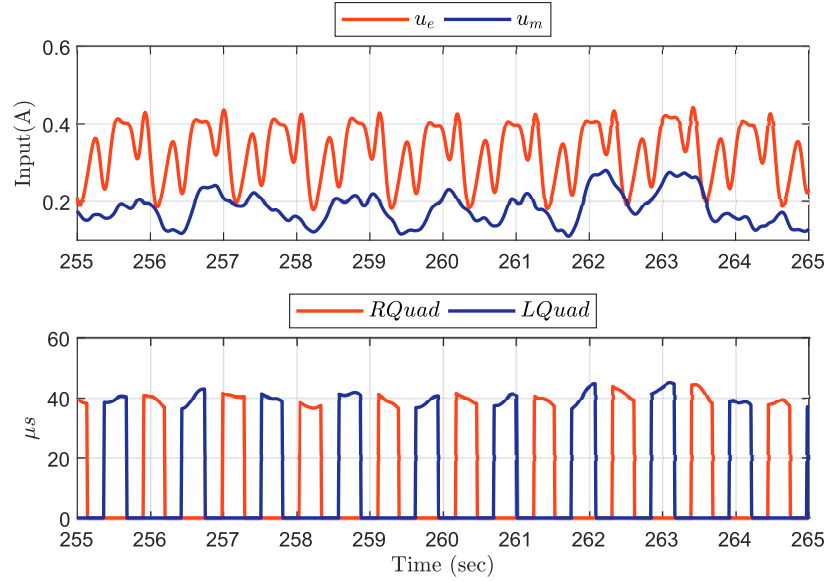


Figure 3.8: Control inputs of subject S4 across 10 crank cycles following 4 minutes of pedaling during the **EXP1**. Normalized muscle and motor control inputs are depicted in the top plot. FES delivered to the right and left quadriceps are depicted in the bottom plot.

trials EXP2 increases at a faster rate compared to the trials EXP1. This quantifiable condition is associated with faster convergence of the parameter estimates $\hat{\Theta}(t)$ and smoother cadence tracking performance since the FE condition is satisfied faster (and thus the history stack is not updated anymore). For comparative purposes, the FE condition $\underline{\lambda}$ was predetermined ahead of time before conducting the three cycling experiments for all participants. As illustrated in Figure 3.6, the predetermined FE condition is satisfied in the trials corresponding to EXP2 on average for all able-bodied participants at 110.69 ± 74.18 seconds, while this FE condition was not satisfied in trials corresponding to EXP1. Although the trials in EXP1 are said to not satisfy the predetermined FE condition, the history stack collected sufficiently rich data to yield a positive definite Σ_y throughout the duration of the cycling trial (see in Figure 3.6 that the minimum eigenvalue for all experiments is greater than zero no later than 33 seconds after the beginning of the trial for all participants). The results obtained from the cycling trials highlight the potential differences in performance due to the implementation of the sets of cadence trajectories. Different from classical adaptive control designs that require persistently exciting trajectories during the whole experiment to guarantee convergence of the estimates [30], in these cycling experiments,

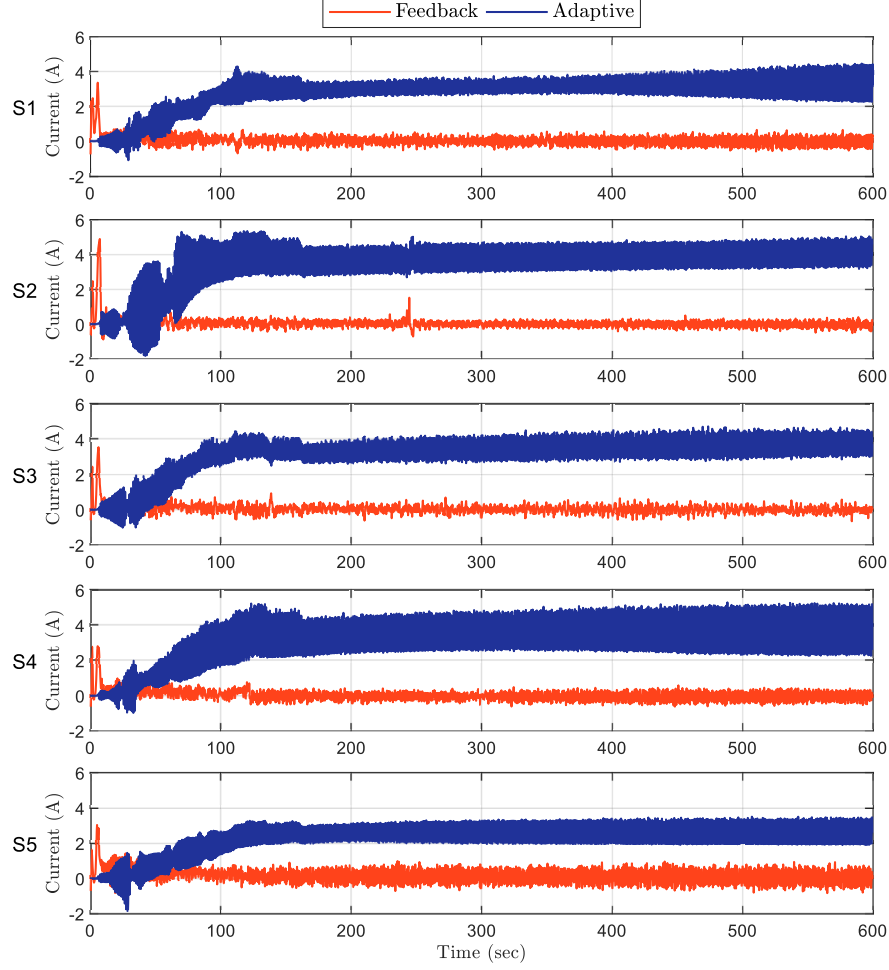


Figure 3.9: The control contributions in the controller in (3.11) are illustrated for cycling trials corresponding to **EXP2**. The red signal shows the robust state feedback term $(k_e r + e)$ while the blue signal shows the adaptive term contribution $Y_\sigma \hat{\Theta}$.

it is shown that introducing staircase trajectories during a finite time in the transient can aid in satisfying the quantifiable FE condition and achieving convergence of the estimates.

3.5.3 Control Contribution

The cadence motor controller u_e designed in (3.11) has three terms on the right-hand side, which can be segregated into robust state-feedback terms $(k_e r + e)$ and the adaptive feedforward term $(Y_\sigma \hat{\Theta})$. Figure 3.9 illustrates the time-varying contributions of the robust terms (red) and adaptive term (blue) during the cycling trials EXP2 for participants S1-S5 as representative examples.

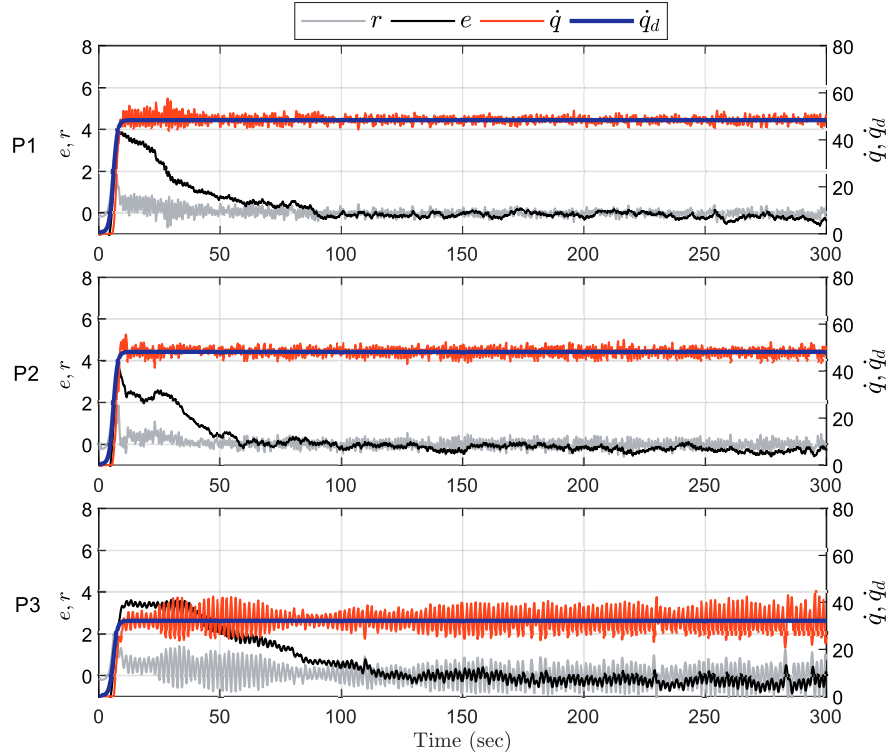


Figure 3.10: Kinematic tracking performance for participants with NCs undergoing **EXP1**. Cadence tracking (RPM), position error $e(t)$ (rad) and filtered error $r(t)$ are presented. Each row corresponds to one subject (P1-P3).

During the transient phase of the trials, the feedback terms have a higher contribution compared to the adaptive term. However, after an average across all able-bodied participants (S1-S8) of 49.68 ± 10.89 seconds from the start of the cycling trial, the contribution of the adaptive term increases surpassing the contribution of the robust feedback terms. As depicted in Figure 3.9, this observation on the difference between the feedforward and robust control contributions is consistent among all able-bodied participants (S1-S8) in the cycling trials EXP2. The same behavior was observed in EXP1 and EXP3, where the adaptive term overtakes the robust term contribution after 50.64 ± 24.55 , and 7.13 ± 1.42 seconds, respectively. Note that in EXP3, the adaptive term takes over significantly faster than the other two trials since the controller leverages data learned in the previous trial (i.e., in EXP2). The cycling experiments demonstrate the advantage of integrating the adaptive term in the cadence controller, which exploits the instantaneous and collected input-output data to generate the adaptive estimates and improve tracking performance.

In this way, the cadence controller relies less on high-gain feedback (and avoids the need for high-frequency control, e.g., sliding-mode control) and is less susceptible to changes in the selection of control feedback gains. For example, the same control gains and parameters were used for the three cycling experiments across all participants, able-bodied subjects (S1-S8) and participants with NCs (P1-P3) (i.e., for a total of 32 cycling trials). Thus, restrictive gain conditions are not developed in this work to compensate for the uncertainty in the cycle-rider dynamics. Hence, manual gain and parameter tuning was not needed for each participant, which is an important contribution given the inherent participant variability.

3.5.4 Participants with Neurological Conditions

The results presented in Table 3.3 with the three participants with NCs successfully demonstrate the control design's ability to achieve stable cadence tracking across a diverse range of individuals. Participants P1 and P2 achieved satisfactory results across all three trials, where the same trend observed in able-bodied participants was evident: stable tracking for all experiments, improved RMS cadence tracking error at steady-state compared to the RMS error for the full experiment, and faster position error convergence in EXP3 when compared to EXP1 and EXP2. For Participant P3, the protocol was modified to account for an inability to handle fast pedaling speeds. Thus, trial EXP2 was removed, and EXP1 and EXP3 were conducted at a lower speed (35 RPM) for P3. The results with P3 demonstrate that the controller can manage lower speeds. Smooth cadence tracking at low speeds can be challenging as depicted in the bottom plot of Figure 3.10, where the cadence tracking has more variability. Nonetheless, the system remains stable, the errors converge, and participant P3 successfully completed the trial.

3.6 Conclusion

A switching ICL controller was developed to track a desired cadence for a motorized FES-cycling system. The adaptive cadence controller was designed to improve tracking and generate estimates of the uncertain parameters in the cycle-rider dynamics and uncertain constant muscle control effectiveness in real time. Due to muscle switching needed to engage muscles in the left and right legs during FES-cycling, the adaptive controller exploits a switching update law where the muscle torque control input is exploited as a feedforward control term into the electric motor controller. Rather than canceling the muscle input as an exogenous input, the adaptive control approach embeds the muscle input into the regressor and facilitates estimating the muscle's uncertain effectiveness. A Lyapunov stability analysis for switching systems was developed leveraging a common Lyapunov function to demonstrate exponential kinematic tracking and parameter estimation convergence after a FE condition is satisfied. Particularly, a recent result for non-autonomous switched systems was exploited since a negative semi-definite Lyapunov derivative was obtained during the initial learning phase (i.e., when the FE condition is not yet satisfied) [41].

To demonstrate the feasibility of the control design, three ten-minute cycling experiments were implemented in eight able-bodied individuals resulting in 24 total cycling trials. Moreover, three participants with NCs tested the system during three five-minute trials. The cycling experiments were conducted to examine the control performance under different cadence trajectories and learning conditions. The first cycling experiment (EXP1) illustrates the system's performance by implementing a constant target cadence and initializing the history stack empty and the adaptive estimates to zero (i.e., no previous learning or knowledge of the system is exploited). The second experiment (EXP2) illustrates the system's performance implementing a staircase-like cadence trajectory (i.e., changing the target cadence during the transient until reaching a steady-state constant cadence). EXP2 facilitated the satisfaction of the predetermined FE condition. The third experiment (EXP3) tracked a constant cadence trajectory exploiting the learned parameters

computed at the end of the cycling trial EXP2. Satisfactory cadence tracking performance was obtained by initializing the adaptive update law with the learned parameters from EXP2; thus, illustrating the ability of the controller to learn useful estimates for tracking during a separate cycling trial. Results from all participants showed that the adaptive controller satisfied the pre-determined FE condition in EXP2 compared to EXP1, where the predefined FE condition is not satisfied; yet, the minimum eigenvalue remained positive during the trials as depicted in the Figure 3.6. By leveraging previously learned data in the cycling experiments from EXP2 into EXP3, across all participants, it was observed that the position error $e(t)$ presented a significantly faster convergence in the cycling trial EXP3 compared to EXP1 and EXP2.

Chapter 4

Integral Torque Tracking with Anti-Windup Compensation and Adaptive Cadence Tracking for Powered FES-Cycling

In this chapter and in the work in [51], a torque and cadence tracking control design (power tracking control) is developed for a motorized FES-cycling system. The quadriceps muscle groups track a desired active torque, while the electric motor regulates the speed to a constant cadence. The main contribution presented in this chapter is the development of a muscle torque tracking controller that incorporates an anti-windup term in an integral-like error signal to compensate for muscle saturation and prevent commanding high FES inputs due to error build-up. Since the muscle active torque acts as an exogenous input in the cadence tracking loop, an adaptive-based cadence controller is developed for the electric motor. Rather than canceling the muscle input in the cadence control loop, a switched concurrent learning controller is developed to embed the torque produced by muscles into the regressor (which is feasible since the muscle torque con-

troller is implementable) and estimate uncertain constant parameters of the nonlinear cycle-rider dynamics to achieve kinematic tracking. A Lyapunov-based stability analysis is developed for the torque and cadence control loops. Globally uniformly ultimately bounded (GUUB) tracking is obtained for the torque tracking objective. The stability analysis of the cadence tracking loop is divided into two phases. During the initial phase, the adaptive cadence controller records input-output data, and bounded tracking and parameter estimates are obtained leveraging a theorem for switching systems [41]. In the final phase, a final excitation (FE) condition is satisfied to ensure exponential cadence tracking and parameter estimation convergence. The tracking controllers were implemented during cycling experiments in one able-bodied individual to demonstrate the feasibility of the developed control strategy.

4.1 Active Torque Tracking Development

Two control objectives are developed to design an FES muscle controller u_m to track a desired active torque and an electric motor controller u_e to track a desired cadence. The strategy is to segregate the control of muscles and the electric motor by (i) prioritizing the design of an integral muscle torque control input with an anti-windup term and (ii) integrating the adaptive cadence controller developed in Chapter 3 for the motor to regulate the cycle's speed and embed the muscle-evoked torque into the regressor, which eliminates the need for the motor controller to reject the muscle torque input. The FES control design developed in this chapter is fundamentally different from the one presented in Chapter 3 since the objective here is to achieve torque tracking with the muscle input. Unlike the control designed in (3.10) that tracks cadence, the current FES controller will track a desired torque, while the adaptive cadence motor controller (3.11) embeds the muscle input generated in the torque loop defined below.

The torque $\tau_m : \mathcal{S} \times \mathbb{R}_{\geq t_0} \rightarrow \mathbb{R}_{>0}$ produced by the muscles can be defined as

$$\tau_m(t, \sigma) \triangleq B_m(\sigma) \text{sat}_{\beta_m}(u_m(t)), \quad (4.1)$$

where $u_m(t)$ is a subsequently-designed control input and the saturation function is defined as (3.12).

To quantify the torque tracking objective, the torque tracking error $e_{aw} : \mathbb{R}_{\geq t_0} \rightarrow \mathbb{R}$ with anti-windup compensation is defined as

$$e_{aw}(t) \triangleq \int_{t_0}^t [(\tau_d - \hat{\tau}_m) - k_{aw}(u_m - \text{sat}_{\beta_m}(u_m))] d\gamma, \quad (4.2)$$

where $\tau_d : \mathbb{R}_{\geq t_0} \rightarrow \mathbb{R}$ is the desired active torque trajectory bounded as $|\tau_d| \leq \bar{\tau}_d$, where $\bar{\tau}_d \in \mathbb{R}_{>0}$ is a known constant, $\hat{\tau}_m : \mathbb{R}_{\geq t_0} \rightarrow \mathbb{R}_{>0}$ is the estimation of the active torque produced by the muscles, and $k_{aw} \in \mathbb{R}_{>0}$ is a selectable constant. The error signal in (4.2) reduces only to the difference between the desired and actual torque when the control input is not saturated (i.e., $u_m = \text{sat}_{\beta_m}(u_m)$). When the controller reaches saturation, the saturation limit is exploited to generate a mismatch with the computed control input that helps to mitigate the wind-up effect in e_{aw} . The active torque estimation is obtained as in [52], [53], where a baseline passive torque $\tau_{passive} \in \mathbb{R}$ is recorded from a pre-trial and subtracted from the actual torque measurement τ as

$$\hat{\tau}_m \triangleq \tau - \tau_{passive}. \quad (4.3)$$

The active torque is defined as

$$\tau_m = \hat{\tau}_m + \epsilon(t), \quad (4.4)$$

where $\epsilon : \mathbb{R}_{\geq t_0} \rightarrow \mathbb{R}$ denotes the estimation error and satisfies $\epsilon \leq \bar{\epsilon}$, where $\bar{\epsilon} \in \mathbb{R}_{\geq 0}$ is a known constant. Taking the time derivative of (4.2), assuming zero initial conditions (see Remark 3), and

substituting (4.1) and (4.4) yields the torque open-loop error system

$$\dot{e}_{aw} = \tau_d - B_m \text{sat}_{\beta_m}(u_m) + \epsilon - k_{aw}(u_m - \text{sat}_{\beta_m}(u_m)). \quad (4.5)$$

Given the open-loop dynamics in (4.5), the muscle control input $u_m : \mathbb{R}_{\geq t_0} \rightarrow \mathbb{R}$ is designed as

$$u_m(t) \triangleq k_m e_{aw} + k_s \text{sgn}(e_{aw}), \quad (4.6)$$

where $k_m, k_s \in \mathbb{R}_{>0}$ are selectable control gains.

Remark 3. To implement the controller in (4.6), the error e_{aw} has to be evaluated first. Thus, the online integration is computed with the initial condition defined as $u_m(t_0) = 0$ for the first iteration.

Two cases are developed and subsequently analyzed corresponding to when muscles are not saturated (Case 1) and when muscles have reached the saturation limit (Case 2).

Case 1 when $|u_m| \leq \beta_m \implies \text{sat}_{\beta_m}(u_m) = u_m$, the muscle is not saturated, the open-loop error system in (4.5) is simplified to

$$\dot{e}_{aw} = \tau_d - B_m u_m + \epsilon. \quad (4.7)$$

Substituting the control input (4.6) into the previous expression yields the closed-loop error system defined as

$$\dot{e}_{aw} = \tau_d - B_m k_m e_{aw} - B_m k_s \text{sgn}(e_{aw}) + \epsilon. \quad (4.8)$$

Case 2 when $|u_m| > \beta_m \implies \text{sat}_{\beta_m}(u_m) = \beta_m \text{sgn}(u_m)$, the muscle is saturated. Leveraging (3.12), the open-loop error system in (4.5) can be rewritten as

$$\dot{e}_{aw} = \tau_d - k_{aw}u_m - (B_m - k_{aw})\beta_m \text{sgn}(e_{aw}) + \epsilon. \quad (4.9)$$

After substituting the control input (4.6) into the previous expression, and leveraging the fact that $\text{sgn}(u_m) = \text{sgn}(e_{aw})$, the closed-loop error system is obtained as

$$\dot{e}_{aw} = \tau_d - k_{aw}k_me_{aw} - (k_{aw}k_s + (B_m - k_{aw})\beta_m)\text{sgn}(e_{aw}) + \epsilon. \quad (4.10)$$

4.2 Stability Analysis

The stability of the robust muscle torque tracking controller can be examined through Theorem 1, which shows the closed-loop torque error system is GUUB. The stability of the closed-loop cadence error system is developed in Chapter 3 (Section 3.3).

Theorem 3. *The torque controller in (4.6) ensures GUUB tracking in the sense that*

$$|e_{aw}(t)| \leq \sqrt{\frac{\zeta_2}{\zeta_1} e_{aw}^2(t_0) e^{-\varphi_1(t-t_0)} + \frac{\varphi_2}{\zeta_1 \varphi_1} (1 - e^{-\varphi_1(t-t_0)})}, \quad (4.11)$$

provided the following sufficient gain conditions are satisfied

$$k_s \geq \frac{\bar{\tau}_d}{k_{aw}}, k_{aw} \leq \underline{B} \quad (4.12)$$

Proof. Let the Lyapunov function candidate $V_\tau : \mathbb{R} \times \mathbb{R}_{\geq t_0} \rightarrow \mathbb{R}_{\geq 0}$ be defined as

$$V_\tau(e_{aw}, t) = \frac{1}{2} e_{aw}^2(t), \quad (4.13)$$

that satisfies the following inequalities

$$\zeta_1 e_{aw}^2 \leq V_\tau \leq \zeta_2 e_{aw}^2, \quad (4.14)$$

where $\zeta_1, \zeta_2 \in \mathbb{R}_{>0}$ are constants. The control input in (4.6) includes the signum function. Hence, the system is treated as the differential inclusion $\dot{e}_{aw} \stackrel{a.e.}{\in} K[f](e_{aw})$ as in [54] where $K[\cdot]$ is defined as in [55] and f denotes the closed-loop error dynamics. Thus, the time derivative of (4.13) exists almost everywhere (a.e.), i.e., for almost all t and can be expressed for each case as follows¹

Case 1 Substituting the closed-loop dynamics in (4.8), the time derivative of (4.13) can be expressed as

$$\dot{V}_\tau \subseteq e_{aw}(\tau_d - K[B_m]k_m e_{aw} - K[B_m]k_s \text{SGN}(e_{aw}) + \epsilon), \quad (4.15)$$

where $K[B_m] \subset [\underline{B}, \overline{B}]$. Thus, (4.15) can be upper bounded leveraging Property 4 as

$$\dot{V}_\tau \stackrel{a.e.}{\leq} -\underline{B}k_m e_{aw}^2 + |e_{aw}|(\overline{\tau}_d - \underline{B}k_s) + |e_{aw}|\overline{\epsilon}. \quad (4.16)$$

Thus, the following gain condition is defined

$$k_s \geq \frac{\overline{\tau}_d}{\underline{B}}. \quad (4.17)$$

Case 2 Substituting the closed-loop dynamics in (4.10), the time derivative of (4.13) can be expressed as

$$\dot{V}_\tau \subseteq e_{aw}(\tau_d - k_{aw}k_m e_{aw} + \epsilon - (k_{aw}k_s + (K[B_m] - k_{aw})\beta_m)\text{SGN}(e_{aw})). \quad (4.18)$$

¹ $K[\text{sgn}(e_{aw})] = \text{SGN}(e_{aw})$ such that $\text{SGN}(e_{aw}) = \{1\}$ if $e_{aw} > 0$; $[-1, 1]$ if $e_{aw} = 0$; and $\{-1\}$ if $e_{aw} < 0$, as defined in [50].

Using similar arguments as in (4.16), the previous expression can be upper bounded as follows

$$\dot{V}_\tau \stackrel{a.e.}{\leq} -k_{aw}k_me_{aw}^2 + |e_{aw}|\bar{\epsilon} + |e_{aw}|(\bar{\tau}_d + (k_{aw} - \underline{B})\beta_m - k_{aw}k_s). \quad (4.19)$$

Provided the gain conditions in (4.12) are satisfied, the inequalities in (4.16) and (4.19) can be upper bounded as

$$\dot{V}_\tau \stackrel{a.e.}{\leq} -k_{aw}k_pe_{aw}^2 + |e_{aw}|\bar{\epsilon} - k_{aw}k_de_{aw}^2, \quad (4.20)$$

where $k_m \triangleq k_p + k_d$.

Remark 4. The sufficient gain conditions in (4.12) are selected to facilitate and unify the analysis of both the non-saturated and saturated cases. Note that when $k_{aw} = \underline{B}$ in (4.12) yields $k_s \geq \frac{\bar{\tau}_d}{\underline{B}}$, which is the gain condition in (4.17) defined for case 1.

Substituting the upper bound from (4.14) into (4.20), and leveraging a nonlinear damping tool as in [56, ch.2] to simplify the last to terms in (4.20), the inequality in (4.20) can be further upper bounded as

$$\dot{V}_\tau \stackrel{a.e.}{\leq} -\varphi_1 V_\tau + \varphi_2, \quad (4.21)$$

where $\varphi_1 \triangleq \frac{k_{aw}k_p}{\zeta_2}$ and $\varphi_2 \triangleq \frac{\bar{\epsilon}^2}{k_{aw}k_d}$. Then, solving the differential inequality in (4.21) and substituting the bounds in (4.14) yields the result in (4.11). Since $V_\tau \in \mathcal{L}_\infty$, then $e_{aw} \in \mathcal{L}_\infty$ which implies that $u_m \in \mathcal{L}_\infty$ in (4.6). ■

4.3 Experimental Results

The muscle and motor controllers designed in (4.6) and the adaptive controller (3.11) developed in Chapter 3, were implemented during two 5-minute cycling trials in one able-bodied individual. Written informed consent was obtained prior to the experiments per the IRB approval at Syracuse University. The motorized FES-cycling testbed is described in Chapter 3 (Section 3.4). The first

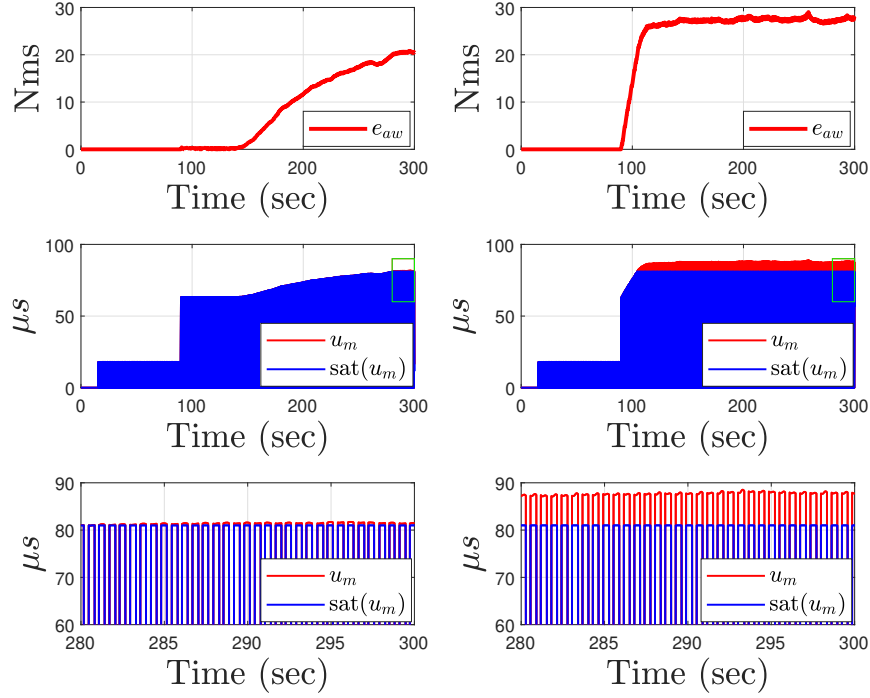


Figure 4.1: Torque tracking for both five-minute cycling experiments: trial one (2 Nm) on the left column and trial two (3 Nm) on the right column. The top plots show the integral torque error $e_{aw}(t)$. The plots in the middle show the muscle control input (pulse width). The bottom plots show a zoom-in version of the muscle input during the saturated regions with saturation limit $\beta_m = 80 \mu s$.

trial was implemented with a desired muscle torque amplitude of 2 Nm whereas the second trial was implemented to track a torque amplitude of 3 Nm. The cycling trials illustrate representative examples in which the rate at which muscle saturate vary depending on the torque demand (e.g., trial 2 saturates faster than trial 1 since the desired torque is higher). The control gains were kept constant for both trials and are selected as $k_m = 0.01, k_s = 0.7, k_{aw} = 0.4, k_e = 1.5, \alpha = 0.15, \Gamma = 0.0001 * \text{eye}(15), N = 30, \delta t = 0.03s, k_{cl} = 1.2$. For the first 15 seconds, only the cadence tracking loop is active to achieve a steady speed. After this initial phase, a warm-up phase is activated for the muscle input with a low constant stimulation. Then, the torque tracking loop is activated 90 seconds after the start of the trials. The torque tracking results of the two cycling trials with different desired torques are illustrated in Figure 4.1. The first trial is shown

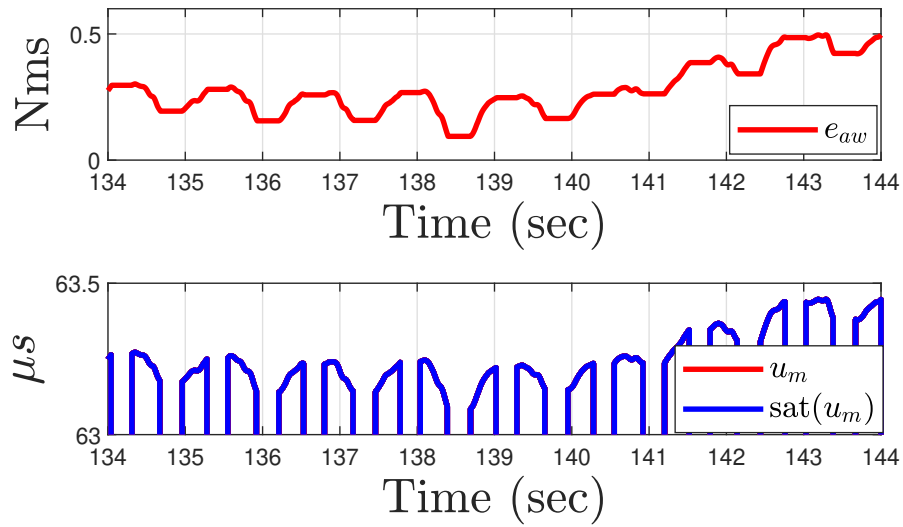


Figure 4.2: Torque error (top plot) and FES input (bottom plot) for trial one (2 Nm) when the system is not saturated (note that $u_m = \text{sat}_{\beta_m}(u_m)$).

on the left and the second trial is shown on the right. It can be observed that both torque error signals (top plots) remain bounded even when saturation occurs. The plots in the middle show the input u_m and the saturated input $\text{sat}_{\beta_m}(u_m)$. The bottom plots show a zoom-in region where the input reaches the saturation limit. It is illustrated that during the first trial muscles saturate later in the experiment since the desired torque is lower than in the second trial where the system saturates earlier (at 104 seconds). Regardless, the anti-windup compensation maintains the torque tracking error bounded in both cycling trials. The torque error and muscle input of the first trial are shown in Figure 4.2 during a 10-second window to illustrate the performance without muscle saturation. Kinematic tracking results corresponding to the second cycling trial are illustrated in Figure 4.3 for the 5-minute experiment. In Figure 4.3, it can be observed that the cadence error \dot{e} (left plot) experiences a transient that is reduced about 30 seconds into the experiment (as also illustrated in the right plot). Then, after 100 seconds, following the activation of the muscle torque controller, the cadence tracking error increases but ultimately decreases around 200 seconds since the adaptive cadence controller accounts for the exogenous muscle input. The adaptive estimates of the uncertain parameters in the cycle-rider system are depicted in Fig 4.4. Note that the adaptive estimates converge to constant values after 150 seconds.

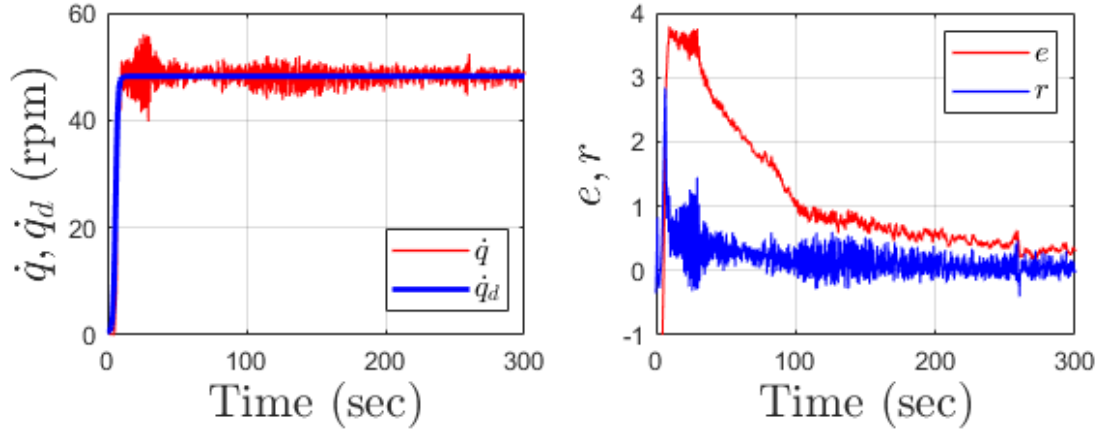


Figure 4.3: Kinematic tracking of the second trial. Cadence tracking is shown on the left side and the position error $e(t)$ and filtered error $r(t)$ are shown on the right.

4.4 Conclusion

In this chapter, a power tracking control design for muscles and an electric motor was developed and implemented in cycling experiments to demonstrate its feasibility. An active torque tracking controller with anti-windup compensation was designed to cope with muscle input saturation. The muscle and motor control designs are motivated to exploit input-output data from the active torque produced by the muscles to improve cadence tracking by using the muscle inputs as feedforward terms into the motor cadence controller as developed in Chapter 3. The adaptive cadence controller achieves exponential tracking and parameter estimation of the cycle-rider uncertain parameters after a finite excitation condition is satisfied (i.e., after collecting sufficiently rich input-output data). The muscle controller with the anti-windup term achieves GUUB torque tracking. Two cycling trials with one able-bodied participant were performed. Results demonstrated the efficacy of the anti-windup compensation to avoid error build-up when the input is saturated.

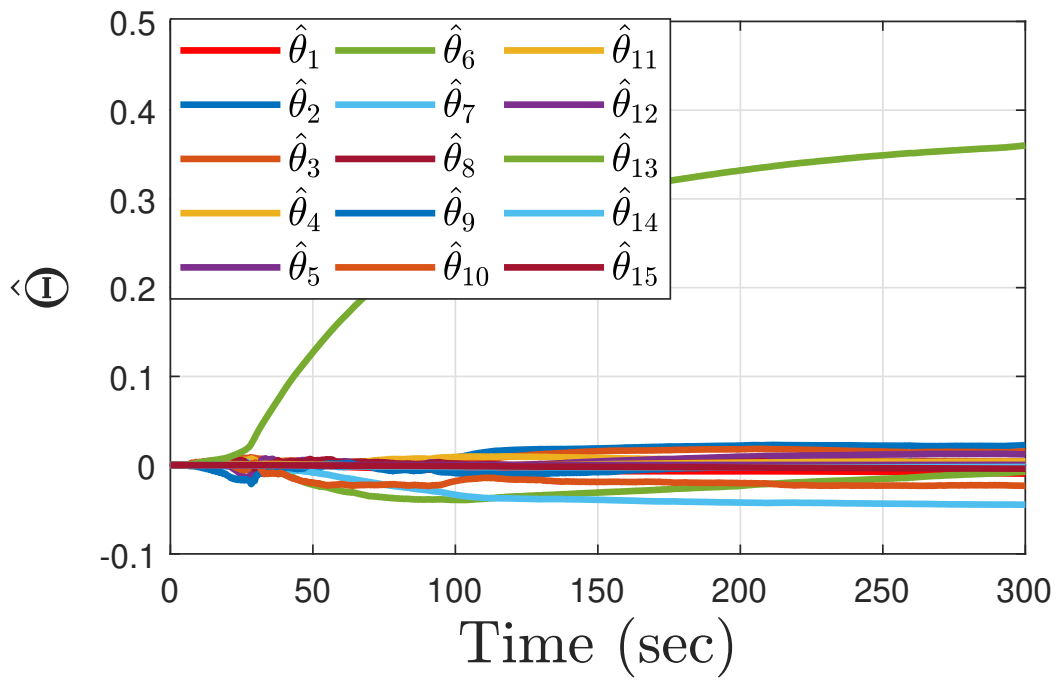


Figure 4.4: Adaptive estimates $\hat{\Theta}(t)$ of the uncertain constant parameters computed during the second cycling trial.

Chapter 5

Switched Concurrent Learning Adaptive Control for Treadmill Walking using a Lower-limb Hybrid Exoskeleton

In this chapter and based on [57], [58], a concurrent learning adaptive kinematic controller is designed, analyzed, and implemented on the 4-DoF lower limb exoskeleton introduced in Chapter 2 to provide hip and knee joint assistance during the stance and swing phases of walking. The phase-based walking model is used to implement the concurrent learning controller to estimate the leg uncertain parameters by switching between the right and left leg stance models. The stability analysis is rigorously developed using multiple Lyapunov functions to account for the switching of the gait models yielding a dwell time condition to ensure convergence across gait phase transitions. Experimental results in two able-bodied individuals are presented to illustrate the performance of the adaptive kinematic controller for a constant treadmill walking speed. An experimental comparison between the concurrent learning controller and a classical gradient-based adaptive controller is also provided.

5.1 Control Development

This section develops the control design for the human-exoskeleton system to track desired kinematic joint angle trajectories throughout the gait cycle. The control design is developed using a switched adaptive-based concurrent learning approach that estimates unknown constant parameters in the dynamics in (2.5) using instantaneous and stored input-output data. To quantify the tracking performance, the measurable joint angular position error $e : \mathbb{R}_{\geq t_0} \rightarrow \mathbb{R}^4$ and the auxiliary filtered tracking error $r : \mathbb{R}_{\geq t_0} \rightarrow \mathbb{R}^4$ are defined as

$$e(t) = q_d(t) - q(t), \quad (5.1)$$

$$r(t) = \dot{e}(t) + \alpha e(t), \quad (5.2)$$

where $\alpha \in \mathbb{R}_{>0}$ is a selectable constant control gain, and $q_d : \mathbb{R}_{\geq t_0} \rightarrow \mathbb{R}^4$ are continuously differentiable desired kinematic trajectories with bounded derivatives such that $\|\dot{q}_d\| \leq \bar{v}$, $\|\ddot{q}_d\| \leq \bar{a}$, where $\bar{v}, \bar{a} \in \mathbb{R}_{>0}$ are known upper bounds. Taking the time derivative of (5.2), pre-multiplying by M_σ , substituting the dynamics in (2.5), using (5.1), (5.2) and Property 8, and performing algebraic manipulation yields the open-loop error dynamics as¹

$$M_\sigma \dot{r} = Y_\sigma \Theta - B_\rho u_\sigma - C_\sigma r, \quad (5.3)$$

where $Y_\sigma : \mathcal{Q}^4 \times \mathbb{R}^4 \times \mathbb{R}_{\geq t_0} \rightarrow \mathbb{R}^{4 \times 19}$, $\forall \sigma \in \mathcal{S}$ is a switched regressor matrix of known functions and $\Theta \in \mathbb{R}^{19}$ is a vector of unknown constant parameters, described in Section 5.2, defined as

$$Y_\sigma \Theta \triangleq M_\sigma(\ddot{q}_d + \alpha \dot{e}) + C_\sigma(\dot{q}_d + \alpha e) + G_\sigma + P_\sigma \dot{q}. \quad (5.4)$$

¹Functional dependencies are omitted henceforth unless required for clarification.

Given the open-loop error system in (5.3), the control input is designed as

$$u_\sigma(t) = B_\rho^{-1} \left(k_\sigma r + e + Y_\sigma \hat{\Theta} \right), \forall \sigma \in \mathcal{S}, \quad (5.5)$$

where $k_\sigma \in \mathbb{R}_{>0}^{4 \times 4}$ is a selectable diagonal constant gain matrix and the parameter estimates are denoted as $\hat{\Theta} : \mathbb{R}_{\geq t_0} \rightarrow \mathbb{R}^{19}$. The parameter estimation error $\tilde{\Theta} : \mathbb{R}_{\geq t_0} \rightarrow \mathbb{R}^{19}$ is defined as

$$\tilde{\Theta}(t) = \Theta - \hat{\Theta}(t). \quad (5.6)$$

To estimate the unknown parameters, a switched ICL adaptive update law is designed as [32], [36]

$$\dot{\hat{\Theta}}_\sigma \triangleq \Gamma Y_\sigma^T r + k_{cl} \Gamma \sum_{p=1}^{\bar{p}} \mathcal{Y}_\sigma^T(t_p) \left(\mathcal{V}_\sigma(t_p) - \mathcal{Y}_\sigma(t_p) \hat{\Theta}(t) \right), \quad (5.7)$$

$\forall \sigma \in \mathcal{S}$. The update rule comprises two terms. The first term is the classical adaptive gradient descent that drives parameter estimation in the direction of reducing tracking error. The second term is an integral concurrent learning which uses the historical data stored in the stack to compute the input-output estimation error and drive the parameters toward reducing the estimation error. The second term guarantees convergence of the parameter estimates. The selectable positive $\Gamma \in \mathbb{R}^{19 \times 19}$ is a definite diagonal matrix, $k_{cl} \in \mathbb{R}_{>0}$ is a selectable gain, and a history stack of size $\bar{p} \in \mathbb{N}$ records input-output data for parameter estimation and convergence [31], [40]. The time at which the p -th data point is recorded in the stack is denoted by $t_p \in \mathbb{R}_{>0}$, and the auxiliary input $\mathcal{V}_\sigma : \mathbb{R}_{\geq t_0} \rightarrow \mathbb{R}^4$ and output $\mathcal{Y}_\sigma : \mathbb{R}_{\geq t_0} \rightarrow \mathbb{R}^{4 \times 19}$ functions are defined, respectively, as

$$\mathcal{V}_\sigma(t_p) = \int_{t_p - \delta t}^{t_p} B_\rho u_\sigma(\gamma) d\gamma, \quad (5.8)$$

$$\mathcal{Y}_\sigma(t_p) = \Phi_\sigma + \int_{t_p - \delta t}^{t_p} \Psi_\sigma(\gamma) d\gamma, \quad (5.9)$$

where $\delta t \in \mathbb{R}_{>0}$ denotes the integration time window in which input-output data is collected, and the auxiliary regressors $\Phi_\sigma, \Psi_\sigma : \mathcal{Q}^4 \times \mathbb{R}^4 \times \mathbb{R}_{\geq t_0} \rightarrow \mathbb{R}^{4 \times 19}$ are designed as

$$\Phi_\sigma \Theta = M_\sigma(q(t_p))\dot{q}(t_p) - M_\sigma(q(t_p - \delta t))\dot{q}(t_p - \delta t), \quad (5.10)$$

$$\Psi_\sigma \Theta = -\dot{M}_\sigma \dot{q} + C_\sigma \dot{q} + G_\sigma + P_\sigma \dot{q}. \quad (5.11)$$

Remark 5. The vector $\hat{\Theta}$ are estimates of the constant uncertain parameters Θ that are described in Section 5.2. The uncertain parameters in the dynamic model represent a combination of inertial terms, torques due to gravity, and friction coefficients, which are not influenced by switching effects. Alternatively, the adaptive update law in (5.7) is switching according to each walking phase ($\sigma = 1$ or $\sigma = 2$) and depends on the switching regressor Y_σ and the input-output data \mathcal{Y}_σ and \mathcal{V}_σ .

Integrating both sides of (2.5), applying integration by parts for the term $M_\sigma \ddot{q}$ and combining Equations (5.10) and (5.11), yields²

$$\Phi_\sigma \Theta + \int_{\delta t} \Psi_\sigma(\gamma) \Theta d\gamma = \int_{\delta t} B_\rho u_\sigma(\gamma) d\gamma, \quad (5.12)$$

$$\mathcal{Y}_\sigma \Theta = \mathcal{V}_\sigma. \quad (5.13)$$

Based on the input-output relationship in (5.13) and using (5.6), the concurrent learning update law in (5.7) can be re-written in analytical form as

$$\dot{\hat{\Theta}}_\sigma = \Gamma Y_\sigma^T r + k_{cl} \Gamma \left(\sum_{p=1}^{\bar{p}} \mathcal{Y}_\sigma^T(t_p) \mathcal{V}_\sigma(t_p) \right) \tilde{\Theta}(t). \quad (5.14)$$

As specified in Remark 2 in Chapter 3, a singular-value maximization algorithm is implemented for the history stack to improve the parameter estimation convergence.

²For simplicity, the notation of the limits of integration is expressed as δt to denote integration over the interval $[t - \delta t, t]$

After substituting (5.5) into (5.3) the closed-loop error system is obtained as

$$M_\sigma \dot{r} = -k_\sigma r + Y_\sigma \tilde{\Theta} - e - C_\sigma r. \quad (5.15)$$

Combining (5.2), (5.15), the time derivative of (5.6) and using (5.14) yields the following closed-loop dynamics

$$\begin{bmatrix} \dot{e} \\ M_\sigma \dot{r} \\ \dot{\tilde{\Theta}} \end{bmatrix} = \begin{bmatrix} r - \alpha e \\ -k_\sigma r + Y_\sigma \tilde{\Theta} - e - C_\sigma r \\ -\Gamma Y_\sigma^T r - k_{cl} \Gamma \left(\sum_{p=1}^{\bar{p}} \mathcal{Y}_\sigma^T(t_p) \mathcal{Y}_\sigma(t_p) \right) \tilde{\Theta} \end{bmatrix}. \quad (5.16)$$

5.2 Unknown Constant Parameters

The Euler-Lagrange dynamic model in (2.5) satisfies the linear-in-the-parameters (LIP) property [59]. This property allows the dynamic equation to be represented as a product of a regressor matrix $Y \in \mathbb{R}^{4 \times 19}$ and a vector of constant parameters $\Theta \in \mathbb{R}^{19}$. In this work, the legs are assumed to be symmetric (i.e., masses and lengths are considered the same for both legs). The

vector of constant parameters can be expressed as

$$\begin{aligned}
\theta_1 &= I_t + 2M_s L_s^2 + 2M_t L_s^2 + M_s L_t^2 + 2M_t L_t^2 + M_s l_s^2 + M_t l_t^2 - 2M_s L_s l_s - 2M_t L_t l_t, \\
\theta_2 &= I_s + 2L_s^2 M_s + 2L_s^2 M_t + M_s l_s^2 - 2L_s M_s l_s, \\
\theta_3 &= I_t + M_s L_t^2 + M_s l_s^2 + M_t l_t^2, \\
\theta_4 &= I_s + M_s l_s^2, \\
\theta_5 &= 2M_s L_s^2 + 2M_t L_s^2 + M_s l_s^2 - 2M_s L_s l_s, \\
\theta_6 &= M_s L_s L_t + 2M_t L_s L_t - M_t L_s l_t, \\
\theta_7 &= M_t L_s l_t + M_s L_s L_t, \\
\theta_8 &= M_s L_t^2 + M_t L_t l_t, \\
\theta_9 &= M_s L_s l_s, \\
\theta_{10} &= M_s L_t l_s, \\
\theta_{11} &= M_s l_s^2, \\
\theta_{12} &= g(2M_s L_s + 2M_t L_s - M_s l_s), \\
\theta_{13} &= g(M_s L_t + 2M_t L_t - M_t l_t), \\
\theta_{14} &= g(M_t l_t + M_s L_t), \\
\theta_{15} &= gM_s l_s, \\
\theta_{16} &= p_{RH}, \\
\theta_{17} &= p_{RK}, \\
\theta_{18} &= p_{LH}, \\
\theta_{19} &= p_{LK},
\end{aligned} \tag{5.17}$$

where M_s, M_t, I_s, I_t denote the mass and moment of inertia of the shank and thigh, respectively; l_s, l_t denote the location of the center of mass (CoM) of the shank and thigh, respectively, as illustrated in Figure 5.1. The viscous damping coefficients for each joint are denoted as $p_{RH}, p_{RK}, p_{LH}, p_{LK}$. The parameters are divided in three main groups. The first group contains the inertial parameters ($\theta_1 - \theta_{11}$) with units kgm^2 , the second group contains the torque parameters ($\theta_{12} - \theta_{15}$) with units Nm , and the third group contains the unit-less friction coefficients ($\theta_{16} - \theta_{19}$).

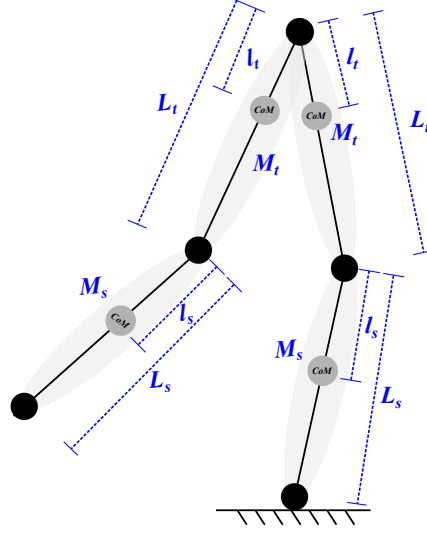


Figure 5.1: Schematic of the lower limbs depicting a subset of the uncertain constant parameters in (5.17) assuming symmetry between legs.

5.3 Stability Analysis

The stability analysis is segregated into two theorems. Theorem 4 shows that exponential tracking is achieved for each individual gait phase, i.e, *right leg stance* ($\sigma = 1$) and *right leg swing* ($\sigma = 2$) phases. As depicted in Figure 2.2, the *right leg stance phase* for the step $n \in \mathbb{N}$ starts at time $t_n^{\sigma=1} \in \mathbb{R}_{\geq t_0}$ with the right heel strike, and ends at time $t_n^{\sigma=2} \in \mathbb{R}_{\geq t_0}$ before the left heel strike at which the *right leg swing phase* starts. The next right heel strike initiates step $n + 1$ at time $t_{n+1}^{\sigma=1}$. Theorem 5 develops a multiple Lyapunov analysis to demonstrate stability of the overall system, i.e., the combination of both phases, *right leg stance* and *swing* phases of walking, accounting for transitions across multiple steps. Using a dwell time analysis, Theorem 5 ensures stability under a slow switching condition.

Leveraging Assumption 2, from Chapter 3, the history stack $\sum_{p=1}^{\bar{p}} \mathcal{Y}_p^T \mathcal{Y}_p$ can be ensured to be full rank by collecting sufficiently exciting data. The exciting data is recorded during a single

treadmill walking pretrial at the same constant speed as in the experiments until the excitation condition in Assumption 2 is satisfied since this condition is measurable. Assumption 2 is also verified online during the actual experiments by continually collecting data (i.e., using the singular value maximization algorithm in [40]) to ensure the minimum eigenvalue of $\sum_{p=1}^{\bar{p}} \mathcal{Y}_p^T \mathcal{Y}_p$ is always increasing until a user selectable threshold is reached [32] (e.g., the threshold in the experiments is selected larger than the threshold selected during the pretrial).

The following definition is exploited in the subsequent analysis.

Definition 1. *The time intervals of the right leg stance and right leg swing phase during the step n can be defined, respectively, as*

$$\mathcal{T}_n^{\sigma=1} \triangleq [t_n^{\sigma=1}, t_n^{\sigma=2}), \quad (5.18)$$

$$\mathcal{T}_n^{\sigma=2} \triangleq [t_n^{\sigma=2}, t_{n+1}^{\sigma=1}), \quad (5.19)$$

such that the time interval of the step n , including both gait phases, can be defined as

$$\mathcal{T}_n \triangleq \mathcal{T}_n^{\sigma=1} \cup \mathcal{T}_n^{\sigma=2} = [t_n^{\sigma=1}, t_{n+1}^{\sigma=1}). \quad (5.20)$$

Thus, the lengths of each time interval are defined as

$$L_n^{\sigma=1} \triangleq t_n^{\sigma=2} - t_n^{\sigma=1}, \quad (5.21)$$

$$L_n^{\sigma=2} \triangleq t_{n+1}^{\sigma=1} - t_n^{\sigma=2}. \quad (5.22)$$

Theorem 4. *Given the closed-loop error dynamics in (5.16), the control input in (5.5) and adaptive law in (5.7) achieve exponential kinematic tracking for each individual walking phase (i.e., $\sigma = 1$ and $\sigma = 2$), provided the system satisfies the finite excitation condition in Assumption 2 from*

Chapter 3, such that

$$V_\sigma(t_n^\sigma + \Delta t) \leq V_\sigma(t_n^\sigma) \exp\left(-\frac{\Lambda_\sigma}{\beta_2} \Delta t\right), \quad \forall \sigma \in \mathcal{S}, \quad (5.23)$$

where $\Lambda_\sigma \triangleq \min(\alpha, \|k_\sigma\|, k_{cl}\lambda)$, and $\Delta t \in \mathbb{R}_{>0}$ denotes an arbitrary time such that $t_n^\sigma + \Delta t \in \mathcal{T}_n^\sigma, \forall \sigma \in \mathcal{S}, \forall n \in \mathbb{N}$.

Proof. Let $V_\sigma : \mathbb{R}^{27} \times \mathbb{R}_{\geq t_0} \rightarrow \mathbb{R}, \forall \sigma \in \mathcal{S}$ be a family of nonnegative, continuously differentiable Lyapunov-like function candidates for each walking phase, defined as

$$V_\sigma(e, r, \tilde{\Theta}) = \frac{1}{2} e^T e + \frac{1}{2} r^T M_\sigma r + \frac{1}{2} \tilde{\Theta}^T \Gamma^{-1} \tilde{\Theta}. \quad (5.24)$$

The functions in (5.24) satisfy the following inequalities

$$\beta_1 \|z\|^2 \leq V_\sigma \leq \beta_2 \|z\|^2, \quad \forall \sigma \in \mathcal{S}, \quad (5.25)$$

where $z : \mathbb{R}_{\geq t_0} \rightarrow \mathbb{R}^{27}$ is the lumped state defined as³

$$z \triangleq [e^T, r^T, \tilde{\Theta}^T]^T, \quad (5.26)$$

and the constants $\beta_1, \beta_2 \in \mathbb{R}_{>0}$ are defined as

$$\begin{aligned} \beta_1 &\triangleq \min \left\{ \frac{1}{2}, \frac{\underline{m}}{2}, \frac{1}{2} \lambda_{\min}\{\Gamma^{-1}\} \right\}, \\ \beta_2 &\triangleq \max \left\{ \frac{1}{2}, \frac{\overline{m}}{2}, \frac{1}{2} \lambda_{\max}\{\Gamma^{-1}\} \right\}, \end{aligned}$$

where \underline{m} and \overline{m} are bounds from Property 5, and $\lambda_{\min}\{\cdot\}, \lambda_{\max}\{\cdot\}$ denote the minimum and maximum eigenvalues of (\cdot) , respectively. After substituting for (5.16), the time derivative of (5.24)

³The size of z is obtained as the combination of the vectors $e, r \in \mathbb{R}^4$ and the parameter estimate error vector $\tilde{\Theta} \in \mathbb{R}^{19}$.

can be expressed as

$$\dot{V}_\sigma = e^T(r - \alpha e) + r^T(-k_\sigma r + Y_\sigma \tilde{\Theta} - e) + r^T(\frac{1}{2}\dot{M}_\sigma - C_\sigma)r - \tilde{\Theta}^T \Gamma^{-1} \dot{\tilde{\Theta}}_\sigma. \quad (5.27)$$

By using Property 6, substituting (5.14), and canceling terms, (5.27) can be rewritten as

$$\dot{V}_\sigma = -\alpha e^T e - r^T k_\sigma r - k_{cl} \tilde{\Theta}^T \left(\sum_{p=1}^{\bar{p}} \mathcal{Y}_\sigma^T(t_p) \mathcal{Y}_\sigma(t_p) \right) \tilde{\Theta}(t). \quad (5.28)$$

Based on Assumption 2, the history stack is positive definite and (5.28) can be upper bounded as

$$\begin{aligned} \dot{V}_\sigma &\leq -\alpha \|e\|^2 - \|k_\sigma\| \|r\|^2 - k_{cl} \underline{\lambda} \|\tilde{\Theta}\|^2, \\ \dot{V}_\sigma &\leq -\Lambda_\sigma \|z\|^2, \quad \forall \sigma \in \mathcal{S}. \end{aligned} \quad (5.29)$$

Using the inequalities in (5.25) and (5.29), the exponential result in (5.23) can be obtained. Further, exponential tracking is guaranteed and the following upper bound can be obtained for (5.26) as

$$\|z(t_n^\sigma + \Delta t)\| \leq \sqrt{\frac{\beta_2}{\beta_1}} \|z(t_n^\sigma)\| \exp\left(-\frac{\Lambda_\sigma}{2\beta_2} \Delta t\right).$$

■

Theorem 4 shows exponential kinematic tracking for each individual gait phase. However, ensuring the stability of the individual walking phases does not guarantee the stability of the overall system with switching dynamics [14]. The subsequent analysis demonstrates exponential kinematic tracking under slow switching across multiple gait phase transitions.

Theorem 5. *Let V_σ , $\forall \sigma \in \mathcal{S}$ be the family of Lyapunov functions defined in (5.24) that ensure exponential kinematic tracking as in (5.23) for each walking phase during their corresponding time intervals \mathcal{T}_n^σ . Suppose that for the time interval $\mathcal{T}_n \cup \mathcal{T}_{n+1}$ defined in (5.20), the following*

inequality holds

$$V_\sigma(t_{n+1}^\sigma) - V_\sigma(t_n^\sigma) \leq -W_\sigma(z(t_n^\sigma)), \forall \sigma \in \mathcal{S}, \quad (5.30)$$

where $W_\sigma : \mathbb{R}^{18} \rightarrow \mathbb{R}$ is a positive definite function. Furthermore, the transition from step n to step $n + 1$ contains the following sequence of switching event times

$$\{t_n^{\sigma=1}, t_n^{\sigma=2}, t_{n+1}^{\sigma=1}, t_{n+1}^{\sigma=2}\}. \quad (5.31)$$

Hence, the overall switched system ensures global exponential kinematic tracking, provided the dwell time $\tau_d \in \mathbb{R}_{\geq 0}$ satisfies the following condition on the interval $\mathcal{T}_n \cup \mathcal{T}_{n+1}$

$$\tau_d > \frac{\beta_2}{\Lambda_{\sigma=1} + \Lambda_{\sigma=2}} \ln \left(\frac{\beta_2}{\beta_1} \right)^2. \quad (5.32)$$

Proof. Each gait phase lasts at least τ_d such that the following condition holds

$$L_n^\sigma \geq \tau_d, \forall \sigma \in \mathcal{S}, \forall n \in \mathbb{N}. \quad (5.33)$$

Using the bounds in (5.25), the following inequalities can be obtained

$$V_{\sigma=1}(t) \leq \frac{\beta_2}{\beta_1} V_{\sigma=2}(t), \quad (5.34)$$

$$V_{\sigma=2}(t) \leq \frac{\beta_2}{\beta_1} V_{\sigma=1}(t). \quad (5.35)$$

Using (5.33) with $L_n^{\sigma=2}$ and (5.22), $t_{n+1}^{\sigma=1} \geq t_n^{\sigma=2} + \tau_d$ is obtained to express (5.23) as

$$V_{\sigma=2}(t_{n+1}^{\sigma=1}) \leq V_{\sigma=2}(t_n^{\sigma=2}) \exp \left(-\frac{\Lambda_{\sigma=2}}{\beta_2} \tau_d \right). \quad (5.36)$$

Evaluating (5.34) at time $t_{n+1}^{\sigma=1}$ and substituting for (5.36) yields

$$V_{\sigma=1}(t_{n+1}^{\sigma=1}) \leq \frac{\beta_2}{\beta_1} V_{\sigma=2}(t_n^{\sigma=2}) \exp \left(-\frac{\Lambda_{\sigma=2}}{\beta_2} \tau_d \right). \quad (5.37)$$

Using (5.33) with $L_n^{\sigma=1}$ and (5.21), $t_n^{\sigma=2} \geq t_n^{\sigma=1} + \tau_d$ is obtained to express (5.23) as

$$V_{\sigma=1}(t_n^{\sigma=2}) \leq V_{\sigma=1}(t_n^{\sigma=1}) \exp \left(-\frac{\Lambda_{\sigma=1}}{\beta_2} \tau_d \right). \quad (5.38)$$

Combining (5.38) and (5.35) evaluated at time $t_n^{\sigma=2}$, and substituting into (5.37) yields the following upper bound for $V_{\sigma=1}$ during the *right leg stance* phase as

$$V_{\sigma=1}(t_{n+1}^{\sigma=1}) \leq \left(\frac{\beta_2}{\beta_1} \right)^2 V_{\sigma=1}(t_n^{\sigma=1}) \exp \left(-\frac{\Lambda_{\sigma=1} + \Lambda_{\sigma=2}}{\beta_2} \tau_d \right). \quad (5.39)$$

Similarly, for the *right leg swing* phase, combining (5.33), (5.23) using $L_{n+1}^{\sigma=1}$ and (5.22) as

$t_{n+1}^{\sigma=2} \geq t_{n+1}^{\sigma=1} + \tau_d$, and substituting the resulting expression into (5.35) evaluated at time $t_{n+1}^{\sigma=2}$ yields

$$V_{\sigma=2}(t_{n+1}^{\sigma=2}) \leq \frac{\beta_2}{\beta_1} V_{\sigma=1}(t_{n+1}^{\sigma=1}) \exp \left(-\frac{\Lambda_{\sigma=1}}{\beta_2} \tau_d \right). \quad (5.40)$$

Combining (5.40) with (5.37), an upper bound for $V_{\sigma=2}$ during *right leg swing* phase is obtained as

$$V_{\sigma=2}(t_{n+1}^{\sigma=2}) \leq \left(\frac{\beta_2}{\beta_1} \right)^2 V_{\sigma=2}(t_n^{\sigma=2}) \exp \left(-\frac{\Lambda_{\sigma=1} + \Lambda_{\sigma=2}}{\beta_2} \tau_d \right). \quad (5.41)$$

The inequalities in (5.39) and (5.41) show that $V_{\sigma=1}$, $V_{\sigma=2}$ (i.e., the Lyapunov functions for the *right leg stance* and *swing* phases, respectively) can be upper bounded by the same expression.

The subsequent analysis is developed to obtain the dwell time condition in (5.32). The analysis is developed for the *right leg stance* phase and the condition can be obtained similarly for the *swing* phase. Let the positive definite function in (5.30) be defined as $W_{\sigma=1} \triangleq \varphi \|z(t_n^{\sigma=1})\|^2$, where $\varphi \in \mathbb{R}_{>0}$. Substituting (5.39) and the lower bound in (5.25) into (5.30), and after some algebraic manipulation the following expression is obtained

$$\frac{\beta_2^2}{\beta_1} \exp \left(-\frac{\Lambda_{\sigma=1} + \Lambda_{\sigma=2}}{\beta_2} \tau_d \right) - \beta_1 \leq -\varphi. \quad (5.42)$$

The expression in (5.42) can be further upper bounded as

$$\exp\left(-\frac{\Lambda_{\sigma=1} + \Lambda_{\sigma=2}}{\beta_2}\tau_d\right) < \left(\frac{\beta_1}{\beta_2}\right)^2. \quad (5.43)$$

Solving the previous inequality for τ_d yields (5.32). Provided the condition in (5.32) and exploiting [14, Th. 3.1], then $\|e\|, \|r\|, \|\tilde{\Theta}\| \rightarrow 0$ as $t \rightarrow \infty$. Since $V_\sigma > 0$ and $\dot{V}_\sigma \leq 0$, $V_\sigma \in \mathcal{L}_\infty$, $\forall \sigma \in \mathcal{S}$, then $e, r, \tilde{\Theta} \in \mathcal{L}_\infty$, which implies that $\dot{e} \in \mathcal{L}_\infty$ from (5.2), and $\hat{\Theta} \in \mathcal{L}_\infty$ from (5.6), since Θ is a column vector of constant parameters. Since $e, r, \dot{e} \in \mathcal{L}_\infty$ then, $q, \dot{q} \in \mathcal{L}_\infty$, which implies that $Y_\sigma, \Phi_\sigma, \Psi_\sigma \in \mathcal{L}_\infty$ in (5.4), (5.10), and (5.11), and therefore $u_\sigma \in \mathcal{L}_\infty$ in (5.5). Consequently, $\mathcal{V}, \mathcal{Y} \in \mathcal{L}_\infty$ from (5.8) and (5.9), respectively, which implies that $\dot{\hat{\Theta}} \in \mathcal{L}_\infty$ in (5.7). Hence, $\ddot{q} \in \mathcal{L}_\infty$ from (2.5). ■

5.4 Experiments

This section presents the procedures developed to evaluate the performance of the adaptive control design. The experimental protocol and results of the walking trials are described.

5.4.1 Experimental Protocol

Two trials of treadmill walking experiments were conducted. The first trial (Exp1) is a baseline test in which the controller in (5.5) is implemented with a classical gradient-based adaptive update law setting $\dot{\hat{\Theta}}_\sigma \triangleq \Gamma Y_\sigma^T r$, where the concurrent learning term in (5.7) was removed. Exp1 is implemented to draw comparisons with the concurrent learning controller designed in this chapter. The second trial (Exp2) implemented the controller in (5.5) with the update law in (5.7) including the concurrent learning term. All experimental trials were performed for eight minutes on two different days for each subject, with the order of implementation of the trials randomized.

5.4.2 Participants

Two able-bodied subjects (S1 and S2: one male and one female, aged 22-31 years) participated in the walking protocol at Syracuse University. Both participants provided written informed consent as approved by the IRB at Syracuse University. The participants were instructed to avoid voluntarily contributing to the treadmill walking task. An orthotic boot was used to mechanically lock the ankle joint and reduce its influence on propulsion. The individuals did not receive verbal or visual feedback on their walking performance during the experiments. Prior to the experimental trials, both participants became acclimated to the device and were exposed to a sufficient amount of time to familiarize themselves with the electrical stimulation and feel comfortable wearing the device.

Table 5.1: Gain tuning and hyperparameter selection for all the experiments

Subject	Experiment	Adaptive Hyper-parameters					Feedback Gains		Input Gains	
		k_{cl}	Γ	\bar{p}	δt (s)	α	$k_{\sigma=1}$	$k_{\sigma=2}$	k_m	k_e
S1	Exp1	0	$0.02 * diag(19)$	0	0	3.5	[rk:0.7,lk: 2.3,rh: 0.8, lh:1]	[rk:2.3, lk:0.7, rh:1.2, lh:0.7]	Quad :3.2, Ham: 8	[rk:1.5,lk:1.5,rh:1,lh:1]
	Exp2	4	$0.13 * diag(19)$	50	0.03	2.3	[rk:0.7,lk: 2.3,rh: 0.8, lh:1]	[rk:2.3, lk:0.7, rh:1.2, lh:0.7]	Quad :3.2, Ham: 8	[rk:1.5,lk:1.5,rh:1,lh:1]
S2	Exp1	0	$0.0002 * diag(19)$	0	0	3.5	[rk:0.7, lk:2, rh:0.8, lh:1]	[rk:2, lk:0.7, rh:1.2, lh:0.7]	Quad :4.8, Ham: 12	[rk:1.5,lk:1.5,rh:1,lh:1]
	Exp2	4	$0.13 * diag(19)$	50	0.03	2.3	[rk:0.7, lk:2, rh:0.8, lh:1]	[rk:2, lk:0.7, rh:1.2, lh:0.7]	Quad :4.8, Ham: 12	[rk:1.5,lk:1.5,rh:1,lh:1]

rk : right knee, rh : right hip, lk : left knee, lh : left hip.

Table 5.2: Percentage of time spent on each walking phase during 114 strides (228 steps), for an average walking velocity of 0.48 steps/s

Subject	Experiment	%RS ($\sigma = 1$)	%LS ($\sigma = 2$)	%DS
S1	Exp 1	43.7%	42.8%	13.5%
	Exp 2	40.7%	46.8%	12.5%
S2	Exp 1	45.0%	50.5%	4.5%
	Exp 2	45.9%	46.9%	7.2%
Average		43.8%	46.7%	9.4%

5.4.3 Results

The results of Exp1 and Exp2 are presented in this section for both subjects (S1-S2). Table 5.1 reports the gain tuning and hyper-parameter selection for each experiment in three categories: hyper-parameter selection of the adaptive controller (concurrent learning gain k_{cl} , adaptive gain matrix Γ , size of the history stack \bar{p} , and integration window δt), feedback gains (α , k_{σ}), and tuning gains for individual actuators (k_m for muscles and k_e for motors) as described in (2.6) in Section 2.2. Table 5.2 reports the average time spent on each walking phase, including single right or left stance and double support, for all subjects in both experiments. The trials lasted eight minutes, during which a total of 114 strides (228 steps) were completed at an average walking speed of 0.48 steps/s.

Kinematic Tracking

The joint kinematic tracking performance in Exp1 and Exp2 for both participants is reported in Table 5.3, where the root-mean-square error (RMS) was calculated for e in (5.1) and r in (5.2)

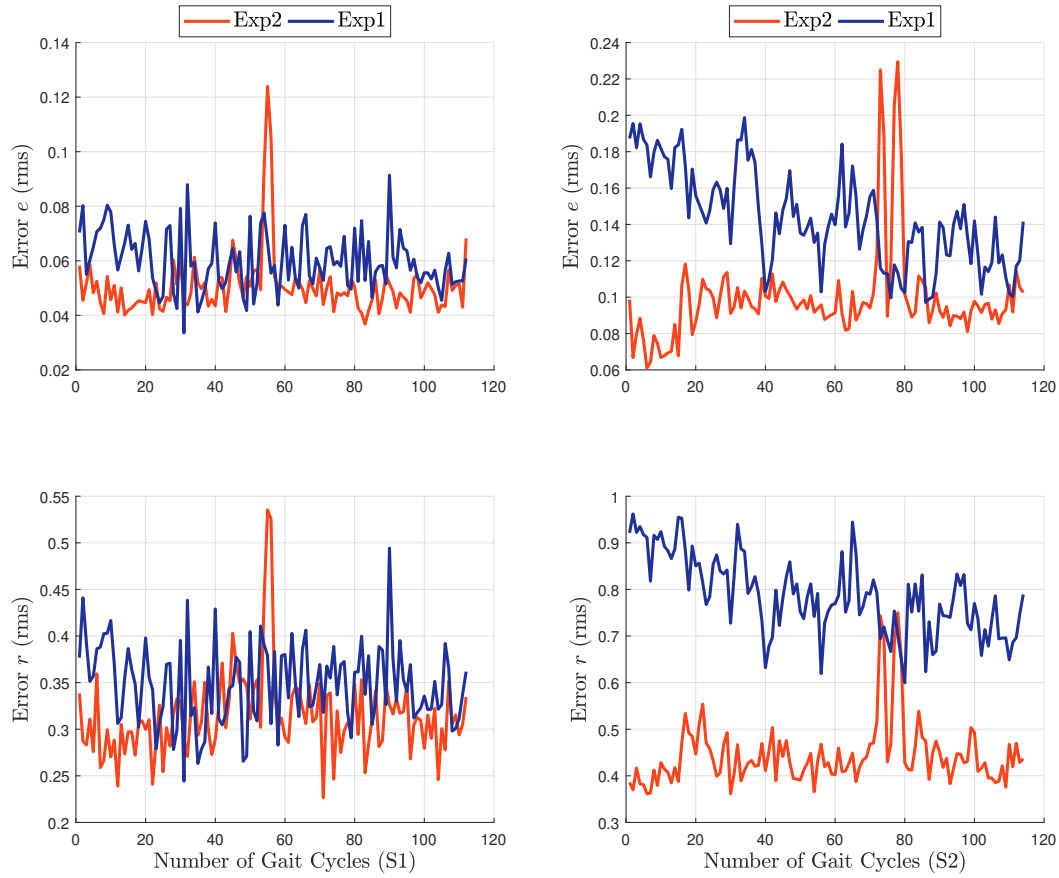
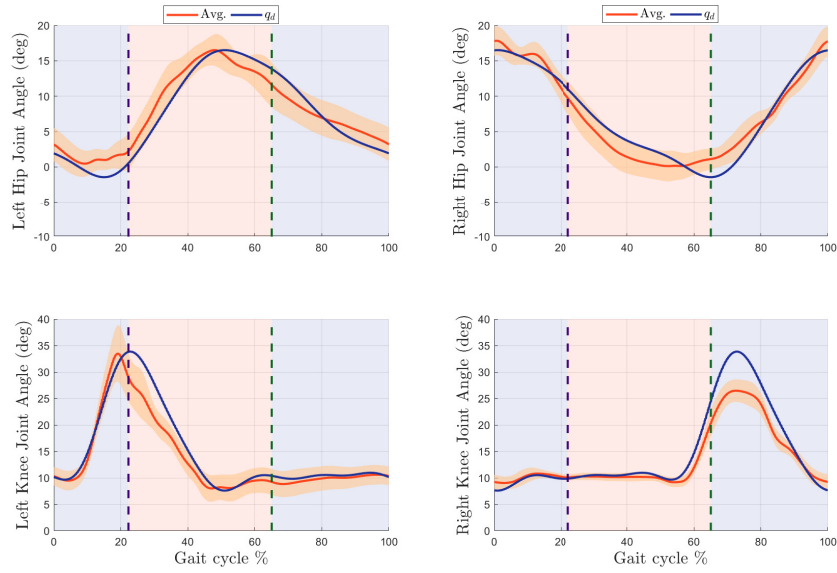
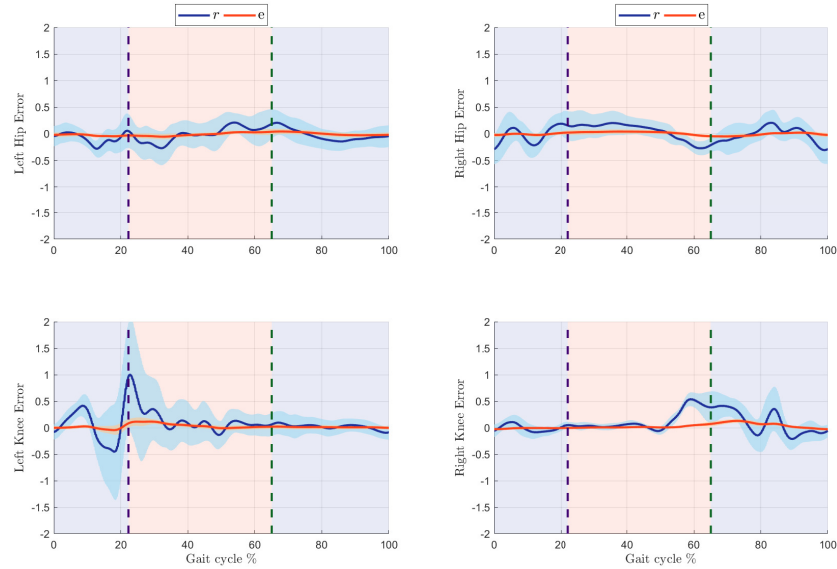


Figure 5.2: Average RMS tracking errors. The top plots show the average RMS position error e across all joints during each gait cycle. The bottom plots show the average RMS filtered error r . The performance plots in the left and right columns correspond to subject S1 and subject S2, respectively.

for each step cycle, and then averaged across all joints and all cycles to obtain an overall RMS error for each experiment. A Wilcoxon signed ranked test was applied to evaluate the pairwise difference of the RMS tracking error across each gait cycle between the two experiments (i.e., Exp1-Exp2). The results indicate a significant difference ($p\text{-value} < 0.05$) across the step cycles between experiments for both subjects. Figure 5.2 illustrates the RMS errors averaged across all joints, where Exp1 is depicted in blue and Exp2 in orange. The average tracking performance for subject S1 in Exp2 is illustrated in Figure 5.3 as a function of the gait cycle percentage. Figure 5.3a shows the average trajectory tracking for all joints (top plots illustrate the hip joints,



(a) Kinematic trajectories as function of the gait cycle percentage. The top plots illustrate the trajectories of the left and right hip joints. The bottom plots illustrate the trajectories of the left and right knee joints. The desired trajectories (q_d) are depicted in blue and the actual average (± 1 std) joint angles are depicted in orange.



(b) Kinematic tracking error as a function of the gait cycle percentage. The top plots illustrate the error of the left and right hip joints. The bottom plots illustrate the error of the left and right knee joints. The average (± 1 std) position error e (rad) is depicted in orange whereas the average (± 1 std) error signals r , computed with \dot{e} in rad/s and e in rad, are depicted in blue.

Figure 5.3: Kinematic tracking performance for subject S1 undergoing eight minutes of treadmill walking at a speed of 0.48 steps/s during Exp2. The vertical dashed lines indicate the average switching instances, where the orange background indicates $\sigma = 1$ and the blue indicates $\sigma = 2$.

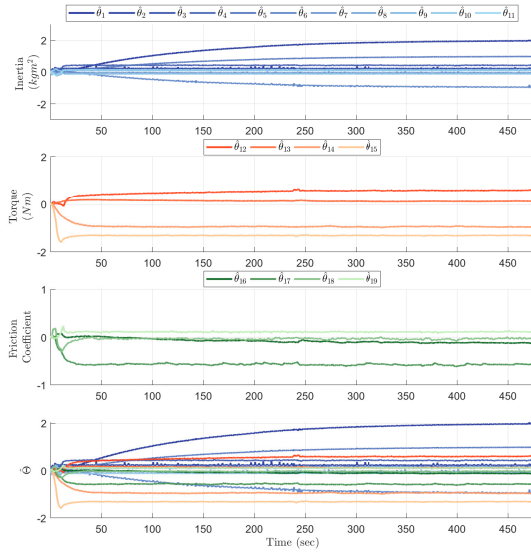
Table 5.3: Average RMS tracking error \bar{e}_{rms} and \bar{r}_{rms} . For each joint, the RMS value is calculated by averaging the error across all gait cycles, and then the RMS values of all joints are averaged to obtain an overall measure of tracking error. The difference is calculated and compared using a Wilcoxon signed ranked test for pairwise differences on each gait cycle. * denotes p-value < 0.05 .

Subject	Experiment	\bar{e}_{rms} (rad)	\bar{r}_{rms} (rad/s)
S1	Exp 1	0.06	0.35
	Exp 2	0.05	0.31
	Diff.	0.01*	0.04*
S2	Exp 1	0.14	0.79
	Exp 2	0.10	0.44
	Diff	0.04*	0.35*

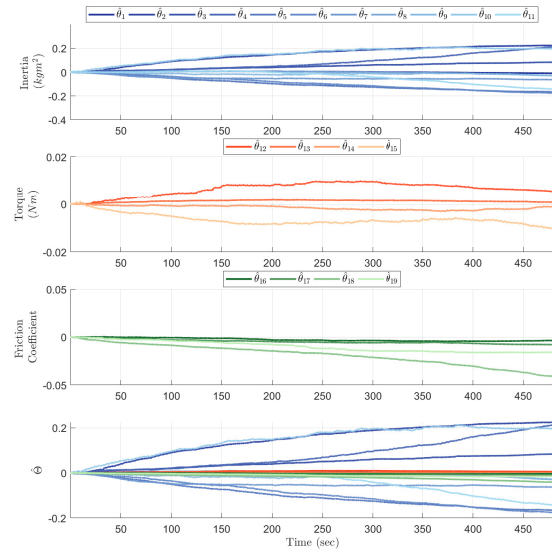
whereas the bottom plots illustrate the knee joints), where the desired trajectory is depicted in blue and the actual average trajectory across all gait cycles is depicted in orange (with ± 1 std depicted in the shaded orange along the trajectory). Similarly, the tracking error is illustrated in Figure 5.3b, where the error e in orange and r in blue are averaged across all gait cycles. In Figure 5.3, the background colors indicate the gait phase, where $\sigma = 1$ is depicted in orange and $\sigma = 2$ in blue (as illustrated in Figure 2.2). Moreover, the dashed lines indicate the average switching instances transferring from one phase to the other. The gait cycle is expressed as a percentage of a full stride, with the right heel strike used as the reference point (i.e., at the right heel strike, the gait percentage is 0%).

Parameter Estimation

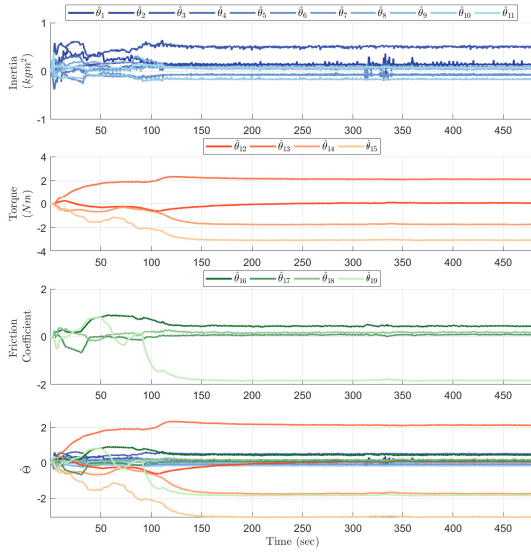
The parameter estimates are divided into three categories: *inertial* parameters (kgm^2) shown in blue, *torque* parameters (Nm) shown in orange, and *viscous-damping* coefficients shown in green in Figure 5.4 (see Section 5.2). Figure 5.4 illustrates the evolution of the parameter estimation for all experiments, with individual plots showing each category and the bottom plots showing all parameters combined. The plots in the left column depict the performance during Exp2, while the plots in the right column show the performance during Exp1 for both subjects. The parameter



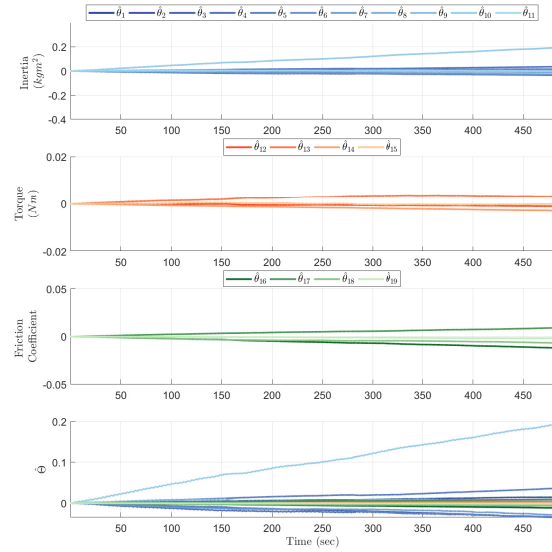
(a) Exp2 S1



(b) Exp1 S1



(c) Exp2 S2



(d) Exp1 S2

Figure 5.4: Parameter estimates for subject S1 corresponding to (a) Exp2 and (b) Exp1, and subject S2 corresponding to (c) Exp2 and (d) Exp1. The estimation of the uncertain parameters (described in Section 5.2) is illustrated for eight-minute treadmill walking experiments. The parameters are divided into three groups: Inertial parameters (blue) in kgm^2 , gravitational torque parameters (orange) in Nm , and viscous-damping coefficients (green). The bottom plots for all experiments depict all the parameter estimates combined.

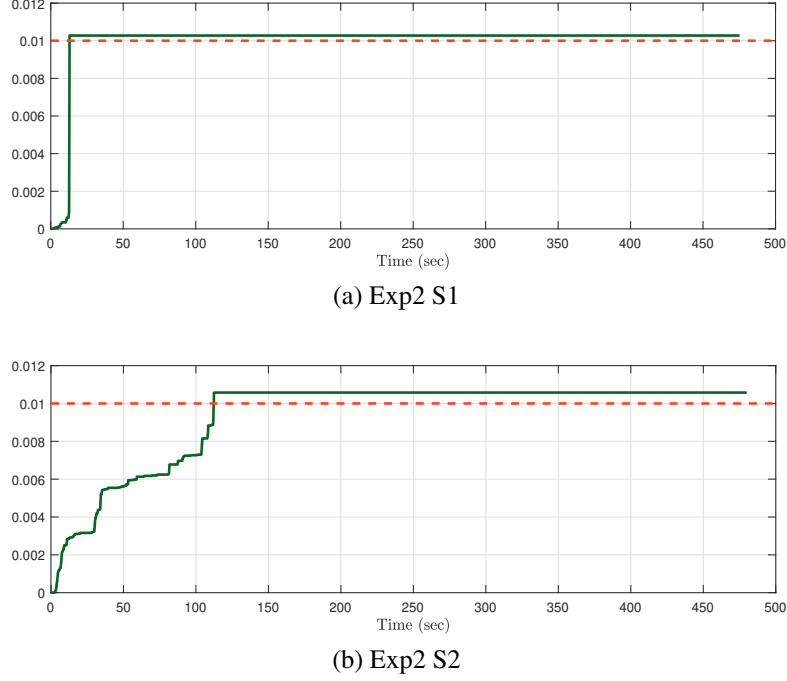
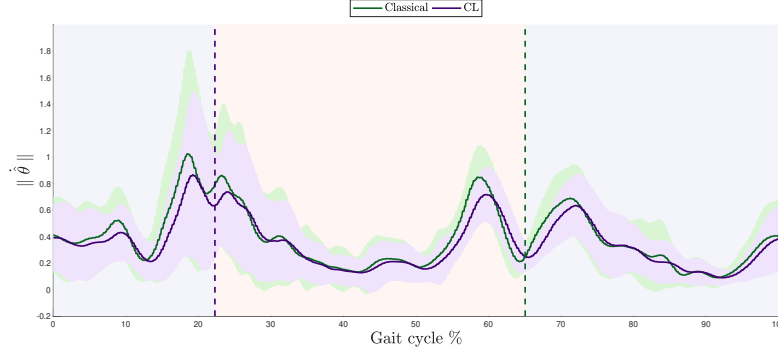


Figure 5.5: Evolution of the minimum eigenvalue of the history stack, i.e., $\lambda_{\min}\{\sum_{p=1}^{\bar{p}} \mathcal{Y}_p^T \mathcal{Y}_p\}$ for (a) subject S1 and (b) subject S2 during Exp2. The dashed line in red shows the user-defined finite excitation condition $\underline{\lambda}$.

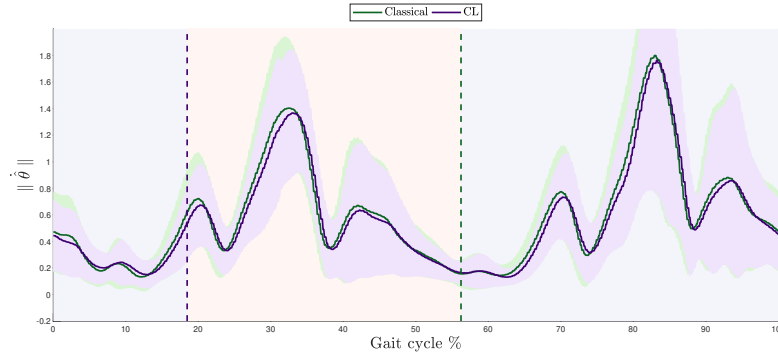
estimates were initialized at zero, i.e., $\hat{\Theta}(t_0) = \text{zeros}([19, 1])$, for all the experiments. Figure 5.5 shows the evolution of the minimum eigenvalue of the history stack under Exp2 for both subjects, with the dashed line indicating the finite excitation condition threshold $\underline{\lambda}$ selected for these experiments. Figure 5.6 illustrates the average contribution of each term in the adaptive update law in (5.7) under Exp2 for both participants, with the classical gradient-descent term shown in green and the integral concurrent learning term shown in purple.

Control Effort

Figure 5.7 shows the average control input commanded across all gait cycles for subject S1 under Exp2. The computed command u_σ is illustrated for all joints in Figure 5.7a. The control input in (5.5) can be divided into two terms: the feedback term $(k_\sigma + e)$ and the adaptive term $(Y_\sigma \hat{\Theta})$. The contribution of each of these terms on the control signal is illustrated in Figure 5.7b, where



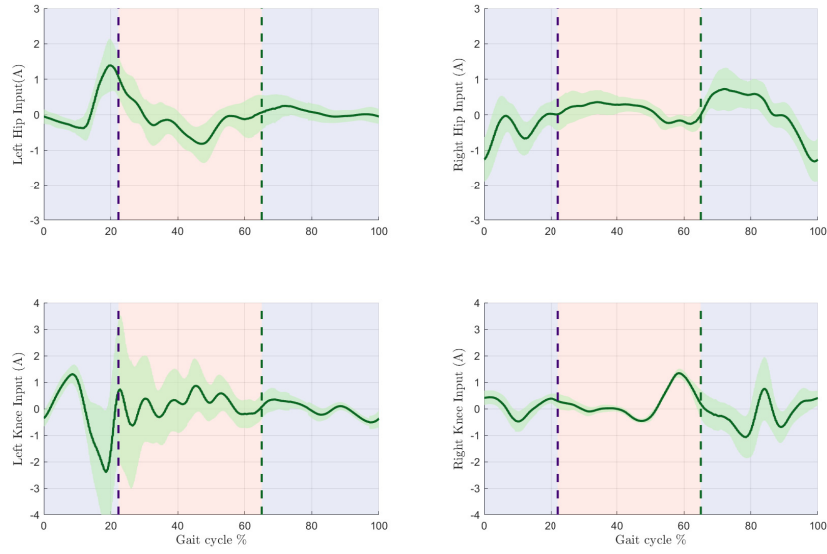
(a) Exp2 S1



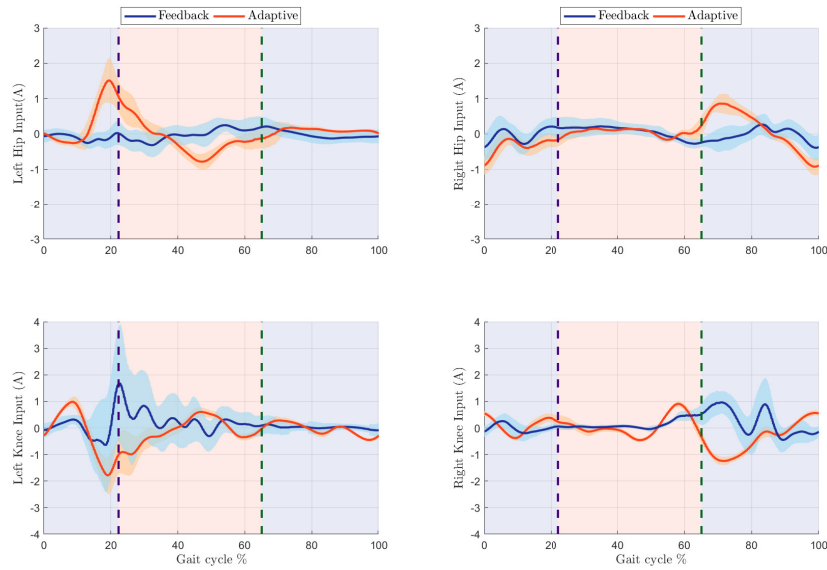
(b) Exp2 S2

Figure 5.6: Magnitude of the average (± 1 std) contribution of each term in the adaptive update law in (5.7) as a function of the gait cycle percentage during Exp 2 for both participants. The classical gradient-descent term is defined as $Classical = \|\Gamma Y_{\sigma}^T r\|$ (green), whereas the integral concurrent learning term is defined as $CL = \|k_{cl} \Gamma \sum_{p=1}^{\bar{p}} \mathcal{Y}_{\sigma}^T(t_p)(\mathcal{V}_{\sigma}(t_p) - \mathcal{Y}_{\sigma}(t_p)\hat{\Theta}(t))\|$ (purple). The vertical dashed lines indicate the average switching instances, where the orange background indicates $\sigma = 1$ and the blue indicates $\sigma = 2$.

the average feedback term is depicted in blue and the average adaptive term is depicted in orange. Figure 5.8 shows the FES input delivered to the quadriceps (orange) and hamstrings (blue) in subject S1 on both legs during Exp2 for a period of 15 seconds. The average RMS control input generated for all experiments is shown in Figure 5.9 presented for subjects S1 (top) and S2 (bottom) across all gait cycles. The RMS value of the feedback and adaptive input contributions is shown in Figure 5.10, where the average RMS feedback (blue) and adaptive (orange) input contributions across all joints is presented for subject S1 (top plots) and subject S2 (bottom plots) during all gait cycles.



(a) Average (± 1 std) control inputs for subject S1. The top plots illustrate the control input delivered to the left and right hip joints and the bottom plots illustrate the input delivered to the left and right knee joints. The vertical dashed lines indicate the average switching instances, where the orange background indicates $\sigma = 1$ and the blue indicates $\sigma = 2$.



(b) The average (± 1 std) control contributions in the controller in (5.5) are illustrated. The top plots illustrate the control contribution delivered to the left and right hip joints and the bottom plots illustrate the control contribution delivered to the left and right knee joints. The blue plot shows the state feedback term ($k_e r + e$) while the orange signal shows the adaptive term contribution $Y_\sigma \hat{\Theta}$ for each joint.

Figure 5.7: Average control inputs for subject S1 (a) applied to the hip and knee joints and (b) segregated by the contribution of the feedback and adaptive terms.

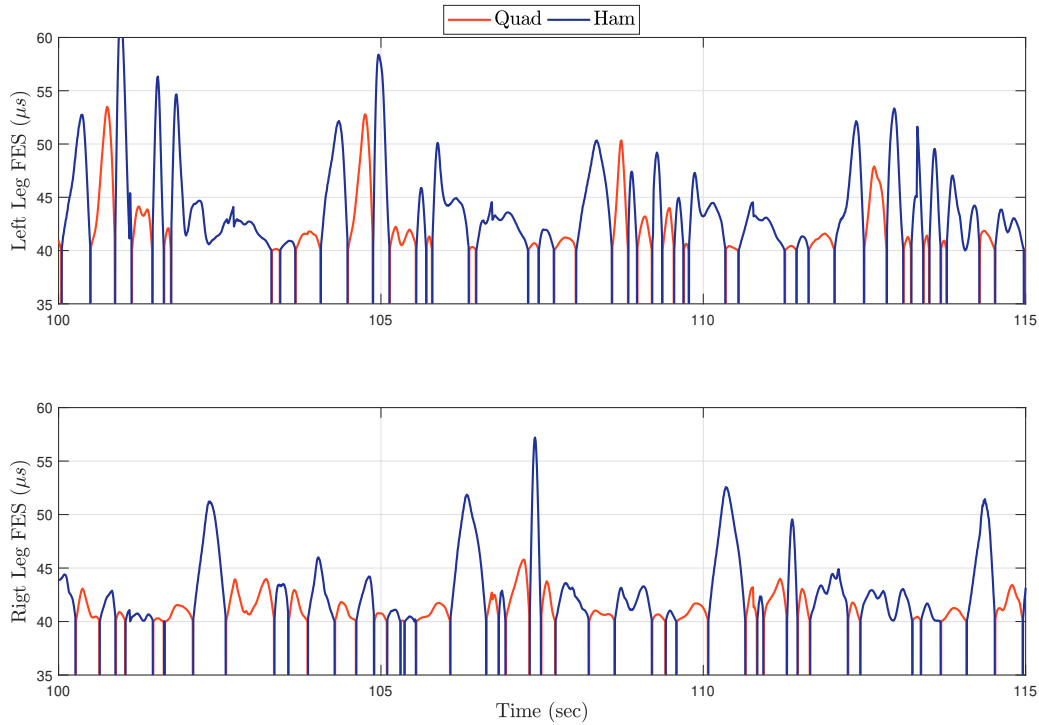


Figure 5.8: FES pulse width input (μs) delivered to left (top) and right (bottom) quadriceps (orange) and hamstrings (blue) for subject S1 during experiment Exp2. The input signal is shown for an interval of 15 seconds.

5.5 Discussion

This section provides a discussion of the results presented in the previous section, focusing on three key aspects: gain tuning and hyper-parameter selection, tracking and input performance, and parameter estimation convergence.

5.5.1 Gain tuning and hyper-parameter selection

Gain tuning had a direct impact on gait performance during experiments. The tuning strategy involved initially selecting the feedback and input gains (listed in Table 5.1) to achieve a satisfactory, fast response of the electric motors and prevent discomfort in the participants due to applying FES. Next, the adaptive gain matrix Γ was tuned to ensure a bounded response for the

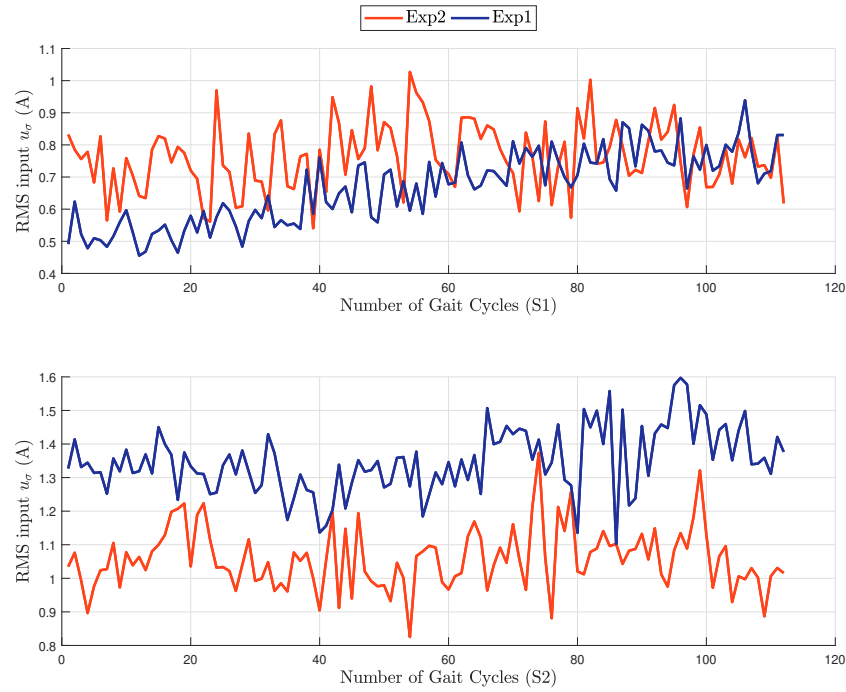


Figure 5.9: RMS control input u_σ averaged across all joints for all gait cycles. The top plot illustrates the average input delivered to subject S1 for both experiments, whereas the bottom plot shows the input delivered to subject S2.

adaptive estimation during the transient phase of the experiments, and k_{cl} was tuned for Exp2 to ensure the concurrent learning term had a significant contribution in the input, as shown in Figure 5.6. Notably, tuning Γ proved to be considerably more challenging in Exp1 for both participants, as the system was highly sensitive to this parameter resulting in large transients. Table 5.1 shows the selection of Γ for the participants, where the adaptive gain values differ significantly between experiments and participants with much lower values for Exp1 compared to Exp2 (i.e., due to the sensitivity of Γ directly influencing the closed-loop performance). Testing different gain values in Γ resulted in rapid unbounded behavior on the estimates in Exp1, which imposed the need for tuning using an iterative (trial and error) approach. Drastically different in Exp2, the same Γ worked for both subjects (despite different body types), and the adaptive system was less sensitive to variations in this gain, leading to satisfactory and predictable performance from the beginning of the experiment. The gain tuning process in both experiments highlights one of the

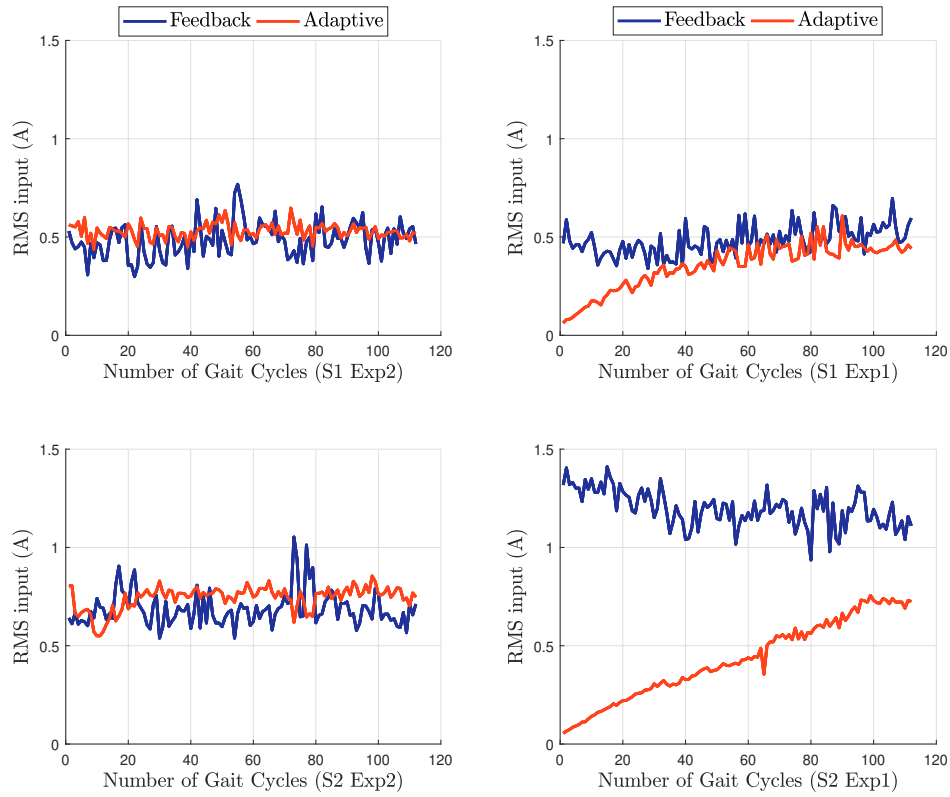


Figure 5.10: RMS feedback and adaptive control input contributions averaged across all joints for all gait cycles. The top plots illustrate the average inputs delivered to subject S1 for both experiments, whereas the bottom plots show the inputs delivered to subject S2.

advantages of concurrent learning over classical adaptive learning, as concurrent learning allows for flexible tuning, which is a key aspect in the development of human-in-the-loop applications. The size of the history stack \bar{p} and the integration window δt were selected exactly the same for both participants to demonstrate the feasibility and allow for fair comparisons between experiments. The minimum requirement for \bar{p} is the size of the parameter vector Θ (i.e., dimension 19 in this case) to allow for a full rank matrix. The integration window must be selected to balance computational cost and the level of smoothness that is desired for the integral input and output.

5.5.2 Tracking and Input Performance

Table 5.3 presents the tracking performance results. Exp2 leverages the concurrent learning controller and significantly outperforms Exp1 using the classical adaptive controller for both participants (p-value < 0.05). As depicted in Figure 5.2, the RMS error e and r are smaller for Exp2 compared to Exp1 for the majority of the time. To ensure a fair comparison of the tracking results, the inputs delivered to the system were also analyzed. Figure 5.9 shows that, for subject S1, the input levels reached similar values towards the end of the experiments for both methods. For subject S2, it can be observed from Figure 5.9 that Exp2 delivered less input than Exp1 and achieved a better tracking performance.

The feedback and adaptive control term contributions change during the walking experiments. In Figure 5.10 (right column) corresponding to Exp1, the feedback term takes over during the initial phase of the trials while the adaptive term slowly increases. This slow growth of the adaptive term is due to the critical tuning of the Γ matrix required to ensure the boundedness of the adaptive term in Exp1 (and satisfactory closed-loop tracking performance) for both participants. Conversely, in Exp2, the adaptive term has a significant contribution throughout the experiment for both subjects as depicted in Figure 5.10 (left column). This demonstrates the benefit of using the concurrent learning controller as it allows to increase the influence of the adaptive term from the beginning of the experiments and reduces dependence on the control feedback term. The reduced reliance on the feedback term is particularly relevant for the control of hybrid exoskeletons where high-gain feedback may yield undesired, aggressive behaviors or discomfort due to applying large FES inputs.

5.5.3 Parameter estimation convergence

Figure 5.4 presents the trajectories of the parameter estimates corresponding to Exp1 (right column) and Exp2 (left column) for both participants. The trajectories of the estimates obtained

in Exp2 reach a steady state value for both participants compared to several estimates obtained in Exp1 that do not settle to a steady state value or remain static (i.e., due to the lack of persistence of excitation). Parameter convergence is not guaranteed during the implementation of the classical adaptive controller in Exp1 due to the switching effects. Moreover, the gradient-based controller traditionally achieves asymptotic tracking without switching [60]. Thus, the classical adaptive controller cannot be used to guarantee the stability of the closed-loop error system due to the switching effects. Hence, its experimental implementation is performed as a benchmark and is limited due to the sensitivity to gain tuning and experiences poor transient performance, which can result in unstable walking behavior due to switching. Similar undesirable behavior is observed in some of the trajectories of the parameter estimates because they exhibit unbounded growth (and do not converge to a steady state value) as depicted in Figure 5.4 (right column). The lack of steady-state convergence of the adaptive estimates obtained in the implementation of the gradient-based controller is expected due to the inability to guarantee convergence (i.e., since persistence of excitation is not injected in experiments due to the ensuing detrimental gait performance) and the switching of the update law in (5.7). In contrast, the concurrent learning controller implemented in Exp2 ensures parameter convergence through the developed stability analysis. This is achieved by ensuring that the history stack is full-rank, as demonstrated in Figure 5.5, where the minimum eigenvalue is maximized to accelerate convergence. Unlike Exp1, the switching does not affect the steady-state convergence of the parameters in Exp2, rendering it a better design alternative for switching systems.

The uncertain parameters in the dynamic model in (2.5) vary across participants. Despite the stability analysis guarantees exponential tracking and parametric convergence, the parameter estimates do not converge to the actual values that have been reported in literature-based anthropometric data [61]. However, fundamentally, the parameters described in Section 5.2 are unknown and user-dependent. The lack of convergence of the parametric estimates to the reported, actual parameters can be partially attributed to the inherent challenges of real-time experiments, where the system is exposed to noisy measurements and perturbations that affect the input-output re-

lationship in (5.13), thereby affecting the direction of the gradient. Moreover, the design of the adaptive controller exploits modeling assumptions that may differ from the real dynamics, affecting the input-output relationship and thus, potentially driving the parameter estimates away from their true values.

The experimental results demonstrate the feasibility of the control design in (5.5) and concurrent learning update law in (5.7) to actuate a hybrid lower-limb exoskeleton for treadmill walking.

One of the contributions of this work was to demonstrate that the controller achieves satisfactory and customized walking performance by combining muscle and motor inputs. The muscle response is nonlinear and uncertain, and thus, can yield jerky walking motion if muscles are not controlled systematically. An additional challenge for the control of hybrid exoskeletons is that muscles fatigue [12], which degrades tracking performance compared to powered exoskeletons without FES. The concurrent learning design outperforms classical adaptive controllers in different aspects, such as mitigating the need for fine-tuning the control gains for different participants, reducing the reliance on high-gain feedback terms that make the system susceptible to large control inputs, and ensuring convergence of the parameter estimates that are robust to the switching effects. However, the current gait control design experiences the following limitations that motivate future extensions: (i) The model does not consider the double-stance support phase. This is a mild assumption for the current implementation as demonstrated by the satisfactory real-time walking experiments. As shown in Table 5.2, the double support phase lasts on average less than 10% of the total step cycle duration, which is minimal compared to the single-stance support phases. Extension of the presented model to account for the double support is motivated for the future design of adaptive gait controllers. (ii) Additional analysis is motivated to examine and guarantee the convergence of the parametric estimates to the reported parameters in literature based on anthropometric data [61]. The real-time experiments experience disturbances and noise that are complex factors to be included in the model, control design, and analysis in the context of adaptive control [29]. Future extensions are motivated to improve the quality of data used to establish the input-output relationship and also account for disturbances and unmodeled effects as

discussed in [62], [63].

5.6 Conclusion

A switching concurrent learning adaptive controller was designed for joint kinematic tracking using a cable-driven hybrid exoskeleton during treadmill walking at a constant speed. A switching Euler-Lagrange model was developed to account for the gait phase transitions. Hybrid actuation was implemented combining FES to induce muscle contractions in the quadriceps and hamstrings muscle groups and electrical motors actuating Bowden cables. The switching adaptive controller was also designed to estimate the constant uncertain parameters and use the adaptive estimates as feedforward input terms in the tracking controller in (5.5); such adaptation is determined by a concurrent learning technique inspired by [32], [36], which exploits input-output data to achieve an exponential tracking result and convergence of the adaptive estimates. Thus, this work leverages concurrent learning for kinematic tracking in the human-exoskeleton system using switched systems tools. A dwell time condition [14] was developed to demonstrate exponential tracking of the overall switching system using a multiple Lyapunov function approach.

Chapter 6

Conclusions

6.1 Contributions and conclusions

This dissertation focuses on developing adaptive controllers that leverage kinematic and torque feedback for powered lower-limb cycles and exoskeletons modeled as nonlinear, time-varying, and uncertain switched systems. Closed-loop adaptive controllers are developed to achieve the desired tracking performance while coping with the inherent uncertainties in the human-robot dynamics by estimating their unknown parameters. Specifically, this dissertation focuses on the design and analysis of switching concurrent learning controllers using Lyapunov-based methods. The design, analysis, and implementation of controllers that activate muscles and motors for assisted cycling and walking have implications for advancing gait rehabilitation. Ultimately, the benefits of hybrid exoskeletons and motorized cycles have to be examined in clinical studies with people with neurological conditions.

In Chapter 3, a switching integral concurrent learning controller was developed to track a desired cadence for a motorized FES-cycling system. The adaptive cadence controller was designed to improve tracking and generate estimates of the uncertain parameters in the cycle-rider dynam-

ics and uncertain constant muscle control effectiveness in real time. Due to muscle switching needed to engage muscles in the left and right legs during FES-cycling, the adaptive controller exploits a switching update law where the muscle torque control input is exploited as a feedforward control term into the electric motor controller. Rather than canceling the muscle input as an exogenous input, the adaptive control approach embeds the muscle input into the regressor and facilitates estimating the muscle's uncertain effectiveness. A Lyapunov stability analysis for switching systems was developed leveraging a common Lyapunov function to demonstrate exponential kinematic tracking and parameter estimation convergence after a FE condition is satisfied. Particularly, a recent result for nonautonomous switched systems was exploited since a negative semi-definite Lyapunov derivative was obtained during the initial learning phase (i.e., when the FE condition is not yet satisfied) [41].

To demonstrate the feasibility of the control design, three ten-minute cycling experiments were implemented in eight able-bodied individuals resulting in 24 total cycling trials. Moreover, three participants with NCs tested the system during three five-minute trials. The cycling experiments were conducted to examine the control performance under different cadence trajectories and learning conditions. The first cycling experiment (EXP1) illustrates the system's performance by implementing a constant target cadence and initializing the history stack empty and the adaptive estimates to zero (i.e., no previous learning or knowledge of the system is exploited). The second experiment (EXP2) illustrates the system's performance implementing a staircase-like cadence trajectory (i.e., changing the target cadence during the transient until reaching a steady-state constant cadence). EXP2 facilitated the satisfaction of the predetermined FE condition. The third experiment (EXP3) tracked a constant cadence trajectory exploiting the learned parameters computed at the end of the cycling trial EXP2. Satisfactory cadence tracking performance was obtained by initializing the adaptive update law with the learned parameters from EXP2; thus, illustrating the ability of the controller to learn useful estimates for tracking during a separate cycling trial. Results from all participants showed that the adaptive controller satisfied the predetermined FE condition in EXP2 compared to EXP1, where the predefined FE condition is not

satisfied; yet, the minimum eigenvalue remained positive during all trials. By leveraging previously learned data in the cycling experiments from EXP2 into EXP3, across all participants, it was observed that the position error $e(t)$ presented a significantly faster convergence in the cycling trial EXP3 compared to EXP1 and EXP2.

One of the main contributions of this work was the ability to simultaneously estimate uncertain parameters of the cycle-rider system and the uncertain muscle control effectiveness, which was considered to be a unknown constant. Future efforts will expand the developed work to include models of the control effectiveness that are state-dependent and time-varying [12]. Complex models of the musculoskeletal dynamics can be used in subsequent work to potentially enhance the design of the adaptive update law and control design. Moreover, leveraging the control structure developed in this paper, multi-objective control such as power tracking for FES-cycling will be examined.

In Chapter 4, a power-tracking control design for muscles and an electric motor was developed and implemented in cycling experiments to demonstrate its feasibility. For the first time, an active torque tracking controller with anti-windup compensation was designed to cope with muscle input saturation. The switched concurrent learning cadence controller, developed in Chapter 3, was implemented to maintain the cycle at a constant speed. The muscle and motor control designs are motivated to exploit input-output data from the active torque produced by the muscles to improve cadence tracking by using the muscle inputs as feedforward terms into the motor cadence controller. The adaptive cadence controller achieves exponential tracking and parameter estimation of the cycle-rider uncertain parameters after a finite excitation condition is satisfied (i.e., after collecting sufficiently rich input-output data). The muscle controller with the anti-windup term achieves GUUB torque tracking. Two cycling trials with one able-bodied participant were performed. Results demonstrated the efficacy of the anti-windup compensation to avoid error build-up when the input is saturated. Future work will be oriented to develop adaptive methods to cope with a nonlinear, state-dependent, and potentially time-varying control effectiveness term.

Testing in additional participants will be conducted in future efforts considering the case where the participants exert volitional effort to characterize the performance of the torque controller.

In Chapter 5 and for the first time, a switching concurrent learning adaptive controller was designed for joint kinematic tracking using a cable-driven hybrid exoskeleton during treadmill walking at a constant speed. A switching Euler-Lagrange model was developed to account for the gait phase transitions. Hybrid actuation was implemented combining FES to induce muscle contractions in the quadriceps and hamstrings muscle groups and electrical motors actuating Bowden cables. The switching adaptive controller was also designed to estimate a set of constant uncertain parameters and use the adaptive estimates as feedforward input terms in the tracking controller in (5.5); such adaptation is determined by a concurrent learning technique inspired by [32], [36], which exploits input-output data to achieve an exponential tracking result and convergence of the adaptive estimates. Thus, this chapter leverages concurrent learning for kinematic tracking in the human-exoskeleton system using switched systems tools. A dwell time condition [14] was developed to demonstrate exponential tracking of the overall switching system using a multiple Lyapunov function approach.

The experimental results obtained with the concurrent learning controller demonstrated improved kinematic tracking performance for knee and hip joints bilaterally compared to the classical gradient-based adaptive controller. The designed concurrent learning controller holds the potential to be tested in a larger sample size of participants including people with movement disorders after a stroke or SCI. Future work includes enhancing the robustness of the developed controller to muscle fatigue and external disturbances (e.g., muscle spasms) that can affect the convergence of the adaptive estimates in experiments involving individuals with movement disorders. In addition, the adaptive controller will be implemented in walking trials with different speeds to examine the convergence of the estimates of the parameters and assess the performance for tracking diverse gait patterns.

6.2 Research directions

The experiments conducted in this dissertation were developed to demonstrate the feasibility of the developed control methods. However, future work will involve validating these methods in mechanistic and longitudinal clinical studies. This is likely to present additional control challenges due to reduced muscle mass and strength, faster rates of muscle fatigue, and spasticity. Personalizing the control gains to balance the need for suitable tracking performance with the sensory challenges that may limit FES control authority in people with neurological conditions is a potential direction. Novel adaptive control techniques are also motivated to identify critical parameters of the dynamic system and improve how control is shared to enhance user assistance as muscle fatigues.

6.2.1 Input-Output Relationship

As presented in the experimental results in all chapters of this dissertation, one limitation of the current work is that the estimated parameters of the concurrent learning method do not appear to converge to the actual values based on anthropometric data [61]. The potential mismatch between the estimated and actual parameters can arise due to the definition of the input-output (I-O) relationship described in (3.18) and (5.13), which is measurable and assumed to fully describe the dynamic behavior of the system. However, in real-time experiments, external disturbances and measurement noise are likely affecting this I-O relationship. For example, at each sampled time t_p , an unknown and unmeasurable disturbance (or perturbation) ϵ_p influences the I-O relation as follows

$$\mathcal{Y}(t_p)\Theta = \mathcal{V}(t_p) + \epsilon_p. \quad (6.1)$$

As a result, when computing the concurrent learning term of the update law in (3.19) or (5.14), substituting the perturbed input-output relationship yields

$$\sum_{p=1}^{\bar{p}} \left(\mathcal{Y}_{\sigma}^T(t_p) \mathcal{Y}(t_p) \tilde{\Theta} - \mathcal{Y}_{\sigma}^T(t_p) \epsilon_p \right), \quad (6.2)$$

where the perturbation is changing the direction of the gradient, precluding the system from converging in the direction that reduces the estimation error $\tilde{\Theta}$ (i.e., achieve convergence to the actual parameters). Addressing this limitation is an active area of research in the adaptive control community [29], especially during real-time experiments with human subjects. Future research is motivated from a theoretical perspective, where the control design and stability analysis allow for unmodeled effects and perturbations due to the human-robot interaction or inaccuracies of the measurements. Preliminary work has been developed in this direction to account for noisy measurements with linear systems [62]. However, the analysis for nonlinear systems with switching effects remains an open question that motivates future research beyond the work developed in this thesis.

6.2.2 Convergence Rate

An important finding in the experimental results presented in Chapter 3 and Chapter 5 was the slow convergence rate observed in the estimation of parameters, indicated by the significantly small minimum eigenvalue. The experimental protocol outlined in Chapter 3 demonstrated that this convergence rate can be influenced by the specific trajectories employed in each task. Moreover, it is fundamentally affected by the formulation of the update law. In this dissertation, an adaptive ICL update law was employed, which exploits a gradient-based algorithm and a history stack of input-output data collected. However, there have been preliminary efforts to enhance gradient-based algorithms by incorporating high-order tuners and acceleration methods. These advancements have shown promise in increasing the convergence rate of adaptive concurrent

learning techniques [64], [65] and enhancing transient performance [66]. Consequently, future research directions are motivated to explore similar techniques and apply them, particularly in the context of integral concurrent learning approaches.

References

- [1] K. D. Anderson, “Targeting recovery: Priorities of the spinal cord-injured population,” *J. Neurotrauma*, vol. 21, no. 10, pp. 1371–1383, 2004.
- [2] A. J. Del-Ama, A. D. Koutsou, J. C. Moreno, *et al.*, “Review of hybrid exoskeletons to restore gait following spinal cord injury,” *J. Rehabil. Res. Dev.*, vol. 49, no. 4, pp. 497–514, 2012.
- [3] M. Grimmer, R. Riener, C. J. Walsh, *et al.*, “Mobility related physical and functional losses due to aging and disease - A motivation for lower limb exoskeletons,” *J. Neuroeng. Rehabil.*, vol. 16, no. 1, pp. 1–21, 2019.
- [4] C. Wiesener and T. Schauer, “The Cybathlon RehaBike: Inertial-Sensor-Driven Functional Electrical Stimulation Cycling by Team Hasomed,” *IEEE Robot. Autom. Mag.*, vol. 24, no. 4, pp. 49–57, 2017.
- [5] H. R. Berry, C. Perret, B. A. Saunders, *et al.*, “Cardiorespiratory and power adaptations to stimulated cycle training in paraplegia,” *Med. Sci. Sports Exerc.*, vol. 40, no. 9, pp. 1573–1580, 2008.
- [6] L. Griffin *et al.*, “Functional Electrical Stimulation Cycling Improves Body Composition, Metabolic and Neural Factors in Persons with Spinal Cord Injury,” *J. Electromyogr. Kinesiol.*, vol. 19, no. 4, pp. 614–622, 2009.

- [7] A. Frotzler, S. Coupaud, C. Perret, *et al.*, “High-volume FES-cycling partially reverses bone loss in people with chronic spinal cord injury,” *Bone*, vol. 43, no. 1, pp. 169–176, 2008.
- [8] G. Lv, H. Zhu, and R. D. Gregg, “On the design and control of highly backdrivable lower-limb exoskeletons: A discussion of past and ongoing work,” *IEEE Control Syst.*, vol. 38, no. 6, pp. 88–113, 2018.
- [9] A. J. Young and D. P. Ferris, “State of the Art and Future Directions for Lower Limb Robotic Exoskeletons,” *IEEE Trans. Neural Syst. Rehabil. Eng.*, vol. 25, no. 2, pp. 171–182, Feb. 2017.
- [10] G. Stampacchia, M. Olivieri, A. Rustici, *et al.*, “Gait rehabilitation in persons with spinal cord injury using innovative technologies: an observational study,” *Spinal Cord*, 2020.
- [11] C. Wiesener and T. Schauer, “The Cybathlon RehaBike: Inertial-Sensor-Driven Functional Electrical Stimulation Cycling by Team Hasomed,” *IEEE Robot. Autom. Mag.*, vol. 24, no. 4, pp. 49–57, 2017.
- [12] R. J. Downey, M. Merad, E. J. Gonzalez, *et al.*, “The Time-Varying Nature of Electromechanical Delay and Muscle Control Effectiveness in Response to Stimulation-Induced Fatigue,” *IEEE Trans. Neural Syst. Rehabil. Eng.*, vol. 25, no. 9, pp. 1397–1408, 2017.
- [13] M. Bellman, “Control of cycling induced by functional electrical stimulation: A switched systems theory approach,” Ph.D. dissertation, University of Florida, 2015.
- [14] D. Liberzon, *Switching in Systems and Control*. Boston, MA: Birkhauser, 2003.
- [15] S. Jezernik, R. G. V. Wassink, and T. Keller, “Sliding Mode Closed-Loop Control of FES: Controlling the Shank Movement,” *IEEE Trans. Biomed. Eng.*, vol. 51, no. 2, pp. 263–272, 2004.
- [16] M. J. Bellman, T. H. Cheng, R. J. Downey, *et al.*, “Stationary cycling induced by switched functional electrical stimulation control,” *Proc. Am. Control Conf.*, no. 1161260, pp. 4802–4809, 2014.

- [17] M. J. Bellman, T. H. Cheng, R. J. Downey, *et al.*, “Switched Control of Cadence during Stationary Cycling Induced by Functional Electrical Stimulation,” *IEEE Trans. Neural Syst. Rehabil. Eng.*, vol. 24, no. 12, pp. 1373–1383, 2016.
- [18] H. Kawai, M. J. Bellman, R. J. Downey, *et al.*, “Closed-Loop Position and Cadence Tracking Control for FES-Cycling Exploiting Pedal Force Direction with Antagonistic Biarticular Muscles,” *IEEE Trans. Control Syst. Technol.*, vol. 27, no. 2, pp. 730–742, 2019.
- [19] C. A. Cousin, V. H. Duenas, C. A. Rouse, *et al.*, “Closed-Loop Cadence and Instantaneous Power Control on a Motorized Functional Electrical Stimulation Cycle,” *IEEE Trans. Control Syst. Technol.*, vol. 28, no. 6, pp. 2276–2291, 2020.
- [20] M. Nandor, R. Kobetic, M. Audu, *et al.*, “A Muscle-First, Electromechanical Hybrid Gait Restoration System in People With Spinal Cord Injury,” *Front. Robot. AI*, vol. 8, no. April, pp. 1–11, 2021.
- [21] C. Meijneke, G. Van Oort, V. Sluiter, *et al.*, “Symbitron Exoskeleton: Design, Control, and Evaluation of a Modular Exoskeleton for Incomplete and Complete Spinal Cord Injured Individuals,” *IEEE Trans. Neural Syst. Rehabil. Eng.*, vol. 29, pp. 330–339, 2021.
- [22] J. W. Grizzle, C. Chevallereau, R. W. Sinnet, *et al.*, “Models, feedback control, and open problems of 3D bipedal robotic walking,” *Automatica*, vol. 50, no. 8, pp. 1955–1988, 2014.
- [23] O. Harib, A. Hereid, A. Agrawal, *et al.*, “Feedback Control of an Exoskeleton for Paraplegics,” *IEEE Control Syst. Mag.*, vol. 38, no. December, pp. 61–87, 2018.
- [24] Ayush Agrawal, Omar Harib, Ayonga Hereid, *et al.*, “First Steps Towards Translating HZD Control of Bipedal Robots to Decentralized Control of Exoskeletons,” *IEEE Access*, vol. 5, 2017.
- [25] H. A. Quintero, R. J. Farris, K. Ha, *et al.*, “Preliminary assessment of the efficacy of supplementing knee extension capability in a lower limb exoskeleton with FES,” *Proc. Annu. Int. Conf. IEEE Eng. Med. Biol. Soc. EMBS*, no. 1, pp. 3360–3363, 2012.

- [26] K. H. Ha, H. A. Quintero, R. J. Farris, *et al.*, “Enhancing stance phase propulsion during level walking by combining fes with a powered exoskeleton for persons with paraplegia,” *Proc. Annu. Int. Conf. IEEE Eng. Med. Biol. Soc. EMBS*, pp. 344–347, 2012.
- [27] K. H. Ha, S. A. Murray, and M. Goldfarb, “An Approach for the Cooperative Control of FES with a Powered Exoskeleton during Level Walking for Persons with Paraplegia,” *IEEE Trans. Neural Syst. Rehabil. Eng.*, vol. 24, no. 4, pp. 455–466, 2016.
- [28] N. A. Alibeji, V. Molazadeh, F. Moore-Clingenpeel, *et al.*, “A muscle synergy-inspired control design to coordinate functional electrical stimulation and a powered exoskeleton: Artificial generation of synergies to reduce input dimensionality,” *IEEE Control Syst. Mag.*, vol. 38, no. 6, pp. 35–60, 2018.
- [29] A. M. Annaswamy and A. L. Fradkov, “A historical perspective of adaptive control and learning,” *Annu. Rev. Control*, vol. 52, no. October, pp. 18–41, 2021. arXiv: [2108.11336](#).
- [30] K. S. Narendra and A. M. Annaswamy, *Stable Adaptive Systems*. USA: Prentice-Hall, Inc., 1989.
- [31] G. Chowdhary and E. Johnson, “Concurrent learning for convergence in adaptive control without persistency of excitation,” *Proc. IEEE Conf. Decis. Control*, no. 4, pp. 3674–3679, 2010.
- [32] A. Parikh, R. Kamalapurkar, and W. E. Dixon, “Integral concurrent learning: Adaptive control with parameter convergence using finite excitation,” *Int. J. Adapt. Control Signal Process.*, vol. 33, no. 12, pp. 1775–1787, 2019.
- [33] S. Basu Roy, S. Bhasin, and I. N. Kar, “Composite Adaptive Control of Uncertain Euler-Lagrange Systems with Parameter Convergence without PE Condition,” *Asian J. Control*, vol. 22, no. 1, pp. 1–10, 2020.
- [34] M. Sastry, Shankar and Bodson, *Adaptive control: stability, convergence and robustness*. Courier Corporation, 2011.

- [35] G. Chowdhary, M. Mühlegg, and E. Johnson, “Exponential parameter and tracking error convergence guarantees for adaptive controllers without persistency of excitation,” *Int. J. Control*, vol. 87, no. 8, pp. 1583–1603, 2014.
- [36] J. Casas, C.-H. Chang, and V. H. Duenas, “Motorized and Functional Electrical Stimulation Induced Cycling via Switched Adaptive Concurrent Learning Control,” in *ASME 2020 Dyn. Syst. Control Conf. DSCC 2020*, 2020.
- [37] G. R. Merritt, S. Akbari, and C. A. Cousin, “Integral Concurrent Learning for Admittance Control of a Hybrid Exoskeleton,” *IFAC-PapersOnLine*, vol. 55, no. 41, pp. 77–82, 2022.
- [38] B. C. Allen, K. J. Stubbs, and W. E. Dixon, “Adaptive Trajectory Tracking During Motorized and FES-Induced Biceps Curls via Integral Concurrent Learning,” *ASME 2020 Dyn. Syst. Control Conf. DSCC 2020*, vol. Volume 1: 2020.
- [39] B. C. Allen, K. J. Stubbs, and W. E. Dixon, “Data-based and Opportunistic Integral Concurrent Learning for Adaptive Trajectory Tracking During Switched FES-Induced Biceps Curls,” *IEEE Trans. Neural Syst. Rehabil. Eng.*, vol. 30, no. 11c, pp. 2557–2566, 2022.
- [40] G. Chowdhary and E. Johnson, “A singular value maximizing data recording algorithm for concurrent learning,” *Proc. Am. Control Conf.*, pp. 3547–3552, 2011.
- [41] R. Kamalapurkar, J. A. Rosenfeld, A. Parikh, *et al.*, “Invariance-Like Results for Nonautonomous Switched Systems,” *IEEE Trans. Automat. Contr.*, vol. 64, no. 2, pp. 614–627, 2019.
- [42] M. J. Bellman, R. J. Downey, A. Parikh, *et al.*, “Automatic Control of Cycling Induced by Functional Electrical Stimulation With Electric Motor Assistance,” *IEEE Trans. Autom. Sci. Eng.*, vol. 14, no. 2, pp. 1225–1234, 2017.
- [43] V. H. Duenas, C. A. Cousin, A. Parikh, *et al.*, “Motorized and Functional Electrical Stimulation Induced Cycling via Switched Repetitive Learning Control,” *IEEE Trans. Control Syst. Technol.*, vol. 27, no. 4, pp. 1468–1479, 2019.
- [44] F. L. Lewis, D. M. Dawson, and C. T. Abdallah, *Robot Manipulator Control*. 2003, p. 638.

- [45] N. A. Kirsch, N. A. Alibeji, and N. Sharma, “Nonlinear Model Predictive Control of Functional Electrical Stimulation,” in *Vol. 2 Diagnostics Detect. Drilling; Dyn. Control Wind Energy Syst. Energy Harvest. Estim. Identification; Flex. Smart Struct. Control. Fuels Cells/Energy Storage; Hum. Robot Interact. HVAC Build. Energy M*, vol. 2, American Society of Mechanical Engineers, Oct. 2015, pp. 319–331.
- [46] D. Popovic, R. B. Stein, M. N. Oguztoreli, *et al.*, “Optimal control of walking with functional electrical stimulation: A computer simulation study,” *IEEE Trans. Rehabil. Eng.*, vol. 7, no. 1, pp. 69–79, 1999.
- [47] C. H. Chang, J. Casas, S. Brose, *et al.*, “Closed-loop Torque and Kinematic Control of a Hybrid Lower-limb Exoskeleton for Treadmill Stepping,” *Front. Robot. AI*, p. 98, 2021.
- [48] C. H. Chang, J. Casas, and V. H. Duenas, “A Switched Systems Approach for Closed-loop Control of a Lower-Limb Cable-Driven Exoskeleton,” *Proc. Am. Control Conf.*, vol. 2022–June, pp. 4341–4346, 2022.
- [49] J. Casas, C. Chen-Hao, and V. H. Duenas, “Switched Adaptive Integral Concurrent Learning for Powered FES-Cycling,” *IEEE Trans. Autom. Sci. Eng.*, 2023, under review.
- [50] N. Fischer, R. Kamalapurkar, and W. E. Dixon, “LaSalle-Yoshizawa corollaries for nonsmooth systems,” *IEEE Trans. Automat. Contr.*, vol. 58, no. 9, pp. 2333–2338, 2013.
- [51] J. Casas and V. H. Duenas, “Integral Torque Tracking with Anti-Windup Compensation and Adaptive Cadence Tracking for Powered FES-Cycling,” in *2023 American Control Conference (ACC), San Diego, CA, USA*, 2023.
- [52] V. H. Duenas, C. A. Cousin, V. Ghanbari, *et al.*, “Torque and cadence tracking in functional electrical stimulation induced cycling using passivity-based spatial repetitive learning control,” *Automatica*, vol. 115, p. 108 852, 2020.
- [53] C.-H. Chang, J. Casas, A. K. Sanyal, *et al.*, “Motorized FES-cycling and closed-loop nonlinear control for power tracking using a finite-time stable torque algorithm,” *Front. Control Eng.*, vol. 3, no. August, pp. 1–15, 2022.

- [54] A. Filippov, “Differential equations with discontinuous right-hand sides,” *Kluwer Acad. Publ.*, pp. 377–390, 1988.
- [55] B. E. Paden and S. S. Sastry, “A Calculus for Computing Filippov’s Differential Inclusion with Application to the Variable Structure Control of Robot Manipulators,” *IEEE Trans. Circuits Syst.*, vol. 34, no. 1, pp. 73–82, 1987.
- [56] M. Krstić, I. Kanellakopoulos, and P. Kokotović, *Nonlinear and Adaptive Control Design*, 1995.
- [57] J. Casas, C. Chen-Hao, and V. H. Duenas, “Switched Concurrent Learning Adaptive Control for Treadmill Walking using a Lower-limb Hybrid Exoskeleton,” *IEEE Trans. Control Syst. Technol.*, 2023, under review.
- [58] J. Casas, C. H. Chang, and V. H. Duenas, “Concurrent Learning Control for Treadmill Walking using a Cable-driven Exoskeleton with FES,” *Proc. Am. Control Conf.*, vol. 2022-June, pp. 3019–3024, 2022.
- [59] W. E. Dixon, A. Behal, D. M. Dawson, *et al.*, *Nonlinear Control of Engineering Systems: A Lyapunov-Based Approach*. Boston, MA: Springer, 2003.
- [60] J. J. Slotine and W. Li, “on the Adaptive Control of Robot Manipulators.,” *Am. Soc. Mech. Eng. Dyn. Syst. Control Div. DSC*, vol. 3, pp. 51–56, 1986.
- [61] D. A. Winter, *Biomechanics and Motor Control of Human Movement*. 1990, vol. 1.
- [62] M. Muhlegg, G. Chowdhary, and E. N. Johnson, “Concurrent learning adaptive control of linear systems with noisy measurements,” *AIAA Guid. Navig. Control Conf. 2012*, pp. 1–13, 2012.
- [63] R. Kamalapurkar, B. Reish, G. Chowdhary, *et al.*, “Concurrent Learning for Parameter Estimation Using Dynamic State-Derivative Estimators,” *IEEE Trans. Automat. Contr.*, vol. 62, no. 7, pp. 3594–3601, 2017.

- [64] D. E. Ochoa, “Accelerated Concurrent Learning Algorithms via Data-Driven Hybrid Dynamics and Nonsmooth ODEs,” vol. 144, no. 2012, pp. 1–13, 2021.
- [65] J. H. Le and A. R. Teel, “Concurrent learning in high-order tuners for parameter identification,” 2022. arXiv: [2204.01346](#).
- [66] R. Ortega, S. Aranovskiy, A. A. Pyrkin, *et al.*, “New Results on Parameter Estimation via Dynamic Regressor Extension and Mixing: Continuous and Discrete-Time Cases,” *IEEE Trans. Automat. Contr.*, vol. 66, no. 5, pp. 2265–2272, 2021. arXiv: [1908.05125](#).

Chapter 7

Vita

Jonathan Casas received a bachelor's degree in Industrial and Electronic Engineering in 2016, and his master's degree in Electronic Engineering in 2019 from the Colombian School of Engineering Julio Garavito. He joined the Bionics Systems Control Lab (BSC) research group at Syracuse University to pursue his doctoral degree under the supervision of Dr. Victor H. Duenas in 2019. His research interests include Adaptive nonlinear control for rehabilitation robotics, data-driven control, and switching systems.